Tunable Coherent Radiation at Soft X-ray Wavelengths:

Generation and Interferometric Applications

by

Kristine Marie Rosfjord

B.E.E. (Georgia Institute of Technology) 1999
M.S. (University of California, Berkeley) 2001

A dissertation submitted in partial satisfaction of the

requirements for the degree of

Doctor of Philosophy

in

Engineering – Electrical Engineering and Computer Sciences

in the

GRADUATE DIVISION

of the

UNIVERSITY of CALIFORNIA, BERKELEY

Committee in charge:

Professor David T. Attwood, Chair
Professor Michael A. Lieberman
Professor Costas P. Grigoropoulos

Fall 2004

Tunable Coherent Radiation at Soft X-ray Wavelengths:

Generation and Interferometric Applications

© 2004

by

Kristine Marie Rosfjord

Abstract

Tunable Coherent Radiation at Soft X-ray Wavelengths: Generation and Interferometric Applications

by

Kristine Marie Rosfjord

Doctor of Philosophy in Engineering – Electrical Engineering and Computer Sciences

University of California, Berkeley

Professor David T. Attwood, Chair

The availability of high power, spectrally and spatially coherent soft x-rays (SXR) would facilitate a wide variety of experiments as this energy region covers the primary resonances of many magnetic and biological materials. Specifically, there are the carbon and oxygen K-edges that are critical for biological imaging in the water window and the L-edges of iron, nickel, and cobalt for which imaging and scattering studies can be performed.

A new coherent soft X-ray branchline at the Advanced Light Source has begun operation (beamline 12.0.2). Using the third harmonic from an 8 cm period undulator, this branch delivers coherent soft x-rays with photon energies ranging from 200eV to 1keV. This branchline is composed of two sub-branches one at 14X demagnification and the other 8X demagnification. The former is optimized for use at 500eV and the latter at 800eV. Here the expected power from the third

harmonic of this undulator and the beamline design and characterization is presented. The characterization includes measurements on available photon flux as well as a series of double pinhole experiments to determine the coherence factor with respect to transverse distance. The first high quality Airy patterns at SXR wavelengths are created with this new beamline.

The operation of this new beamline allows for interferometry to be performed in the SXR region. Here an interferometric experiment designed to directly determine the index of refraction of a material under test is performed. Measurements are first made in the EUV region using an established beamline (beamline12.0.1) to measure silicon, ruthenium and tantalum silicon nitride. This work is then extended to the SXR region using beamline 12.0.2 to test chromium and vanadium.

Table of Contents

List of Figures ***iii***

List of Tables xi

Acknowledgements xii

1 Introduction 1

1.1 Motivation 1

1.2 EUV/SXR Sources 4

1.3 Thesis Overview 5

2 Undulator Radiation 7

2.1 Introduction 7

2.2 Overview of Synchrotron Radiation 8

2.3 First Order Undulator Solution 10

2.4 Higher Harmonics 15

2.5 Beamline Design 26

2.6 Conclusions 32

3 Beamline Characterization 33

3.1 Introduction 33

3.2 Flux in Central Radiation Cone 34

3.3 Pinhole Fabrication 37

3.4 Spatially Coherent Flux 40

3.5 Single Pinhole Characterization of Beamline 12.0.2 44

3.6 Double Pinhole Characterization of Beamline 12.0.2 50

3.7 Beamline Challenges 60

3.8 Conclusions 67

4 Interferometry - Material Testing 68

4.1 Introduction 68

4.2 Index of Refraction – definition and previous work 69

4.3 EUV Experiment 72

4.4 SXR Experiment 91

4.5 Conclusions 96

5 Conclusions 97

References 99

Appendix 110

List of Figures

1-1 The Extreme Ultraviolet (EUV) and Soft X-ray (SXR) portion of the electromagnetic spectrum [9]. 1

1-2 (a)Elbow patterns printed using 13.4nm (EUV) radiation. This lithography was performed at beamline 12.0.1.3 of the Advanced Light Source (ALS). Photo courtesy of the P. Naulleau et al. [13] (b) Protein labeled microtubule network of mouse epithelial cell taken using 520eV (SXR) radiation. This image was created using the XM-1 microscope of beamline 6.1 at the ALS. Photo courtesy of C. Larabell, UCSF and W. Meyer-Ilse, CXRO/LBNL [18]. 4

2-1 Overhead view of the advanced light source (ALS) at Lawrence Berkeley Laboratory (LBL) [29]. 8

2-2 The periodic magnets of an undulator [30] 11

2-3 First harmonic solution for the power in the central radiation cone (watts) versus electron energy (eV) for the 8cm period undulator of beamline 12 at the ALS. 14

2-4 Starting with position in the electron frame of reference, the second derivative with respect to time is taken to get acceleration in the electron frame of reference. This is inserted into the dipole radiator formula (2-8), transformed to the laboratory frame of reference, and integrated to achieve the solution of power in central radiation cone (watts) versus K for first, second and third harmonics. 18

2-5 The power in the central radiation cone versus K for the U8 undulator of beamline 12 at the ALS using the Hofmann/intuitive model (blue) and Kim model (red) for (a) the first harmonic solution and (b) the third harmonic solution. Note the agreement for low K values. For the n=3 work in this thesis, using an 8cm period undulator at the ALS (γ=3720), at 500eV K=1.8 and at 800eV K=1.1. 21

2-6 The power in the central radiation cone (W) versus electron energy (eV) of the fundamental (blue) and third (red) harmonics for the U8 undulator of beamline 12 at the ALS using the Kim model. 22

2-7 (a) Spatially coherent power (b) spatially coherent flux and (c) spectral brightness versus energy for the first (blue) and third (red) harmonics of the U8 undulator at beamline 12 of the ALS for $0.5 < K < 3.5$. 25

2-8 Reflectivity of gold at an electron energy of 500eV versus angle of incidence. 27

2-9 Reflectivity of gold, iridium, tungsten, nickel, osmium, platinum, and rhenium versus electron energy for 2 degree glancing incidence. 28

2-10 Reflectivity versus energy for the (a) 600 line/mm and (b) 1200 line/mm grating of the monochromator [49]. 30

2-11 Beamline layout of the new coherent soft x-ray beamline at the ALS. 31

3-1 Spectral responsivity of several diodes in the soft x-ray region. The diode used in this work is a GaAsP/Au Schottky diode and is denoted above with the diamond data points [52]. 34

3-2 Fabrication process for arrays of pinholes used to achieve spatial coherence and to test the level of spatial coherence of the beamline [55]. 38

3-3 SEM of single pinhole used to spatially filter the beamline radiation to create airy patterns. This pinhole has a diameter of 2.5μm. Image is courtesy of Bruce Harteneck. 39

3-4 SEM of pinhole pair used to perform spatial coherence characterization of the beamline. 5.9 μm separate the pinholes and each individual pinhole has a diameter of 450 nm. Images are courtesy of Bruce Harteneck. 40

3-5 View of beamline used to determine single pinhole size for spatial filtering. The beamline is viewed as one large optic that demagnifies the radiation by a factor of M (8 or 14 depending on the sub-branch). 41

3-6 Image of the focal spot of the 14X branchline on the YAG phosphor. The focal spot is 60μm X 9.4 μm FWHM. 43

3-7 Airy pattern and its cross-section recorded using a 2.5μm diameter pinhole at the focal plane of beamline 12.0.2 at the ALS. This picture is recorded at a wavelength of 2.48nm(500eV) with an exposure time of 200 msec. 46

3-8 Airy pattern and its cross-section recorded using a 2.5μm diameter pinhole at the focal plane of beamline 12.0.2 at the ALS. This picture is recorded at a wavelength of 2.07nm(600eV) with an exposure time of 1 sec. Note that the rings are smaller at 600eV than 500eV, as in figure 3-7, due to the shorter wavelength and thus reduced divergence angle as seen in equation (3-10). 46

3-9 Airy patterns recorded using a 500nm diameter pinhole at the focal plane of beamline 12.0.2 at the ALS for energies ranging from 500eV – 900eV. 49

3-10 Double pinhole experiment setup. An extended source illuminates two pinholes, each point of the extended source creating an interference pattern at the recording plane. The sum of the intensities of these patterns creates the overall intensity distribution. 51

3-11 Figure of beamline used to determine double pinhole dimensions. The beamline is viewed as one large optic that demagnifies the radiation by a factor of M (8 or 14 depending on the sub-branch). 52

3-12 Measured two-pinhole interference patterns and their respective lineouts for vertical pinhole separations of (a) 2μm, (b) 6μm and (c) 8μm. Each individual pinhole of the two-pinhole pairs has a diameter of 450nm to insure a spatially coherent wavefront over the individual pinhole. (d) charts the measured magnitude of the complex coherence function versus the pinhole separation. A least square error Gaussian curve is fitted to these data points. All of this data was taken at a photon energy of 500eV (2.48nm) on beamline 12.0.2 of the ALS. 54

3-13 Measured two-pinhole interference patterns and their respective lineouts for a 5μm vertical pinhole separation at a photon energy of (a) 600eV (2.07nm), (b) 700eV (1.77nm) and (c) 800eV (1.56nm). The airy envelope decreases for increasing energy, as is implied from equation (3-9). (d) charts the measured magnitude of the complex coherence function versus

the pinhole separation for 500eV(blue), 600eV(red), 700eV(green) and 800eV(black). A least square error Gaussian curve is fitted to each energy's set of data points. All of this data was taken on beamline 12.0.2 of the ALS. The coherence lengths as calculated by equation (3-19) are (a) 5.4μm, (b) 4.9μm, (c) 4.2μm and (d) 3.6μm. 55

3-14 Measured two-pinhole interference patterns and their respective lineouts for horizontal pinhole separations of (a) 1μm, (b) 4μm and (c) 8μm. (d) charts the measured magnitude of the complex coherence function versus the pinhole separation. A least square error Gaussian curve is fitted to these data points. All of this data was taken at a photon energy of 500eV (2.48nm) on beamline 12.0.2 of the ALS. 56

3-15 Interference fringes with saturated bleed through in a near-axis rectangular region. 60

3-16 Power in the central radiation cone versus energy for the 3rd, 5th and 7th harmonics [37-40] out of the U8 undulator of beamline 12. Values are plotted for 0.5 < K <3.5. Note the decreasing peak power with increased harmonic. 64

4-1 Intuitive experiment setup for material measurement. 72

4-2 Experimental setup for material testing. 73

4-3 Fabrication process for sample mask used to directly measure the index of refraction of the sample material. 75

4-4 Rough data analysis for the 287nm thick silicon sample taken at 99.6eV(12.4nm) (a) sample interferogram (b) cross-sectional lineouts of

the seven silicon interferograms taken. These lineouts run from pixel 275 to pixel 320 in the vertical direction at a horizontal pixel location of 375. The fringes are marked at each discreet pixel point. (c) close up of a sample and reference lineout. 81

4-5 Figure 4-5. Schematic of Fourier approach to data analysis to achieve the real part of the index of refraction. [2] 83

4-6 (a) δ and (b) β measurements taken about 92.5eV (13.4nm) for ruthenium. The experimental data is shown with error bars and referenced against data taken using absorption measurements [85]. The error bars on the data are a result of changing upstream alignment of the system due to the time of data acquisition. 87

4-7 (a) δ and (b) β measurements taken about 92.5eV (13.4nm) for $Ta_{57.68}Si_{26.46}N_{14.42}Ar_{1.44}$. This work was performed in conjunction with Motorola, where the sample material was deposited and Rutherford Back-Scattering measurements performed. $Ta_{57.68}Si_{26.46}N_{14.42}Ar_{1.44}$ is a highly absorptive material and as such is being considered as an absorber layer in EUV lithography phase shift masks [75, 86, 87]. This highly absorptive nature, however, creates great difficulties in taking accurate visibility measurements, and thus β, of this material. A density, ρ, of 11.914 (g/cm^3) and atomic weight, A, of 114.40 g/mole were used in these calculations. These constants were chosen based on RBS measurements performed by Motorola. 88

4-8 (a) δ and (b) β measurements taken about 92.5eV (13.4nm) and silicon's L_2 and L_3 absorption edges (99.8eV and 99.2eV, respectively). Although the sample material was originally thought to be silicon, RBS measurements determined it to be $Si_{93.96}Ar_{5.98}In_{0.06}$. The experimental data is shown with error bars and referenced against data taken using absorption measurements [85] for silicon and $Si_{93.96}Ar_{5.98}In_{0.06}$ [84]. 89

4-9 RBS results of silicon sample. From the areal density it was found that

$(Nt)_{\alpha\text{-Si}} = 6.3484 \pm 0.1962 \times 10^{17}$ atoms / cm^2, 93.96 atom %

$(Nt)_{Ar} = 4.037 \pm 0.1520 \times 10^{16}$ atoms / cm^2, 5.98 atom %

$(Nt)_{In} = 4.4 \pm 0.4 \times 10^{14}$ atoms / cm^2, 0.06 atom %

resulting in an overall density of 2.313 g /cm^3. RBS measurement courtesy of Motorola. 91

4-10 (a) δ and (b) β measurements taken about 574.1eV (2.16nm) for vanadium. The experimental data is shown with error bars and referenced against data taken using absorption measurements [85]. The sample used had a thickness of 350nm and a RBS determined density of 5.891g/cm^3. Note the increase in the magnitude of the error bars at energies higher than the absorption edge. 94

4-11 (a) δ and (b) β measurements taken about 512.1eV (2.42nm) for chromium. The experimental data is shown with error bars and referenced against data taken using absorption measurements [85]. The sample used had a thickness of 310nm and a RBS determined density of 7.115g/cm^3. Note

the increase in the magnitude of the error bars at energies higher than the
absorption edge. 95

List of Tables

2-1 Beamline summary giving spatially coherent flux delivered to the focal plane of the beamline, predicted using the third harmonic of the 8cm period undulator. 32

3-1 Transmission of the materials used in the fabrication of the pinholes. The gold, chrome, and Si_3N_4 correspond to materials in the "clear" section of the pinhole and the 2.1μm gold is the absorber section. 39

3-2 Tabulated values of the experimentally determined complex coherence length (L_c) versus energy for beamline 12.0.2, consistent with the values determined using van Cittert-Zernike when modified for the complications of beamline optics. 59

3-3 Transmission of the originally used material thicknesses in the fabrication of the pinholes for the 3rd, 5th, and 7th harmonics associated with K=1.77. K=1.77 maximized the third harmonic power at an electron energy of 500eV. Note the six order of magnitude increase in transmission from the third harmonic to the seventh. 63

3-4 Transmission of the materials used in the fabrication of the pinholes for the 3rd, 5th, and 7th harmonics associated with K=1.77. 65

4-1 Material thicknesses used for EUV index of refraction measurement. 85

Acknowledgements

First, I would like to express my appreciation towards my research advisor, Professor David Attwood. I went to the first couple of days of his class on a lark and ended up with a new research field. I benefited not only from the depth of his knowledge in the EUV/SXR field, but also from his patience in sharing this knowledge.

I would also like to thank Prof. Michael Lieberman and Prof. Costas Grigoropoulos for serving on both my qualifying exam and thesis committee. I am grateful to Prof. Ken Gustafson for all of his kind words and support in my early graduate school years and to Prof. Kam Lau for his encouragement to attend UC Berkeley. At Berkeley, students are so lucky to have Dr. Sheila Humphries who makes us feel at home and encourages us to make the EE department a welcoming place for all.

In order for there to be the creation of a new beamline, there needed to be a beamline scientist. Eric Gullikson stepped into this role and along came coherent soft x-rays. His intuition in beamline alignment was utilized time and again as well as his extensive knowledge of material properties.

None of the work presented in this thesis would have been possible without the wonderful expertise of CXRO's technical staff including Paul Denham, Brian Hoef, Drew Kemp, Seno Rekawa, Kevin Bradley, Ron Oort, Farhad Salmassi,

Phil Batson, Rene Delano, Gideon Jones, Ron Tackaberry, Bob Gunion, Hanjing Huang and Jeff Gamsby. They spent countless hours helping with beamline issues and surprises.

CXRO's nanofabrication team generously provided me with pinholes, XORs, and material samples. I would like to thank the entire nanofabrication team for this effort and in particular Bruce Harteneck for his time and amiable manner.

I would like to thank my family for all of their support during graduate school and for their ability to keep everything in perspective.

Finally, I would like to thank all of the students with whom I have been lucky enough to share my graduate school experience. I am greatly indebted to Chang Chang who was so generous with his time and knowledge. My graduate school experience has benefited tremendously from discussions with Weilun Chao, Yanwei Liu, Michael Shumway, Göran Johansson and Anne Sakdinawat. I am appreciative of the help Ryan Miyakawa and Holly Barth gave me in soft X-ray data acquisition and look forward to hearing about their continued academic successes in the years ahead.

Chapter 1

Introduction

5.1 Motivation

The availability of high power, spectrally and spatially coherent Extreme Ultraviolet (EUV) radiation has facilitated a wide variety of experiments [1-7]. Radiation with these characteristics in the Soft X-ray (SXR) region would also create many scientific and technological opportunities [8]. EUV and SXR radiation is the area of the spectrum between the ultraviolet and x-ray region of the spectrum as seen in figure 1-1. The definition of the wavelengths of this spectrum varies. For this text we will define EUV radiation as ranging from approximately 30eV to 200eV photon energy (40nm to 6nm wavelength). The SXR region will be defined as ranging from approximately 200eV to 1keV (6 nm–1nm).

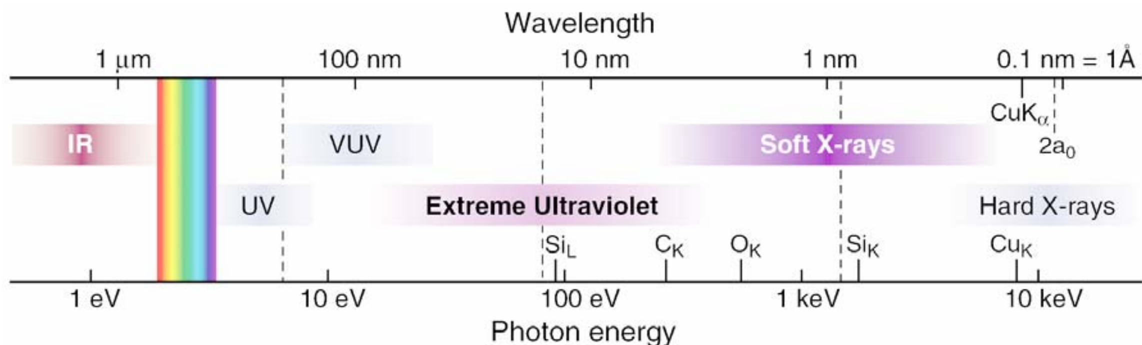

Figure 1-1 The Extreme Ultraviolet (EUV) and Soft X-ray (SXR) portion of the electromagnetic spectrum [9].

The EUV and SXR portion of the electromagnetic spectrum is important for many reasons. This energy range contains a large number of atomic resonances and

absorption edges for low and intermediate valued Z elements. For example, the L_2 absorption edge of silicon at 99.8eV and L_3 absorption edge of iron at 706.8eV fall within the EUV and SXR region. These edges create the ability to perform elemental and chemical identification [10].

The ability to print fine features is critical for the semiconductor industry [11]. The smallest linewidth, L_w, that one can write is proportional to the wavelength of the radiation used to write as seen in equation (1-1) [12]

$$L_w = k_1 \frac{\lambda}{NA} \tag{1-1}$$

where NA is the numerical aperture seen at the printing plane and k_1 is a constant that is determined from many factors including the optical system, photoresist and processing used [12].

Following equation (1-1), the short wavelengths of the EUV region, therefore, allow for smaller linewidth features to be printed. An example of elbow patterns created using 13.4nm radiation is shown in figure 1-1(a) [13]. These lines were printed at beamline 12.0.1.3 at the Advanced Light Source (ALS).

The SXR region also plays a critical role in microscopy [14]. The Rayleigh resolution, the nearest two point sources can be and still be resolved dependent on the Rayleigh criterion, can be expressed as

$$\Delta r_{rayleigh} = \frac{0.610\lambda}{NA} \tag{1-2}$$

where NA is the numerical aperture of the system. From equation (1-2), it is evident that better resolution will be achieved with decreasing wavelength.

The SXR region contains the K absorption edges of oxygen and carbon at 543.1eV and 284.2eV, respectively. These edges create the “water window” where it is desirable to image biological samples due to favorable levels of absorption [15]. Although harder x-rays (and thus shorter wavelengths) would create higher resolution images, these energies damage biological images. The XM-1 microscope [16,17] at the Advanced Light Source is a full-field transmission microscope that operates in the water window. An example of an image [18] taken with the XM-1 is shown in figure 1-1(b).

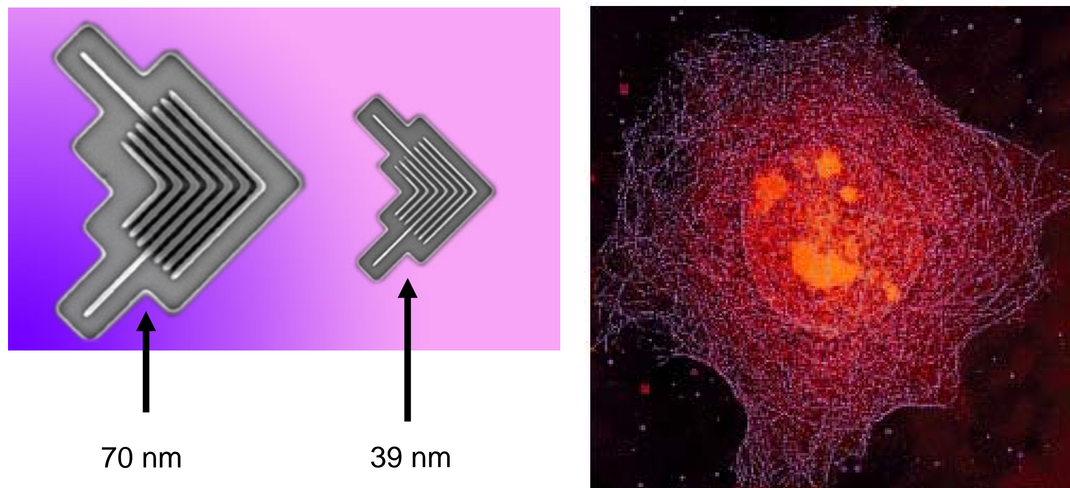

Figure 1-2 (a)Elbow patterns printed using 13.4nm (EUV) radiation. This lithography was performed at beamline 12.0.1.3 of the Advanced Light Source (ALS). Photo courtesy of P. Naulleau et al. [13] (b) Protein labeled microtubule network of mouse epithelial cell taken using 520eV (SXR) radiation. This image was created using the XM-1 microscope of beamline 6.1 at the ALS. Photo courtesy of C. Larabell, UCSF and W. Meyer-Ilse, CXRO/LBNL [18].

5.2 EUV/SXR Sources

Generation of the EUV and SXR radiation needed for the applications discussed above is not trivial. In recent years there has been significant progress in compact EUV sources, particularly plasma lasers [19] and high-order harmonic generation of intense femtosecond lasers [20, 21]. They are now capable of producing coherent radiation at EUV wavelengths with moderate photon flux levels. However, when scaling to shorter wavelengths, both sources face unfavorable demands on excitation schemes. Photon energies of several

hundred eV have not yet been reached with even moderate flux levels using these sources [22].

To create the tunable, high power, short wavelength, coherent radiation desirable for interferometric applications, this thesis will use the undulator radiation of a synchrotron source. In the EUV region, this has already successfully been achieved with beamline 12.0.1 at the ALS [23, 24]. This thesis will develop a branchline to achieve the above characteristics in the SXR region.

5.3 Thesis Overview

This thesis details the development of a new spatially and spectrally coherent soft x-ray branchline at the ALS and an interferometric application using this source. This thesis begins, in chapter 2, with the presentation of the theory behind undulator branchlines. Specifically, first order radiation out of a branchline is described. Next, high order radiation from the undulator is described. It is this higher order radiation that achieves the short wavelengths of the SXR region from the 8cm period undulator. Chapter 2 also presents the design of the new soft x-ray branchline and calculates that anticipated flux at the focal plane of the branchline.

Chapter 3 presents the characterization of this new branchline. This branchline is characterized based on the flux that reaches the focal plane as well as the flux achieved through a pinhole. Flux attained through the pinhole is referred to as

the spatially coherent flux. Airy patterns generated with this beamline are presented and the magnitude of the complex coherence factor of the beamline is determined using the classical Thompson-Wolf [25] double pinhole method.

Chapter 4 delves into interferometry performed using beamline 12. The interferometry performed directly determines the index of refraction of a material under test. These measurements are first made in the EUV region using the established beamline 12.0.1.2. At these wavelengths silicon, ruthenium, and tantalum silicon nitride are measured [26]. These measurements are then extended to the SXR region using the new beamline 12.0.2.1 where chromium and vanadium are studied.

Chapter 2

Undulator Radiation

2.1 Introduction

The availability of tunable, high power, coherent radiation at short wavelengths opens a world of experimental opportunities. Unfortunately, this is not a simple list of requirements. Lasers are routinely used for achieving these characteristics at longer wavelengths, but they do not yet provide a solution for the extreme ultraviolet and soft x-ray energy regions [22, 27]. The closest thing to a laser at this wavelength [19-21] has a longer wavelength, is spatially incoherent, has low power, is not tunable, and is capable of only a few short bursts of energy a day. The current answer to achieving these characteristics is synchrotron radiation. Synchrotron radiation is tunable, high power radiation [28]. It is not inherently spatially coherent, but rather provides a path towards achieving coherence.

This chapter discusses the generation of this tunable, high power, coherent, short wavelength radiation. Specifically, this chapter discusses synchrotron radiation as these facilities provide a path to achieving the above characteristics. The basics of synchrotron radiation and the three types of magnet structures used to produce this radiation are reviewed. Next, undulator radiation (one of these magnet structures) is discussed in depth. This chapter models what is physically going on with an undulator in the simplest case and then expands this simplest case to develop a model for the higher order harmonics. Lastly, this

chapter discusses beamline design for delivering this radiation in a focused and spectrally coherent spot at the experimental setup.

2.2 Overview of synchrotron radiation

Synchrotron radiation facilities are designed to enable electrons to travel at nearly the speed of light. When these electrons are then forced into a circular path by magnets, they emit bright ultraviolet and x-ray light

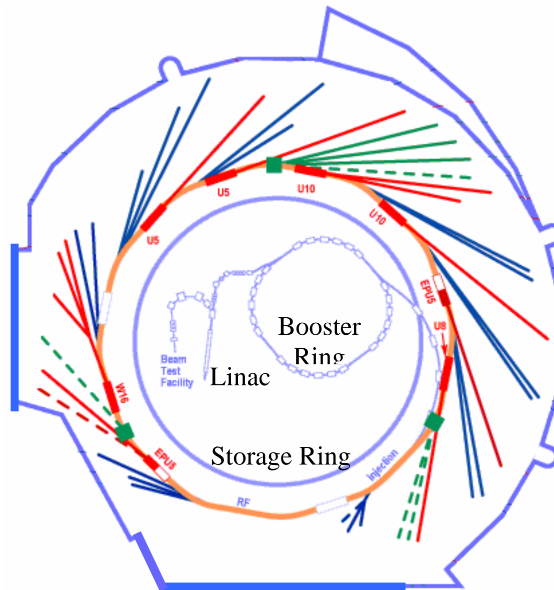

Figure 2-1 Overhead view of the advanced light source (ALS) at Lawrence Berkeley Laboratory (LBL) [29].

Figure 2-1 shows an overhead diagram of the synchrotron source discussed in this work, the Advanced Light Source (ALS). The linear accelerator (linac) and booster ring are used together to accelerate the electrons to 99.99999% the speed of light. For the ALS, this velocity gives a relativistic factor [30] of

$$\gamma = \frac{1}{\sqrt{1-\frac{v^2}{c^2}}} = 3720 \qquad (2\text{-}1)$$

where v is the electron velocity and c is the velocity of light in a vacuum. The peak current in the storage ring is 400mA, and the electron energy is equal to 1.9 GeV.

There are three general types of magnet structures that deliver the radiation out of the storage ring. These are bending magnets, wigglers and undulators. Bending magnets deliver radiation from the turns in the storage ring. They provide broad spectrum, low power radiation. Undulators and wigglers are periodic magnets placed in the straight sections of the storage ring. Undulators provide bright, laser – like radiation. Wigglers provide broad spectrum, high photon flux (yet less bright then undulators) radiation. It is the bright laser like quality that makes undulators our choice for the purposes of this thesis.

The general requirements for the radiation that are stated above include high power, tunable and coherent. Undulator radiation directly provides the first two of these requirements. Undulator radiation, however, is not inherently 100% spectrally and spatially coherent. Its high power allows for the use of filtering techniques to achieve coherence while retaining an experimentally useable level of photon flux. Radiation from an undulator is quasi monochromatic. The inherent bandwidth of the source is dependent on the geometry of the undulator as will be seen below. Increased spectral coherence is achieved with a

monochromator made up of a varied line space grating [31, 32] coupled with an exit slit.

The level of spatial coherence of a source or system can be described by the complex coherence factor, μ [33, 34]. μ has a value between 0 and 1, whereas 0 is incoherent radiation and 1 is completely coherent radiation. The radiation from an undulator can be thought of as an assembly of uncorrelated emitters. The van-Cittert Zernike theorem [35, 36] shows how one can expect some level of spatial coherence at a distant plane based on the spatial separation of two mutually incoherent quasi-monochromatic point sources, the angles and the wavelength. Spatial coherence is thus achieved with undulator radiation by filtering to limit the transverse spread and the angle of the radiation.

2.3 First Order Undulator Solution

The undulator equations have been successfully developed for all solutions (first and higher order harmonics) by Kwang-Je Kim [37-40]. These solutions are complete and accurate, yet they can appear opaque to the reader. Hofmann first presented [41, 42] and then Jackson popularized [43] an intuitive method for developing the first order solution to the undulator equation. The highlights of this approach are summarized here in order to develop a common terminology for the higher-order solution.

An undulator (figure 2-2) is a system of periodic magnets that is inserted in the straight sections of the synchrotron's storage ring. An undulator is characterized by the period (λ_u) and the number (N) of the magnet pairs. The undulator of beamline 12 (which is to be used in this thesis) has N=55 periods and λ_u = 8 cm.

The radiation pattern generated by an undulator is directed into a narrow cone. The central radiation cone is defined [30] as the angular extent of the radiation in which the spectral bandwidth

$$\frac{\Delta\lambda}{\lambda} = \frac{1}{nN} \tag{2-2}$$

where λ is the wavelength, $\Delta\lambda$ is the wavelength spread, and n is the order of the solution as will be discussed in section 2.4.

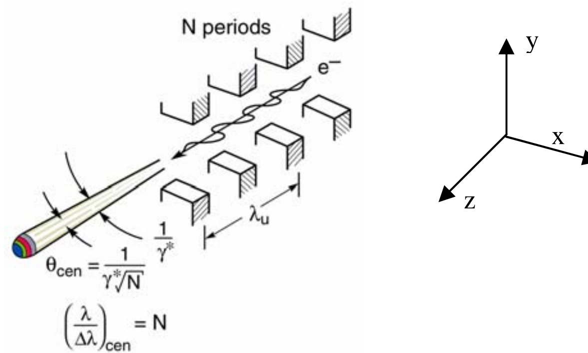

Figure 2-2 The periodic magnets of an undulator [30].

As the electron races through the magnet pairs of the undulator, the magnetic field applied by the undulator causes the electron to experience oscillations. These oscillations are what determine the output power spectrum of the undulator.

Hofmann [41] starts with the basic force (F) equation for a charge in the presence of electric (E) and magnetic (B) fields.

$$F_x = \frac{dp_x}{dt} = q(E_x + v_z \times B_y) \tag{2-3}$$

where q is the charge on an electron and dp/dt is the rate of change of momentum. The effects due to the electric field are ignored due to the large applied magnetic field. Approximating the magnetic field as a sinusoid, equation (2-3) can be solved for the velocity of the electron in the x direction (v_x) in terms of z

$$v_x = \frac{Kc}{\gamma}\sin(\frac{2\pi z}{\lambda_u}) \tag{2-4}$$

where K is the magnetic deflection parameter of $K=eB_o\lambda_u/2\pi mc$ and for now it is assumed that $v_z = c$ and K is small. Integrating equation (2-4), obtains the position x with respect to time as

$$x = \frac{-K}{\gamma k_u}\cos(\omega_u t) \tag{2-5}$$

where $k_u=\lambda_u/2\pi$ and $\omega_u=k_u c$. These calculations have all been done in the laboratory frame of reference. For calculation simplicity the calculations will now be performed in the frame of reference of the electron. Performing a Lorentz transform on equation (2-5) finds that

$$x' = \frac{-K}{\gamma k_u}\cos(\omega_u' t') \tag{2-6}$$

Taking the second derivative in order to get acceleration in the electron frame of reference gives

$$a'(t') = \frac{2\pi c^2 \gamma}{\lambda_u} \frac{K}{(1 + K^2/2)} \cos \omega_u ' t' \tag{2-7}$$

In the electron frame of reference, the only motion the electron “sees” is the undulating in the x-direction as described by equation (2-6) as the forward motion is non-existent with respect to the reference frame. Electromagnetic theory predicts that a charge oscillating back and forth can be described as a dipole radiator [44], with a radiated power distribution with respect to solid angle described as

$$\frac{dP'}{d\Omega'} = \frac{e^2 a'^2 \sin^2 \Theta'}{16\pi^2 \varepsilon_o c^3} \tag{2-8}$$

where Θ’ is the radiation angle in the electron frame of reference, e is the charge on an electron, a’ is the electron’s acceleration and ε_o is the permittivity of vacuum. Inserting the acceleration term from equation (2-7) into equation (2-8) gives the power spectral distribution with respect to solid angle as

$$\frac{dP'}{d\Omega'} = \frac{e^2 c \gamma^2}{8\varepsilon_o \lambda_u{}^2} \frac{K^2}{(1 + K^2/2)^2} \tag{2-9}$$

The portion of the solid angle that is associated with the central radiation cone can be expressed, in polar coordinates about the z-axis, as

$$\Delta\Omega_{cen} = \int_0^{2\pi} \int_0^{1/\gamma^* \sqrt{N}} \sin\theta d\theta d\phi = \frac{\pi}{\left(\gamma^* \sqrt{nN}\right)^2} \tag{2-10}$$

Transforming equation (2-9) into the laboratory frame of reference, multiplying by equation (2-10) for the central radiation cone portion of this radiation, and taking into account the many (rather than single) electrons in the undulator gives a power spectral distribution of

$$P_{cen\,x_1} = \frac{\pi e \gamma^2 I}{\varepsilon_o \lambda_u} \frac{K^2}{(1+K^2/2)^2} \tag{2-11}$$

for the first order solution of the undulator. This solution for power in the central radiation cone ($\Delta\lambda/\lambda$ = 1/N = 1.8%) versus electron energy for the 8cm period undulator of beamline 12 at the Advanced Light Source is plotted in figure (2-3). The energy values of this plot correspond to K values of $0.1 \leq K \leq 3.5$.

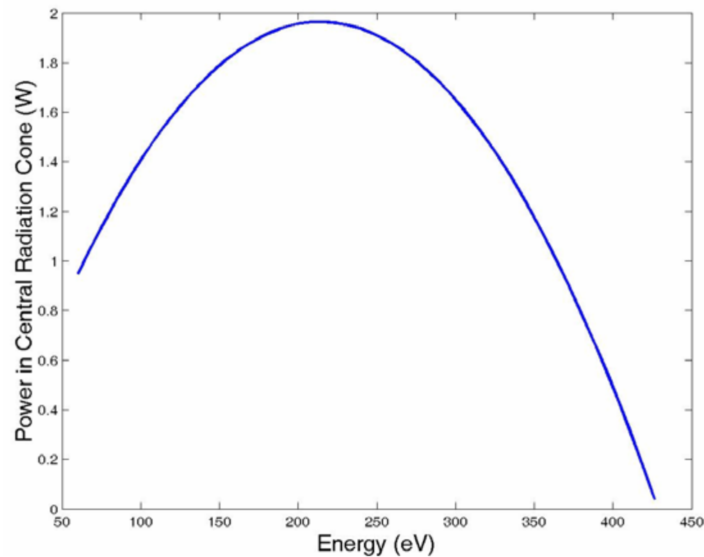

Figure 2-3 First harmonic solution for the power in the central radiation cone (watts) versus electron energy (eV) for the 8cm period undulator of beamline 12 at the ALS.

The first harmonic solution of this 8cm period undulator produces radiation up to approximately 400eV as shown in figure 2-3. The radiation is tunable by varying the gap between the magnets (and thus the magnetic field felt by the electrons, or the magnetic deflection parameter, K). This radiation is not inherently coherent, as mentioned in section 2.2, but with proper angular and spatial filtering can achieve a high complex coherence factor. This technique has been

successfully utilized at the 12.0.1 branch of beamline 12 for applications such as lithography, interferometry, and angle resolved photon emission spectroscopy.

The fact that this radiation theoretically does not reach much above the 400eV point provides a problem for applications such as optics testing, material analysis and magnetic scattering where it is desirable to have tunable, coherent radiation through 1keV (the soft x-ray region). This simple solution of the 8cm undulator does not achieve the soft x-ray region.

2.4 Higher harmonics

Higher order solutions to the above problem of an electron racing through a periodic magnetic field achieve shorter wavelengths out of the undulator. This section will inspect the assumptions from section 2.3 and develop the third harmonic solution iteratively.

An undulator is an example of an electron in motion in a uniform magnetic field. The time rate of change of the energy of an electron in a uniform magnetic field is 0 as shown in equation (2-12) [30].

$$\frac{dE_e}{dt} = v \cdot F = -ev \cdot (v \times B) \equiv 0 \qquad (2\text{-}12)$$

The above dot product is identically zero as for any vectors X,Y, $X \bullet (X \times Y) \equiv 0$. With the energy of highly relativistic electrons (as is the case with synchrotron

radiation) defined as $E_e=\gamma mc^2$, E_e defined as a constant with respect to time implies that γ is also a constant with respect to time.

In the n=1 (first harmonic) solution in section 2.3, equation (2-4) used the assumption that the velocity in the forward direction (v_z) was equal to the speed of light (a constant). This solution also found that the velocity in the transverse direction (v_x) was sinusoidal. Inspecting equation (2-13) shows how this would create a sinusoidal γ, and thus violate conservation of electron energy. Therefore, v_z must not be a constant, and must oscillate in such a way as to insure a constant relativistic factor. In other words, the electron oscillations in the transverse direction induce electron oscillation in the direction of propagation. These oscillations in the z-direction in turn induce oscillations once again in the transverse direction and so on.

$$\gamma = \frac{1}{\sqrt{1-\frac{v^2}{c^2}}} = \frac{1}{\sqrt{1-\frac{v_x^2+v_z^2}{c^2}}} \qquad (2\text{-}13)$$

Solving equation (2-13) for v_z in terms of v_x , substituting in the first order solution for v_x, equation (2-4), and simplifying gives the forward velocity of

$$v_{z_2} = c\left(1-\frac{1+K^2/2}{2\gamma^2}+\frac{K^2}{4\gamma^2}\cos 2k_u z\right) \qquad (2\text{-}14)$$

The subscript 2 on the v_z term is to denote that this is the second order solution. Note that the frequency of this solution is twice that of the first order solution.

Using the approach from section 2.2, equation (2-14) is integrated to find position, z_2, with respect to time and Lorentz tranformed to the electron lab space to get z_2'

$$z_2' = \frac{\lambda_u'}{2\pi}\frac{K^{*2}}{8}\sin 2\omega_u' t' \quad (2\text{-}15)$$

where the superscript star, *, on any variable $Q^* = Q/(1+K^2/2)^{0.5}$. Working off of this z_2' variable, the power spectral distribution in the central radiation cone with respect to K is solved for as shown in figure 2-4. It is important to note that this higher order solution (as with all even higher order solutions) will radiate off-axis. It is necessary to solve now for the third harmonic solution to achieve higher-order on-axis radiation.

To solve for the third harmonic solution of the undulator the small K approximation relating to equation (2-6) must be addressed. Without this small K approximation, equation (2-6) would read

$$x' = \frac{-K}{\gamma k_u}\cos(\omega_u' t' + \omega_u' \frac{z'}{c}) \quad (2\text{-}16)$$

where the z'/c is negligible for small K. Now instead substitute equation (2-15) into the new x' expression of (2-16) and simplify, finding that

$$x_3' = \frac{\lambda_u'}{2\pi}\frac{K^{*2}}{16}\sin 3\omega_u' t' \quad (2\text{-}17)$$

Note that the frequency of x_3' is three times that of the fundamental harmonic. Once again the power spectral distribution of the central radiation cone with

respect to K can be solved for as was done in the first harmonic case and is shown in figure 2-4.

$$x_1'(t') = \frac{-\lambda_u'}{2\pi} K^* \cos\omega_u' t'$$
$$z_2'(t') = \frac{\lambda_u'}{2\pi}\frac{K^{*2}}{8} \sin 2\omega_u' t'$$
$$x_3'(t') = \frac{-\lambda_u'}{2\pi}\frac{K^{*3}}{16} \cos 3\omega_u' t'$$

$$a_{x_1}'(t') = \frac{2\pi c^2\gamma}{\lambda_u}\frac{K}{(1+K^2/2)} \cos\omega_u' t'$$
$$a_{z_2}'(t') = -\frac{1}{2}\frac{2\pi c^2\gamma}{\lambda_u}\frac{K^2}{(1+K^2/2)^{1.5}} \sin 2\omega_u' t'$$
$$a_{x_3}'(t') = \frac{9}{16}\frac{2\pi c^2\gamma}{\lambda_u}\frac{K^3}{(1+K^2/2)^2} \cos 3\omega_u' t'$$

$$P_{cen\,x_1} = \frac{\pi e\gamma^2 I}{\varepsilon_o\lambda_u}\frac{K^2}{(1+K^2/2)^2}$$
$$P_{cen\,z_2} = \frac{1}{2}\frac{\pi e\gamma^2 I}{\varepsilon_o\lambda_u}\frac{K^4}{(1+K^2/2)^3}$$
$$P_{cen\,x_3} = \frac{27}{256}\frac{\pi e\gamma^2 I}{\varepsilon_o\lambda_u}\frac{K^6}{(1+K^2/2)^4}$$

Figure 2-4 Starting with position in the electron frame of reference, the second derivative with respect to time is taken to get acceleration in the electron frame of reference. This is inserted into the dipole radiator formula (2-8), transformed to the laboratory frame of reference, and integrated to achieve the solution of power in central radiation cone (watts) versus K for first, second and third harmonics.

One goal of this section has been to find the power with respect to energy equations of higher order solutions using an intuitive approach by extending the first harmonic solution of the Hofmann model to the third harmonic. Let us now compare these solutions with those of Kim mentioned in section 2-3. Kim's solutions can be expressed as [37-40]

$$P^{KJ}_{cenx_n} = (\hbar\omega)\pi\alpha N \frac{\Delta\omega}{\omega}\frac{I}{e}(1+\frac{K^2}{2})\frac{1}{n}\frac{K^2 n^2}{(1+\frac{K^2}{2})^2}[J_{\frac{n-1}{2}}(\frac{nK^2}{4(1+\frac{K^2}{2})}) - J_{\frac{n+1}{2}}(\frac{nK^2}{4(1+\frac{K^2}{2})})]^2$$

$$= \frac{\pi I e \gamma^2}{\varepsilon_o \lambda_u}\frac{K^2}{\left(1+\frac{K^2}{2}\right)^2}[J_0(\frac{K^2}{4(1+\frac{K^2}{2})}) - J_1(\frac{K^2}{4(1+\frac{K^2}{2})})]^2 \quad \text{(n=1)} \qquad \text{(2-18)}$$

$$= \frac{\pi I e \gamma^2}{\varepsilon_o \lambda_u}\frac{K^2 n}{\left(1+\frac{K^2}{2}\right)^2}[J_1(\frac{3K^2}{4(1+\frac{K^2}{2})}) - J_2(\frac{3K^2}{4(1+\frac{K^2}{2})})]^2 \quad \text{(n=3)}$$

where $\alpha = e^2/4\pi\varepsilon_o\nabla c$, the fine structure constant and J_0, J_1, and J_2 are Bessel functions of the 1st kind. Comparing equation (2-18) with the solutions shown in figure 2-4, they do not appear equivalent. For the first harmonic and third harmonic solutions, equation (2-18) has Bessel function terms that figure 2-4 does not. Also for the third harmonic there is a factor of four difference in magnitude.

The bessel function terms appearing in Kim's equations come from the transfer of power from lower to higher order harmonics. Performing a Taylor expansion on the Bessel function of the first harmonic and using the small K approximation it is found that

$$J_0(x) = 1 - \left(\frac{x}{2}\right)^2 \xrightarrow{smallK} 1 \qquad \text{(2-19)}$$

$$J_1(x) = \frac{x}{2} - \frac{1}{2}\left(\frac{x}{2}\right)^3 \xrightarrow{smallK} \frac{x}{2} \qquad \text{(2-20)}$$

and thus

$$\left[J_0(x) - J_1(x)\right]^2 = 1 - x \xrightarrow{smallK} 1 \tag{2-21}$$

resulting in (2-18) and (2-11) being equivalent for small K as shown in figure 2-5 (a).

The third harmonic involves a second order Bessel function which can be expanded as

$$J_2(x) = \frac{1}{2}\left(\frac{x}{2}\right)^2 - \frac{1}{6}\left(\frac{x}{2}\right)^4 \xrightarrow{smallK} \frac{x^2}{8} \tag{2-22}$$

and thus

$$\left[J_1(x) - J_2(x)\right]^2 = \xrightarrow{smallK} \frac{x^2}{4} \tag{2-23}$$

Using the x= $\frac{3K^2}{4(1+\frac{K^2}{2})}$ third harmonic term in equation (2-23) reduces equation (2-18) to

$$P_{cenx_3} = \frac{27}{64}\frac{\pi I e \gamma^2}{\varepsilon_o \lambda_u}\frac{K^6}{\left(1+\frac{K^2}{2}\right)^4} \tag{2-24}$$

The small K approximation of the third harmonic solution shown in equation (2-24) is a factor of four greater than the power in the central radiation cone found for the third harmonic using the intuitive model (figure 2-4). This factor of four can be traced to the simplification used above when determining the x_3'(t') of figure 2-4. x_3'(t') was determined by calculating the oscillations resulting from the direction of propagation oscillations that in turn were created by the first order

solution transverse oscillations. This is only half of what was happening in the actual $x_3'(t')$ term. The second order direction of propagation oscillations are relativistic. This relativistic nature causes a frequency mixing of the first and second order harmonics. For small K, this frequency mixing results in a third harmonic wave that is of the same amplitude and in phase with the $x_3'(t')$ term of figure 2-4 [45]. A factor of 2 increase in $x_3'(t')$ results in the factor of four increase in power amplitude that the power in the central radiation cone of the third harmonic was missing from the intuitive model compared to Kim's equations. Including this factor of four, there is agreement between the two models in the third harmonic solution as seen in figure 2-5 (b) for small K.

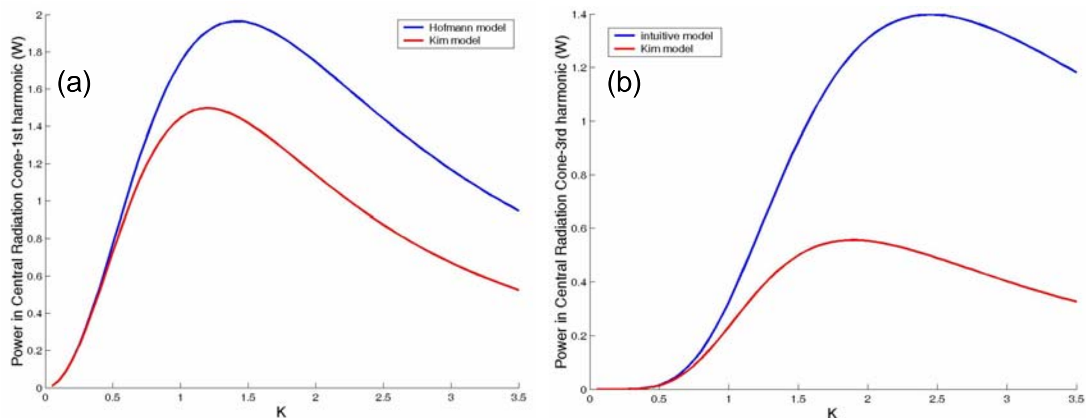

Figure 2-5 The power in the central radiation cone versus K for the U8 undulator of beamline 12 at the ALS using the Hofmann/intuitve model (blue) and Kim model (red) for (a) the first harmonic solution and (b) the third harmonic solution. Note the agreement for low K values. For the n=3 work in this thesis, using an 8cm period undulator at the ALS (γ=3720), at 500eV K=1.8 and at 800eV K=1.1.

The values of the fundamental and the third harmonic solutions to equation (2-18) are shown in figure 2-6. The K values of this figure range from 0.5 to 3.5.

This figure demonstrates the ability of the third harmonic from the 8cm period undulator, U8, of beamline 12 to extend from 200eV to 1keV as was one of the original criteria (short wavelength) for the radiation.

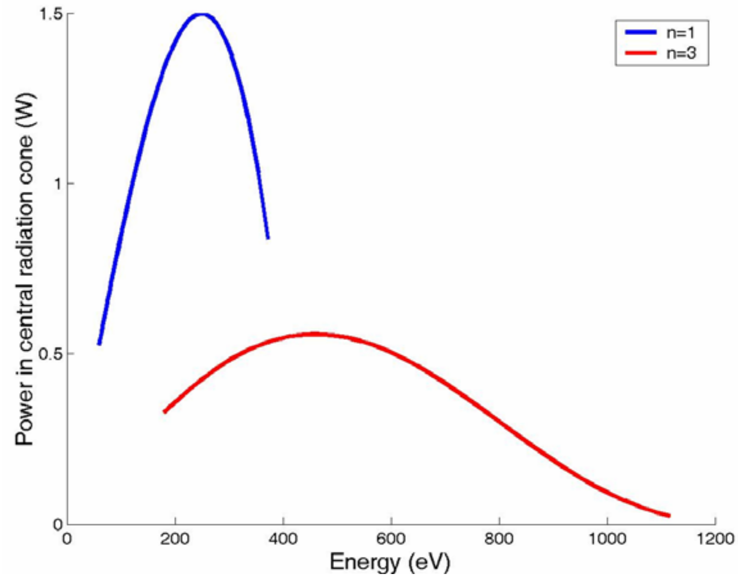

Figure 2-6 The power in the central radiation cone (W) versus electron energy (eV) of the fundamental (blue) and third (red) harmonics for the U8 undulator of beamline 12 at the ALS using the Kim model.

The radiation plotted in figure 2-6 is that in the central radiation cone. As stated in section 2-2 this radiation can be thought of as coming from uncorrelated emitters and thus is not inherently spatially coherent. Filter factors representing the space and angle filtering of the van Cittert-Zernike theorem are used to determine what portion of the central radiation cone can be considered spatially coherent. From Heisenberg's uncertainty principle, it can be determined [46] that sources with full spatial coherence can be described using the equation

$$d \cdot \theta = \frac{\lambda}{2\pi} \tag{2-25}$$

where d and θ are Gaussian rms quantities representing the source diameter and divergence half angle, respectively. Using equation (2-25) as a limiting relationship in the vertical and horizontal directions, the spatially coherent power out of the undulator can be expressed as [46]

$$P_{coh} = \left(\frac{\lambda / 2\pi}{d_x \theta_x}\right)\left(\frac{\lambda / 2\pi}{d_y \theta_y}\right) P_{cen} \tag{2-26}$$

where this is for a bandwidth equal to that of the central radiation cone (1/nN).

When planning an experiment, a quantity of interest is the number of photons per second, or flux, that the source will deliver. Flux is an important quantity for experiments that use photon-counting detectors such as CCDs. The flux of the source helps to determine experimental parameters such as exposure time. Spatially coherent flux can be determined from equation (2-26) by using the relationship that

$$F_{coh} = \frac{P_{coh}}{\hbar \omega} \tag{2-27}$$

where $\nabla\omega$ represents the electron energy.

A quantity that is commonly referred to within the synchrotron radiation community is spectral brightness. Brightness represents the flux per unit area and per unit solid angle as shown in equation (2-28). This value is often given within a 0.1% bandwidth. This is seen in equation (2-28) in the term (nN/1000). The nN term cancels out the bandwidth of the central radiation cone inherent in the F_{cen} term. As the third harmonic radiates into a smaller solid angle than the

first harmonic, it can be expected that the brightness of the third harmonic will be equal to the brightness of the first harmonic at a point where the flux of the third harmonic is lower than that of the first.

$$B = \frac{F_{cen}\left(\frac{nN}{1000}\right)}{2\pi^2 \sigma_x \sigma_y \theta_X \ \theta_Y}\left(\frac{1}{mm^2}\right)\left(\frac{1}{mrad^2}\right)\left(\frac{1}{0.1\% BW}\right) \tag{2-28}$$

where σ_x and σ_y are the semi-major and semi-minor axes of the elliptical beam cross section and θ_x and θ_y are the total central cone half angles to be discussed further in chapter 3 [30].

Equations (2-26), (2-27), and (2-28) are plotted in figure 2-7 for the U8 undulator of beamline 12 at the ALS for 0.5 < K < 3.5. This figure demonstrates that soft x-ray, spatially coherent power is achievable from the 8cm period undulator available, as was the goal of this section.

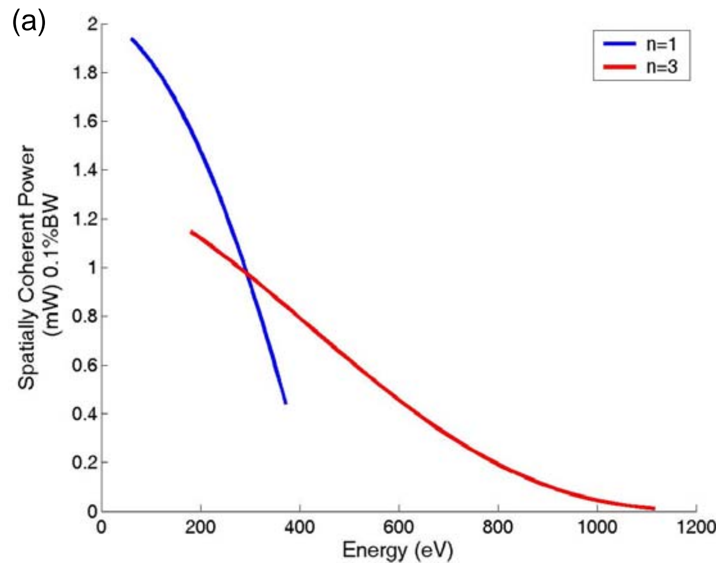

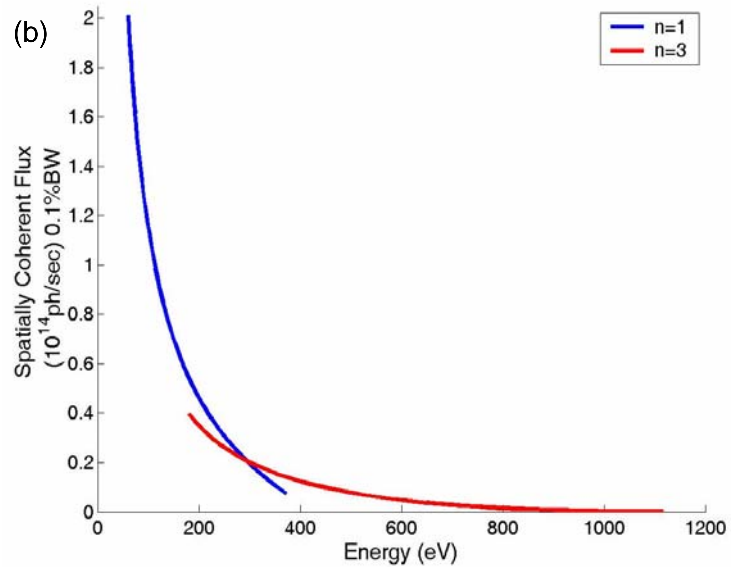

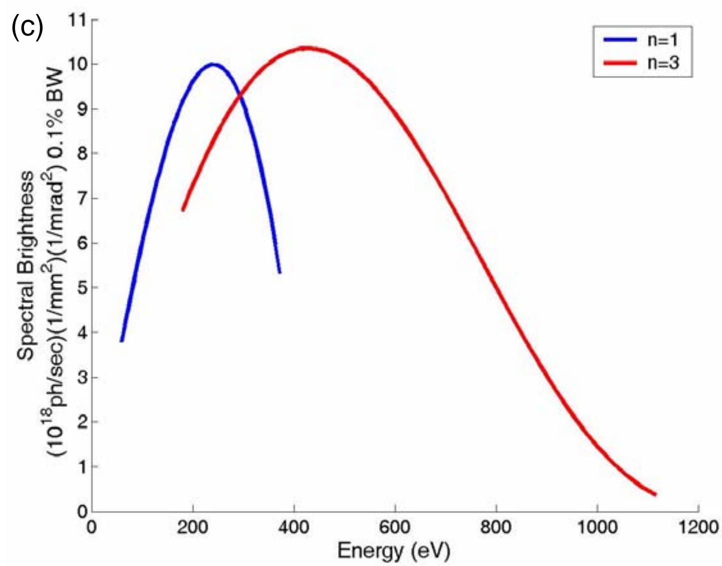

Figure (2-7) (a) Spatially coherent power (b) spatially coherent flux and (c) spectral brightness versus energy for the first (blue) and third (red) harmonics of the U8 undulator at beamline 12 of the ALS for $0.5 < K < 3.5$.

2.5 Beamline Design

Beamlines are used to deliver the radiation from the undulator to the user's experiment. These beamlines are comprised of elements used to increase the spectral coherence of the beam, focus the beam to a smaller spot size, and to rid the beam of some of the excess power at other angles and energies. The beamline also serves as a differential pump between the ultra low pressures of the storage ring (~pTorr) to the pressures of a common end station (μTorr).

The beamline performs the functions listed above with the goal of minimizing power loss. Because of this goal, careful consideration in the beamline design process is given to the number of mirrors in the beamline, the angle at which these mirrors are incident to the beam, and what types of coatings are used for the reflective surface of each beamline optic.

$$R_p = \left|\frac{E_o^{''}}{E_0}\right| = \frac{\left|n^2 \cos\phi - \sqrt{n^2 - \sin^2\phi}\right|^2}{\left|n^2 \cos\phi + \sqrt{n^2 - \sin^2\phi}\right|^2} \tag{2-29}$$

As seen in equation (2-29) [47] the reflectivity of the material is dependent on the angle of incidence upon that material. In (2-29) ϕ is defined as the complement of the angle of incidence with the reflecting surface and n, the index of refraction, of the material is defined as

$$n=1-\delta+\iota\beta \tag{2-30}$$

where δ is the phase shifting part and β is the absorptive part of the refractive index, to be described in detail in chapter 4. The subscript p on the reflectivity equation denotes that the radiation from the undulator is parallel to the plane of incidence.

In the EUV and SXR regions, the refractive index of most materials is very close to 1. Closer inspection of equation (2-29) shows that for large values of ϕ, or small angles of incidence, the reflectivity increases. Thus, small angle or glancing incidence angle reflection yield higher reflectivity at these wavelengths. This is shown in figure 2-8 where the reflectivity of gold at 500 eV is plotted versus an incident angle ranging from 0° (total external reflection) to 4.5°. A glancing incidence angle of 2° was chosen for the mirrors and grating in the beamline as it is a tradeoff between reflectivity and ease of steering and focusing.

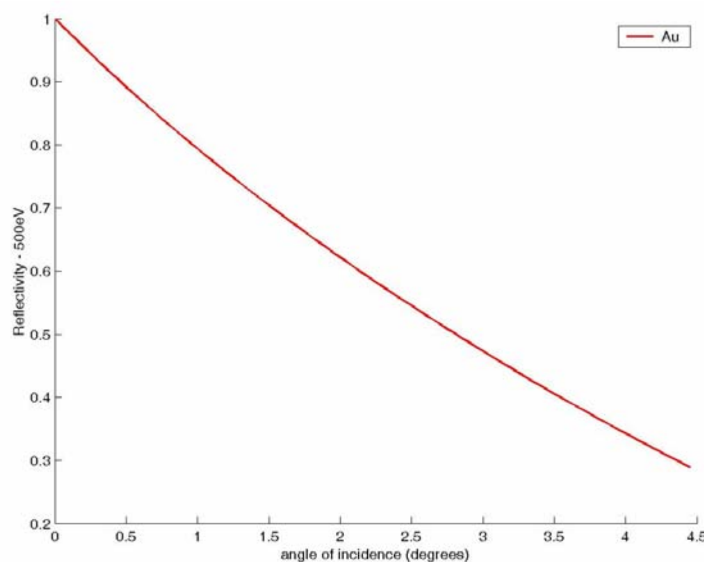

Figure 2-8 Reflectivity of gold at an electron energy of 500eV versus angle of incidence.

Materials considered as coatings for the beamline mirrors included gold, iridium, tungsten, nickel, osmium, platinum, and rhenium. All of the aforementioned have similar reflectivity characteristics in the 200 eV-1 keV energy region other than nickel. Nickel was considered a strong candidate for a coating material as it has a reflectivity greater than 80% in the 500eV range. Unfortunately, its L_3 absorption edge at 852.7 eV causes its reflectivity to greatly decrease about this energy value. The reflectivities of these materials are shown for 2° glancing incidence in figure 2-8 based on the reflectivity equation (2-29). For the new beamline, a combination of one gold, one iridium, and two tungsten mirrors were selected to balance reflectivity, material deposition ease and material price. Using equation (2-29), these materials have a theoretical reflectivity of 0.622, 0.664, and 0.677 at 500eV, respectively.

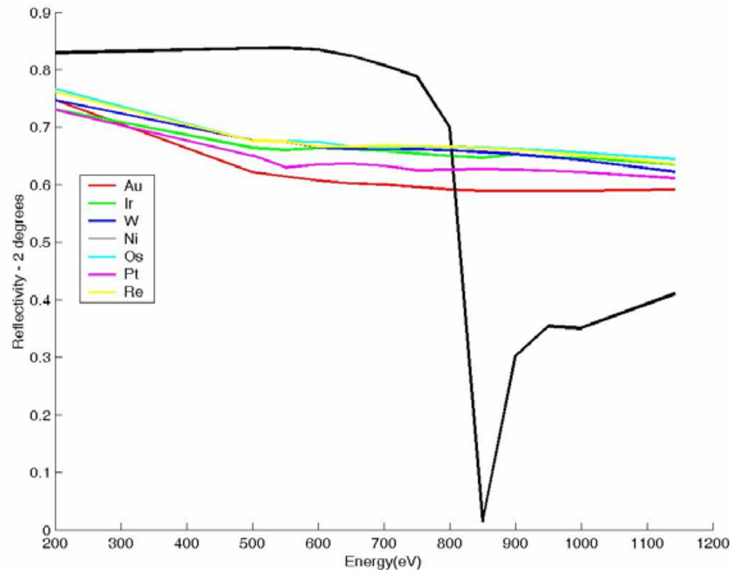

Figure 2-9 Reflectivity of gold, iridium, tungsten, nickel, osmium, platinum, and rhenium versus electron energy for 2 degree glancing incidence.

The new coherent soft x-ray branchline, 12.0.2, at the ALS is actually composed of two sub branches. The coherent optics branch has a 14X demagnification and is optimized for 500eV (2.48nm). The coherent scattering branch has a demagnification of 8X and is optimized for 700eV. Two sub-branches were decided upon due to the end-stations of the experiments. With two sub-branches, each of the two user groups is able to have a permanent endstation in place.

The layout of this new coherent soft x-ray beamline is shown in figure 2-11 [48]. First along the beam path are the water-cooled beam-defining apertures. The total power out of the undulator (all harmonics and in all directions) is [37]

$$P_{TOT}(@\,500eV) = \frac{\pi N e I \gamma^2 K^2}{3\varepsilon_o \lambda_u} = 226W \tag{2-31}$$

for the K= 1.77 value which maximizes the 500eV radiation from the third harmonic. The water-cooled beam defining apertures absorb much of this radiation so that fewer elements further downstream do not also need to be cooled. Minimizing the amount of water-cooling required is valuable to minimize cost and to reduce the number of sources of vibration in the beamline.

The branchline optics consist of four mirrors and a monochromator. The first optical element is a water-cooled, 2° horizontally deflecting, planar mirror coated in gold, which deflects the beam into beamline 12.0.2. Next is an angular aperture. This aperture selects the central radiation cone of the beam, optimized for the 33.57μrad central radiation cone of the third harmonic at 500eV. As seen

in figure 2-6, the harmonic with the highest power for a given K value is the first harmonic. This harmonic also has the largest central radiation cone as seen in equation (2-2). Thus, an angular aperture serves to partially stop the over-powering first harmonic. The next optical element is a water-cooled, spherical, vertically deflecting mirror coated in iridium that focuses the source onto the exit slit of the monochromator.

Next along the beam path is the monochromator composed of a water-cooled, varied line-space grating coated in gold and a vertical exit slit. The design of the monochromator allows for one of two gratings (600 lines/mm or 1200 lines/mm) to be chosen based upon what part of the 200eV-1keV energy region is desired. The reflectivity versus electron energy of these gratings is shown in figure 2-10 [49]. This monochromator allows for a bandwidth as low as 0.1% (compared to the 0.6% bandwidth of the third harmonic central radiation cone.)

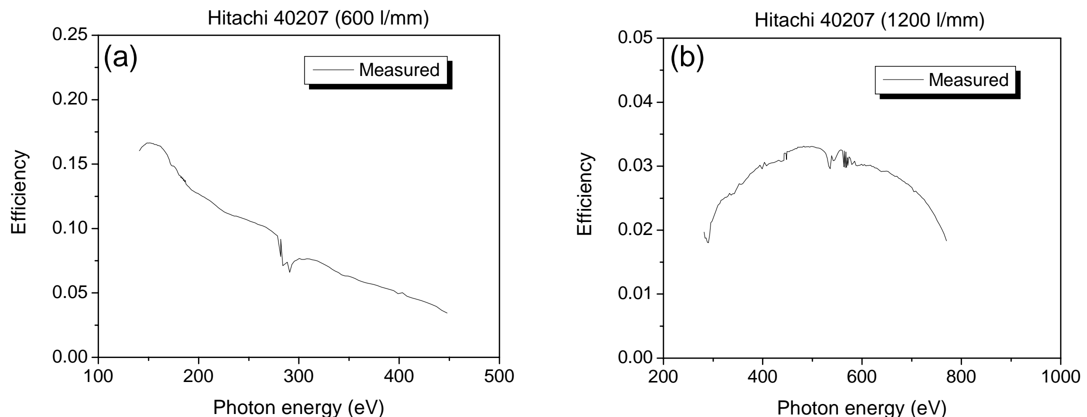

Figure 2-10 Reflectivity versus energy for the (a) 600 line/mm and (b) 1200 line/mm grating of the monochromator. [49]

Lastly, are two pairs of tungsten coated mirrors comprising the Kirkpatrick-Baez (K-B) [50] focusing system for the two sub-branches.   The horizontally deflecting K-B mirror images the source onto the pinhole plane as it is the only horizontally focusing element in the beamline, whereas the vertically deflecting K-B mirror images the exit slit of the monochromator onto the pinhole plane.

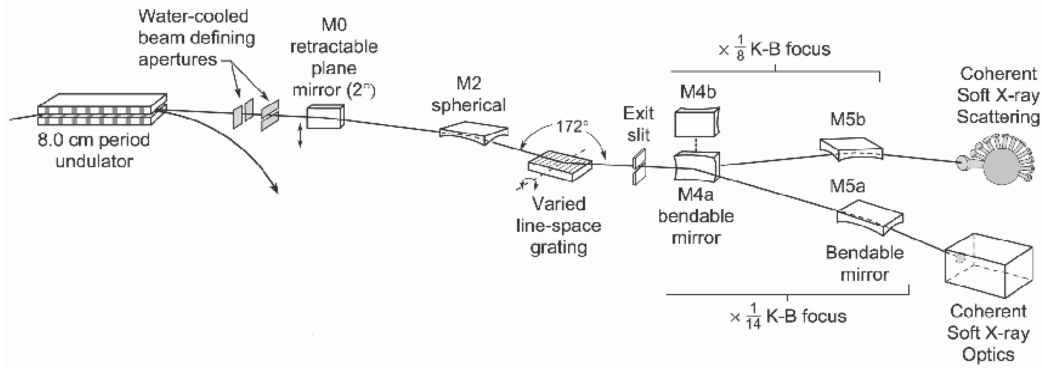

Figure 2-11 Beamline layout of the new coherent soft x-ray beamline at the ALS.

Using the reflectivity of the one gold, one iridium, and two tungsten mirrors found in figure 2-9, and the grating reflectivity shown in figure 2-10 the efficiency of the beamline and the flux delivered to the experimental endstations can be determined. This is summarized in table 2-1. Table 2-1 lists the beamline efficiency, the spatially coherent flux in the central radiation cone and the part of this spatially coherent flux delivered to the beamline focal plane for the energy region of 500eV – 800eV.

Energy (eV)	λ (nm)	K	θ_{cen}(urad) n=3, σ^1=0 finite K	Eff. for 2 W, 1 Au, 1 Ir mirrors and hitachi grating-η	Spatially Coherent Flux-F_{sp} BW=1/nN, finite σ'	F_{sp} with η BW=0.1%
500	2.48	1.77	33.57	0.00567	4.69E+13	4.39E+10
550	2.25	1.64	32.01	0.00553	3.69E+13	3.37E+10
600	2.07	1.51	30.65	0.00534	2.88E+13	2.54E+10
650	1.91	1.4	29.45	0.00437	2.22E+13	1.60E+10
700	1.77	1.29	28.37	0.00433	1.68E+13	1.20E+10
750	1.65	1.2	27.41	0.00426	1.25E+13	8.80E+09
800	1.55	1.1	26.54	0.00251	9.11E+12	3.80E+09

Table 2-1 Beamline summary giving spatially coherent flux delivered to the focal plane of the beamline, predicted using the third harmonic of the 8cm period undulator.

2.6 Conclusions

This chapter established the theoretical existence of tunable, spatially and spectrally coherent soft x-ray radiation. This was done by extending the first harmonic solution of the Hofmann model to the shorter wavelengths of the third harmonic. The design of a beamline used to deliver this short wavelength radiation was presented. Using the beamline design parameters chosen and the flux equations developed in section 2.4, the expected flux delivered to the focal plane of the beamline was established.

Chapter 3

Beamline Characterization

3.1 Introduction

The flux and coherence properties of a beamline are critical pieces of information for experimental design. An undesirably low flux level will cause experimentally difficult exposure times. Low spatial coherence for a given spatial and angular filtering will cause low fringe visibility. Chapter 2 presented the radiation theoretically expected at the focal plane of beamline 12.0.2, the new coherent soft x-ray branchline at the ALS, which was commissioned in March of 2003. This chapter will verify the flux and coherence calculations experimentally to determine the actual beamline parameters.

This chapter presents the results of the characterization of this soft x-ray branchline. This characterization will first measure the flux found in the central radiation cone at the focal plane of the branchline and then measure the spatially coherent flux found through an appropriately sized pinhole. Airy patterns taken from diffraction through a pinhole are presented and a double pinhole characterization is performed to determine the magnitude of the complex coherence factor in the vertical and horizontal directions with respect to distance. Lastly, challenges associated with the beamline characterization are presented.

3.2 Flux in Central Radiation Cone

The flux in the central radiation cone was measured by detecting the current on a photodiode placed directly behind the focal plane of the 14X branchline. The flux could then be calculated with the knowledge of the photodiode's responsivity for a specific wavelength.

The photodiode used was a GaAsP/Au Schottky photodiode from Hamamatsu, product number G2119 [51]. The quartz window placed in front of the diode by the manufacturer was cut out, since this window is strongly absorptive at the soft x-ray energy range. The G2119 has a detecting area of 10mm X 10mm. The responsivity versus photon energy plot for the detector is shown in figure 3-1 [52]. At 500eV, this detector has a responsivity of 1W/0.164A.

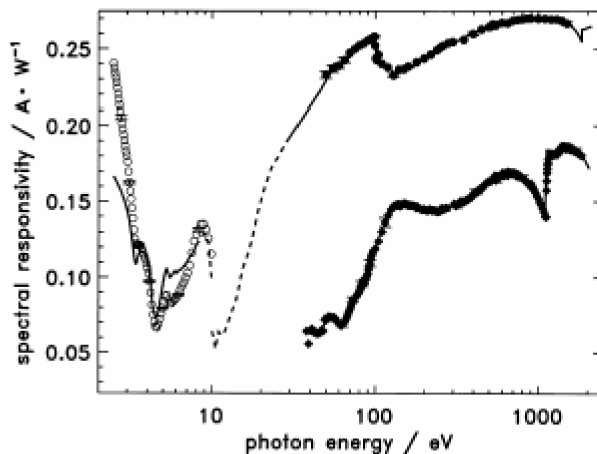

Figure 3-1 Spectral responsivity of several diodes in the soft x-ray region. The diode used in this work is a GaAsP/Au Schottky diode and is denoted above with the diamond data points [52].

The bandwidth associated with the central radiation cone is selected using the exit slits of the beamline monochromator. The change in output wavelength per

change in distance across the exit slit is referred to as the linear wavelength dispersion. This quantity varies based upon the incoming angle of the radiation onto the grating. This implies that the linear wavelength dispersion is dependent upon the wavelength chosen.

Tables showing the grating parameters for the 600 lines/mm and 1200 lines/mm gratings of beamline 12.0.2 are shown in Appendix A [53]. These tables include the radiation incoming angle, the wavelength, the energy and the corresponding linear wavelength dispersion. Interpolating from these tables, at an energy of 500 eV, the monochromator exit slit width for the 0.61% natural bandwidth of the central radiation cone can be determined as

$$slit_width(\mu m) = \frac{1}{nN}\lambda(nm)\frac{1}{Disp}\frac{\mu m}{nm} = 30.8\mu m \,@\, 500eV \qquad (3\text{-}1)$$

Using this exit slit width of 31μm at 500eV, a current of 0.225 mA was measured on the diode placed directly behind the focal plane of the 14X branchline when the ALS current was equal to 353mA. This diode current corresponds to a flux in the central radiation cone of

$$flux_{BW=1/nN} = 0.225mA \times \frac{1W}{0.164A} = 1.37mW(@\,500eV) \qquad (3\text{-}2)$$

$$= 1.71 \times 10^{13}\,\frac{photons}{\sec}$$

The theoretical value expected for the flux in the central radiation cone arriving at the focal plane on beamline 12.0.2 can be determined using equation (2-18) and

table 2-1. Inserting the undulator parameters and the experimental ALS current into equation (2-18) yields a flux of 6.08×10^{15} photons/second in the central radiation cone coming out of the U8 undulator. Multiplying this number by the beamline efficiency of 0.00567 stated in table 2-1 for 500eV yields a photon flux of 3.45×10^{13} photons/second in the central radiation cone at the focal plane of the beamline.

The flux found experimentally is a factor of 2.02 smaller than that found theoretically. Correct alignment of all optical elements in the beamline is critical in order to achieve the experimental flux value found. Beamline challenges with associated with achieving this correct alignment will be discussed in section 3.7.

Several factors can contribute to the 2.02 times difference in the predicted and experimental flux. The spectrum in the central radiation cone can be broadened by both the limited number of undulator periods and the fact that the electron beam has non-negligible divergence angles [30]. For our experiment, the electron beam has a divergence angle of 23 μrad in horizontal direction, which is comparable to the central radiation cone (33.6 μrad). With monochromator still set to an ideal bandwidth of 1/165 which assumes zero divergence, a broader bandwidth in the central radiation cone will result in lower photon flux passing through the monochromator. Other possible reasons include incorrect alignment of all optical elements in the beamline, and performance degradation of the optics due to less than ideal coatings and carbon contamination that is known to

accumulate over time.

3.3 Pinhole Fabrication

The above section discussed the flux experimentally found in the central radiation cone at the focal plane of the beamline. As previously discussed in chapter 2, this radiation is not inherently spatially coherent; spatial and angular filtering must be used to achieve spatial coherence. This filtering is done using pinholes with a diameter in the range of a few microns as is to be discussed in section 3.4. Pinholes with diameters as small as needed for spatial coherence at beamline 12.0.2, and specifically double pinhole pairs that are needed for the experiments of section 3.6 are not commercially available [54]. Therefore, pinholes used to achieve spatial coherence and to test the beamline's level of spatial coherence were fabricated at Lawrence Berkeley Lab by the Center for X-ray Optic's nanofabrication team [55].

The fabrication process for creating the pinholes used is shown in figure 3-2. The process starts with a silicon wafer with a 0.1μm silicon nitride window stretched

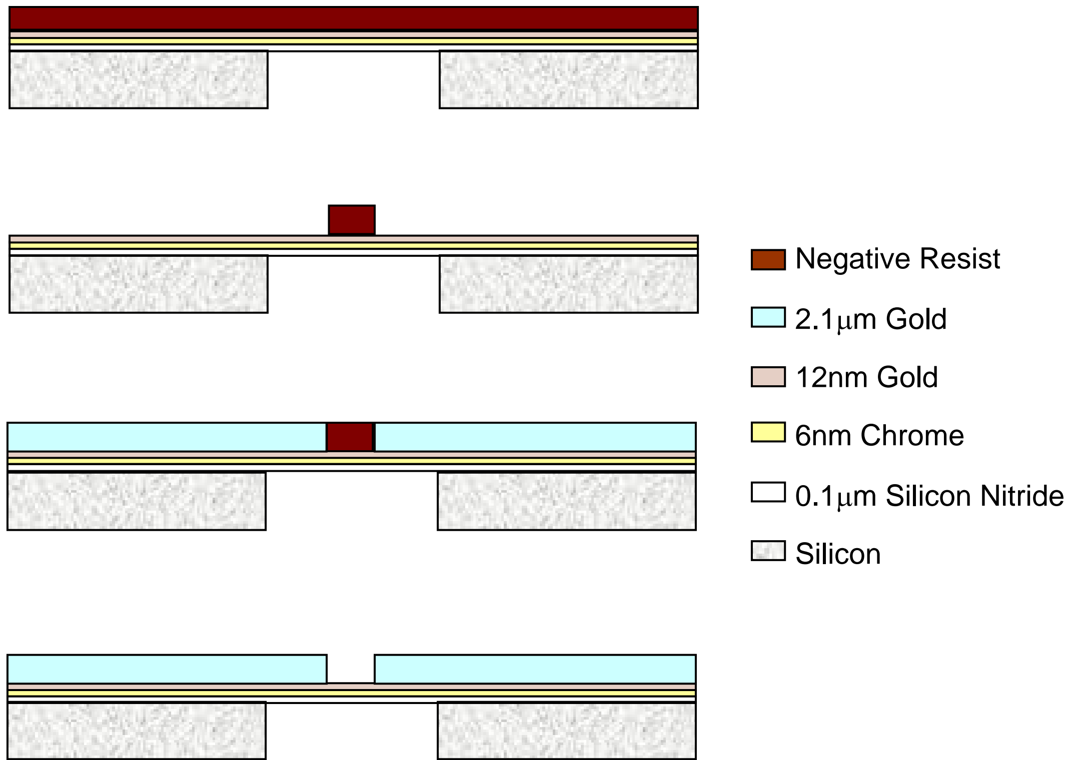

across a 500μm X 500μm square back opening. 6nm of chrome and 12 nm of gold are deposited on the silicon nitride to act as a plating base. Negative resist is spun on the plating base and then patterned with the e-beam nanowriter so that only the "posts" where the pinholes will be located remain. Next, 2.1μm of gold is electo-plated as an absorber material for the pinhole. The resist is then removed revealing the pinhole.

Figure 3-2 Fabrication process for arrays of pinholes used to achieve spatial coherence and to test the level of spatial coherence of the beamline [55].

Note in figure 3-2 that the finished pinholes are not empty. The “clear” portion of the pinhole contains 0.1μm silicon nitride, 6nm of chrome and 12nm of gold. As shown in table 3-1, at 500eV these materials correspond to a transmission of 46% for the “clear” portion of the pinhole. This compares to the absorptive (gold) part of the pinhole which transmits 9.71E-21%.

	Transmission for:			
Energy	2.1μm Gold	12nm Gold	6nm Chrome	0.1 μm Si_3N_4
500eV	9.71E-23	0.749	0.984	0.623
800eV	2.50E-14	0.836	0.946	0.866

Table 3-1 Transmission of the materials used in the fabrication of the pinholes. The gold, chrome, and Si_3N_4 correspond to materials in the “clear” section of the pinhole and the 2.1μm gold is the absorber section.

SEM pictures of the fabricated pinholes are shown in figures 3-3 and 3-4. Figure 3-3 is of a 2.5 μm single pinhole. Figure 3-4 shows a pinhole pair. The pair is separated by 5.9μm. A close up of one of the individual 450nm diameter pinholes of this pair is also shown. The choice of diameter and spacing of these pinholes will be discussed in sections 3.4 and 3.6.

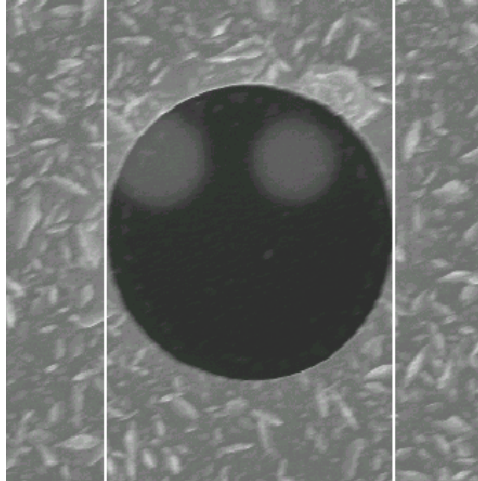

Figure 3-3 SEM of single pinhole used to spatially filter the beamline radiation to create airy patterns. This pinhole has a diameter of 2.5μm. Image is courtesy of Bruce Harteneck.

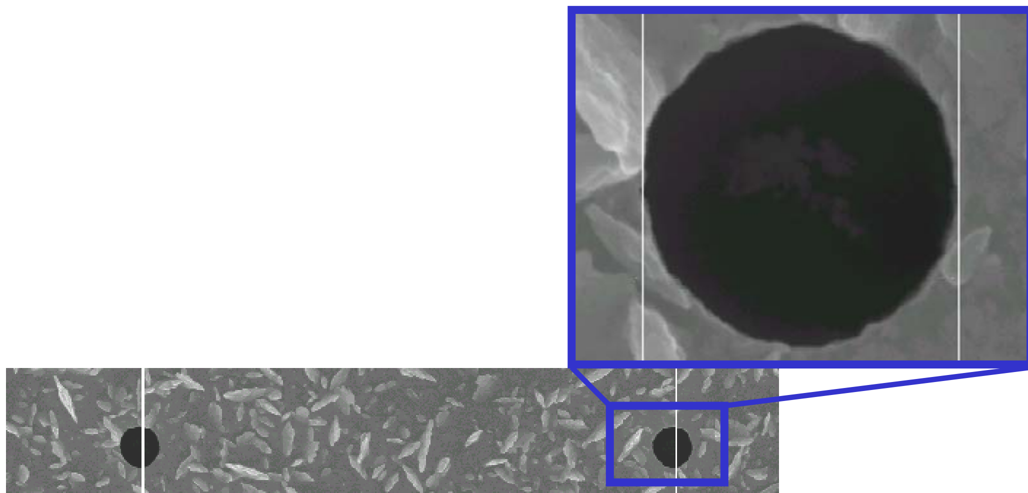

Figure 3-4 SEM of pinhole pair used to perform spatial coherence characterization of the beamline. 5.9 μm separate the pinholes and each individual pinhole has a diameter of 450 nm. Images are courtesy of Bruce Harteneck.

3.4 Spatially Coherent Flux

The spatially coherent flux of the 14X branchline of beamline 12.0.2 was experimentally determined by detecting the flux after an appropriately sized pinhole. The pinhole diameter was chosen such as to create a resultant angle twice that of the incoming angle to create a clearly defined Airy pattern. Airy patterns are discussed further in section 3.5.

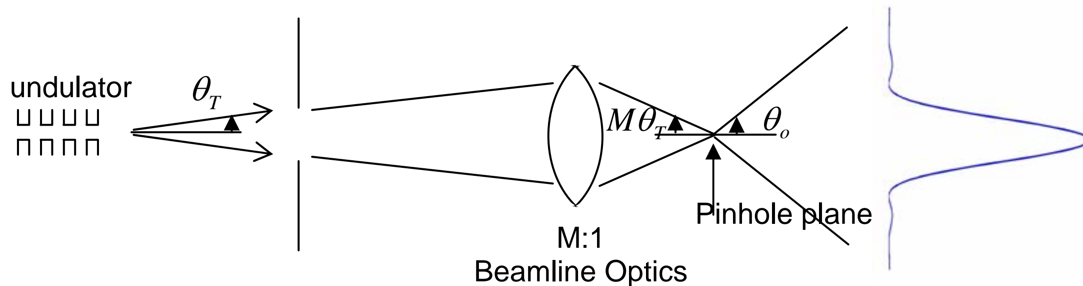

Figure 3-5 View of beamline used to determine single pinhole size for spatial filtering. The beamline is viewed as one large optic that demagnifies the radiation by a factor of M (8 or 14 depending on the sub-branch).

To determine the incoming angle of the radiation to the pinhole, the beamline is represented in the diagram by one large optic demagnifying the radiation spot

either 14X or 8X depending on the sub branch used. The half angle of the radiation from the undulator, θ_T, can be defined as [30]

$$\theta_T = \sqrt{\theta_{cen}^2 + \left(\sigma'\right)^2} \tag{3-3}$$

where σ' is the rms angular divergence of the beam in the storage ring. For the ALS, $\sigma'_x = 23\mu rad$ and $\sigma'_y = 3.9\mu rad$, and thus $\theta_{T_x} = 40.7\mu rad$ and $\theta_{T_y} = 33.8\mu rad$ at 500eV. The larger of these values is chosen so that a greater filtering is required. The 14X demagnification of the coherent optics branchline results in an incident angle at the pinhole plane 14 times greater then that shown above, or

$$\theta_{incident} = 14\theta_T = 570\mu rad \text{ at 500eV} \tag{3-4}$$

The angle to be created from the filtering pinhole is chosen to be twice the value of the incident angle in order to force the production of a well-defined Airy pattern. This resultant angle can be expressed as

$$\theta_o = 2\theta_{incident} = 1.14 mrad \text{ at 500eV} \tag{3-5}$$

The diameter of the spatially filtering pinhole, d, is then chosen based on θ_o according to the equation for diffraction through a pinhole [55]

$$\theta_o = 1.22\frac{\lambda}{d} \tag{3-6}$$

At 500eV and the incident angle shown in equation (3-5) for the 14X branchline, this corresponds to a pinhole with a diameter of 2.65μm. This pinhole is shown in figure 3-3 and was measured using an SEM to have a diameter of 2.5μm.

To measure the spatially coherent flux at 500eV, the 2.5μm pinhole was placed at the focal plane of the 14X sub branch. Using the photodiode described in section 3-2, 0.232μA was detected behind the pinhole. This current corresponds to spatially coherent flux of

$$flux_{coh} = 0.232\mu A \times \frac{1W}{0.164A} = 1.41\mu W\,(@\,500eV) \qquad (3\text{-}7)$$

$$= 1.77 \times 10^{10}\,\frac{photons}{\sec}$$

This measurement has the central radiation cone bandwidth of 0.61% seen in equation (2-2).

As in section 3-2, equation (2-18) and table 2-1 are used to determine a theoretical flux of 2.63 x 10^{13} photons/sec in the central radiation at the focal plane of the beamline for an ALS current of 268mA in equation (3-7). This is the flux incident onto the pinhole.

The amount of this central radiation cone flux focused into the 2.5μm pinhole is determined by examining the focused spot of the beamline. A picture of the focal spot of the beamline is shown in figure 3-6. This image was recorded by inserting a W/C multilayer mirror into the beamline before the focal plane. This mirror is positioned at a 45° incident angle in order to turn the beam 90°. A camera is focused on a YAG phosphor placed at a distance equal to that from the mirror to the focal plane. The YAG fluoresces in the visible region when soft x-ray radiation is incident upon it. The W/C multilayer mirror's peak reflectivity is

~8% at a wavelength of 4.9nm (253eV) [57]. As such, focusing is performed at 4.9nm.

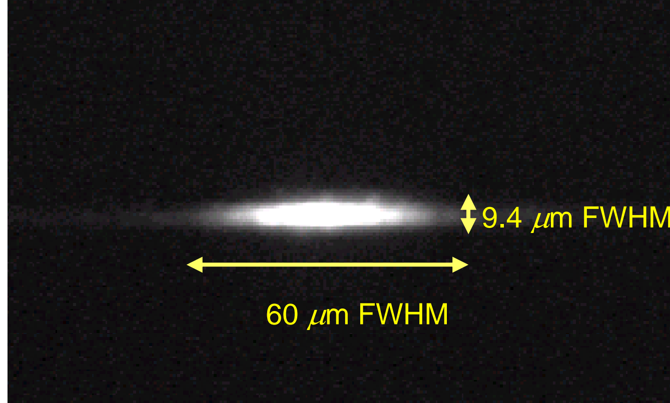

Figure 3-6 Image of the focal spot of the 14X branchline on the YAG phosphor. The focal spot is 60μm X 9.4 μm FWHM.

Calculating the intensity transmission of a 2.5 μm diameter circle in the highest intensity part of this focused beam and the intensity of the entire focused beam, a intensity ratio of 0.61% was found. Assuming the pinhole had been positioned in the beam path such as to optimize the flux through it, this ratio represents the part of the central radiation cone that passes through the pinhole.

Taking into consideration the transmission of the silicon nitride, chrome and gold in the pinhole as discussed in section 3-2, the theoretically determined coherent flux can be expressed as

$$flux_{coh,theotetical} = 2.63\times10^{13}\times0.61\%\times45.9\% \quad (3\text{-}8)$$

$$= 7.36\times10^{10}\,\frac{photons}{\sec}$$

This is a factor of 4.16 greater than the experimental value of equation (3-7). A factor of 2.02 of this error can be attributed to the flux found in the central radiation cone as was found in section 3.2. This error is also a result of the intensity ratio process used to determine the theoretical value of spatially coherent flux.

3.5 Single Pinhole Characterization of Beamline 12.0.2

A wave normally incident on a circular aperture will produce a radial intensity distribution in the far field according to equation (3-9) if it has a sufficient level of spatial coherence [56] where w is the aperture radius and z is the distance from the aperture to the pattern. This pattern is referred to as an Airy pattern. As a first order measurement of the spatial coherence of the beamline, we will look at the far field patterns generated by the 2.5 μm diameter single pinhole discussed in section 3.4.

$$I(r) = \left(\frac{\pi w}{\lambda z}\right)^2 \left[2\frac{J_1(kwr/z)}{kwr/z}\right]^2 \tag{3-9}$$

The far field patterns are recorded on a CCD camera. This CCD chip is back thinned (~15μm thick), ie. the light enters the back of the grinded down chip to eliminate the absorption in the top layer and so that the photons will only have a short distance to travel. These characteristics are critical for the camera to be operational in the short wavelength region of interest [58]. For energy regions greater than 10eV, the CCD will generate multiple electron-hole pairs for each

incident photon. The specific CCD used is a TEK1024X1024b made by Princeton Instruments in conjunction with Princeton controller ST138. The detector area is 1” by 1”, 1024 pixels X 1024 pixels (24.8μm/pixel).

Placing the 2.5μm diameter pinhole at the focal plane of the 14X branch, Airy patterns were generated at 500 eV (200msec exposure time) and 600 eV (1 sec exposure time) as shown in figures 3-7 and 3-8. These images were recorded with the CCD camera placed 1.44m downstream from the pinhole plane. 1.44m downstream of the pinhole plane corresponds with the edge of the optical table.

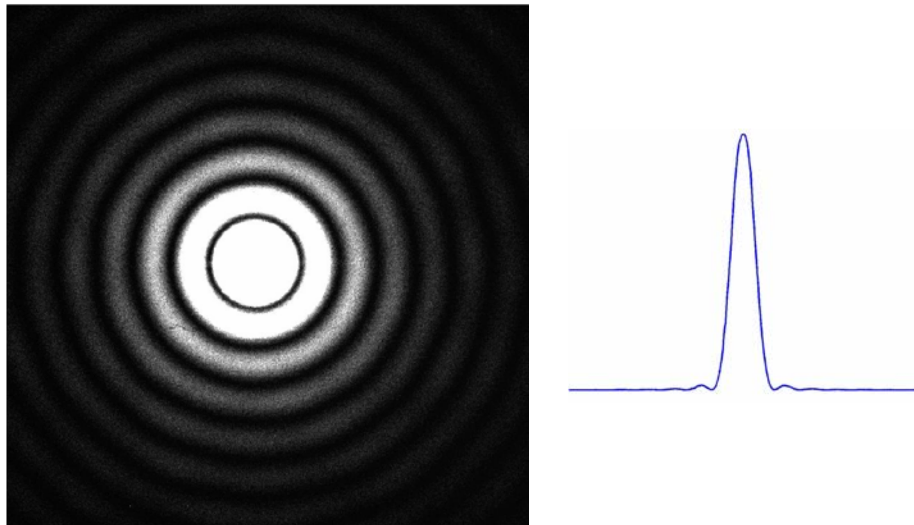

Figure 3-7 Airy pattern and its cross-section recorded using a 2.5μm diameter pinhole at the focal plane of beamline 12.0.2 at the ALS. This picture is recorded at a wavelength of 2.48nm(500eV) with an exposure time of 200 msec.

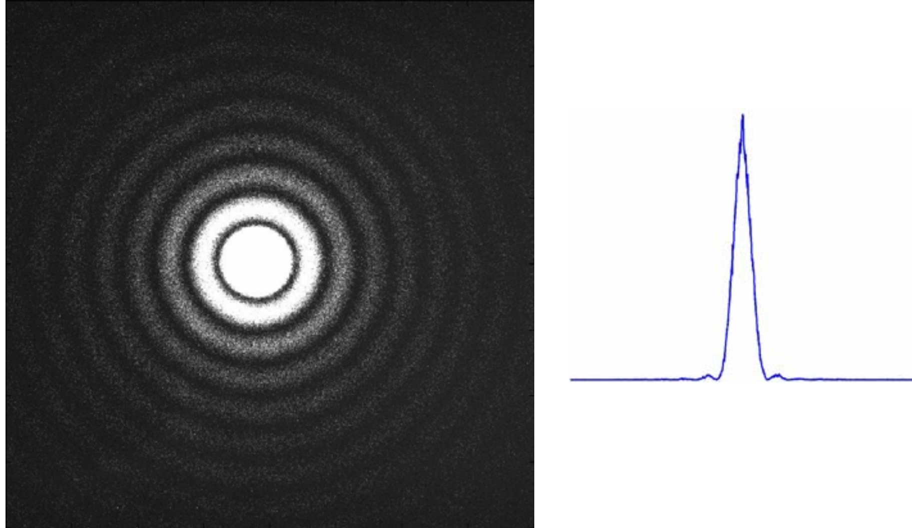

Figure 3-8 Airy pattern and its cross-section recorded using a 2.5μm diameter pinhole at the focal plane of beamline 12.0.2 at the ALS. This picture is recorded at a wavelength of 2.07nm(600eV) with an exposure time of 1 sec. Note that the rings are smaller at 600eV than 500eV, as in figure 3-7, due to the shorter wavelength and thus reduced divergence angle as seen in equation (3-10).

These are the first high-quality airy patterns seen with soft x-ray radiation [59].

Equation (3-9) can be solved to determine the location of the consecutive minima and maxima of the Airy pattern [54]. Specifically, the radial location of the first minima, d, can be expressed as

$$d = \frac{1.22\lambda z}{w} \tag{3-10}$$

Using Matlab [60] to analyze figures 3-7and 3-8, an average radial position of the first minima of 1.7mm and 1.5mm was determined, respectively. Using equation (3-10), this corresponds to a pinhole diameter of 2.5μm. This is the same diameter as was measured using the SEM in section 3.3.

In section 3-4 the flux through the pinhole, or spatially coherent flux, was measured. This is not the spatially coherent flux that will be available for future experiments. In these measurements, the photodiode was placed immediately after the pinhole. This caused the diode to record all of the radiation through the pinhole, including the flux diffracted into the airy rings. Only that flux in the central lobe of the airy pattern will be used in future experiments.

The ratio of the power in the central lobe to the power of the entire pattern can be expressed as [61]

$$\frac{P_{central_lobe}}{P_{total}} = 1 - J_0^2(3.833) - J_1^2(3.833) = 0.8378 \tag{3-11}$$

Using equation (3-11), of the 0.232μA found through the 2.5μm diameter pinhole in section 3-4, 0.194μA is in the experimentally useful central lobe. This corresponds to a spatially coherent flux in the central lobe of

$$flux_{coh,central_lobe} 0.194\mu A \times \frac{1W}{0.164A} = 1.18\mu W\,(@\,500eV) \tag{3-12}$$

$$= 1.48 \times 10^{10} \frac{photons}{\sec}$$

within the central radiation cone bandwidth of 0.61%.

To generate Airy patterns at energies higher than those seen above, greater filtering is required to generate spatial coherence as implied by the van Cittert-Zernike theorem. [35,36] Using a single 500nm diameter pinhole placed at the focal plane of the 14X sub-branch, the Airy patterns shown in figure 3-9 were recorded. The CCD camera used was once again placed 1.44m downstream of the pinhole plane. As the wavelength of the incident radiation decreases, the number of rings visible in the 1”X1” detector area of the CCD increases and the diameter of the central lobe decreases as is implied by equation (3-10).

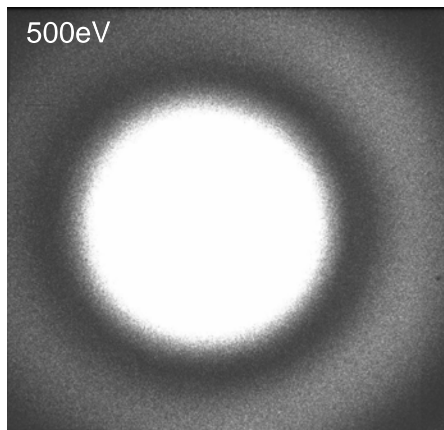

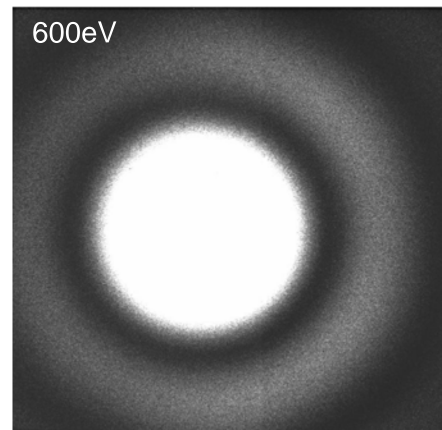

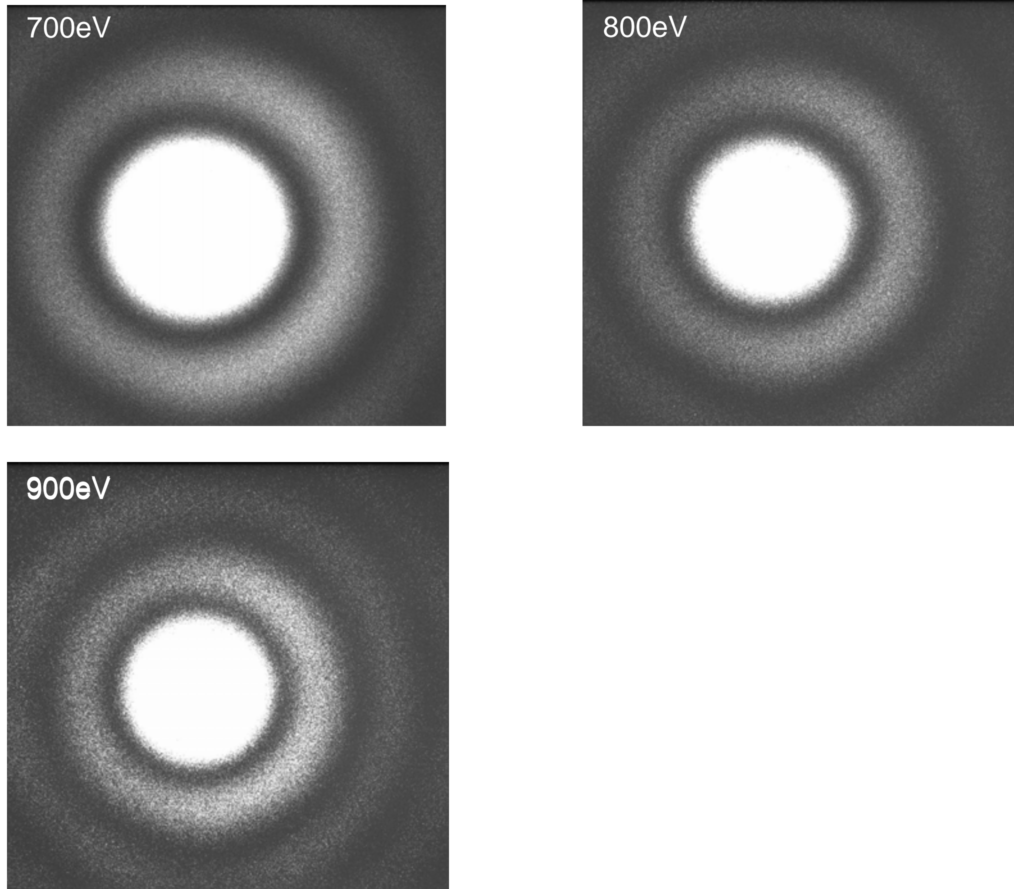

Figure 3-9 Airy patterns recorded using a 500nm diameter pinhole at the focal plane of beamline 12.0.2 at the ALS for energies ranging from 500eV – 900eV.

3.6 Double Pinhole Characterization of Beamline 12.0.2

The first double-slit experiment was performed by its namesake, Thomas Young, in 1802. Young illuminated an opaque screen with two small, closely spaced openings with monochromatic light from a small source. The two waves from the openings interfered on a screen in the far-field causing fringes. With this experiment, Young discovered the principle of optical interference and provided

support for the wave theory of light [62]. In 1957, Thompson and Wolf [25] first used the double-slit setup to experimentally verify theoretical predictions relating to the two-beam interference of partially coherent light. By varying the separation of the two openings, Thompson and Wolf were able to determine the degree of coherence with respect to transverse distance of a mercury-vapor compact source lamp with a wavelength of 579nm.

This section uses the same basic Young's double slit experiment as Thompson and Wolf did to determine the complex coherence factor of the soft x-ray branchline [2, 64-67]. A schematic of the experiment is shown in figure 3-10. In this experiment, the slits in question will be pinholes fabricated as discussed in section 3-5 and placed at the focal plane of the beamline. The soft x-rays pass through the pinholes and then propagate 1.44m to the far field region where they will be detected on the 1"X1" CCD camera discussed in section 3-5.

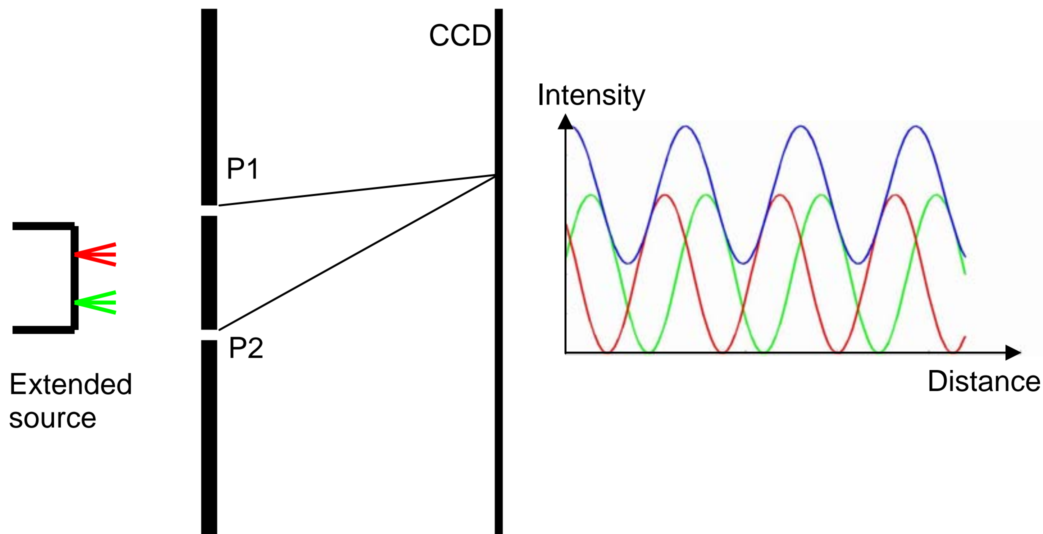

Figure 3-10 Double pinhole experiment setup. An extended source illuminates two pinholes, each point of the extended source creating an interference pattern at the recording plane. The sum of the intensities of these patterns creates the overall intensity distribution.

The uncorrelated emitters of an undulator can be described as an extended source. Identifying two points from the extended source (shown in red and green, respectively, in figure 3-10), after passing through a double pinhole each point creates an interference pattern on the CCD camera. The resultant interference pattern on the CCD will be the sum (blue) of the intensities of these individual patterns. It is the visibility of this resultant pattern that will be used to determine the complex coherence factor of the source.

The visibility can be described as the sharpness of the fringes or [33]

$$Visibility = \frac{I_{\max} - I_{\min}}{I_{\max} + I_{\min}} = \frac{2\sqrt{I^{(P1)} I^{(P2)}}}{I^{(P1)} + I^{(P2)}} \left| \mu_{12} \right| \quad (3\text{-}13)$$

for the quasi-monochromatic case of undulator radiation passed through a monochromator where I_{max} and I_{min} are the maximum and minimum intensity of the fringe pattern, respectively, and $I^{(P1)}$ and $I^{(P2)}$ are the intensities on each of the pinholes. If the double pinholes are centered about the incident radiation such that $I^{(P1)} = I^{(P2)}$ then the visibility is simply equal to the magnitude of the complex coherence factor.

In order to use the simple model of equation (3-13), the wavefront over each individual pinhole must be spatially coherent (μ~1). To determine the diameter of the individual pinhole where this full spatial coherence is achieved, the beamline is once again modeled as a single optic imaging an incoherent source as seen in figure 3-11.

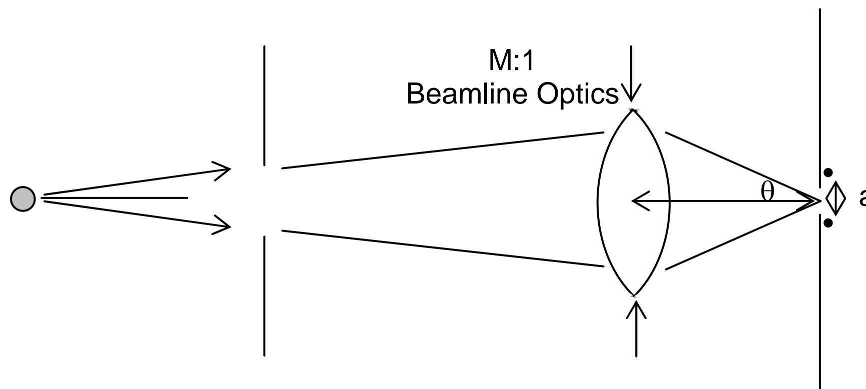

Figure 3-11 Figure of beamline used to determine double pinhole dimensions. The beamline is viewed as one large optic that demagnifies the radiation by a factor of M (8 or 14 depending on the sub-branch).

Following Born and Wolf's [34] calculation, using van Cittert-Zernike, for the degree of coherence in the image of an incoherent light source, the complex

coherence factor between two points a distance “a” apart in the image plane can be shown to be

$$\mu_{12} = e^{-i\psi} \frac{2J_1(ka\theta)}{ka\theta} \tag{3-14}$$

Solving equation (3-14) for a wavelength of λ=2.48 nm (500eV), we find that for a=450nm, $\left|\mu_{12}(ka\theta)\right| = 0.96$. Thus a pinhole diameter of 450nm for each individual pinhole was used for a high spatial coherence wavefront from each pinhole. These individual pinholes are shown in figure 3-4.

Results of the double pinhole characterization performed are shown in figures 3-12, 3-13 and 3-14. These figures display the results of pinholes separated be varying distances in the vertical direction at 500eV, pinholes separated by 5μm in the vertical direction at varying energies, and separated at varying distances in the horizontal direction at 500eV, respectively. The images obtained on the CCD camera are displayed as well as cross-sectional lineouts of the images. A graph of complex coherence factor versus pinhole separation is also shown with a least square error fit Gaussian curve to the experimental data points.

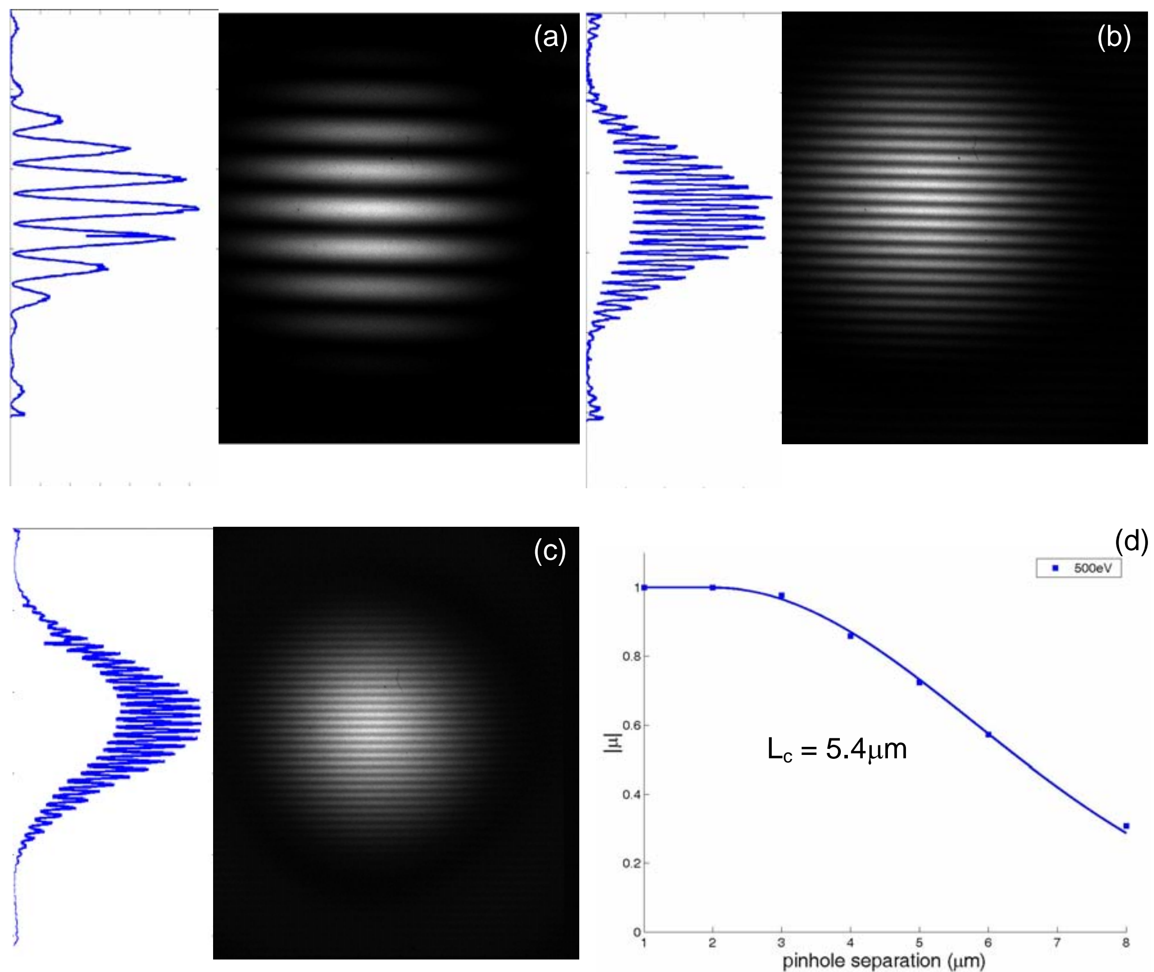

Figure 3-12 Measured two-pinhole interference patterns and their respective lineouts for vertical pinhole separations of (a) 2μm, (b) 6μm and (c) 8μm. Each individual pinhole of the two-pinhole pairs has a diameter of 450nm to insure a spatially coherent wavefront over the individual pinhole. (d) charts the measured magnitude of the complex coherence function versus the pinhole separation. A least square error Gaussian curve is fitted to these data points. All of this data was taken at a photon energy of 500eV (2.48nm) on beamline 12.0.2 of the ALS.

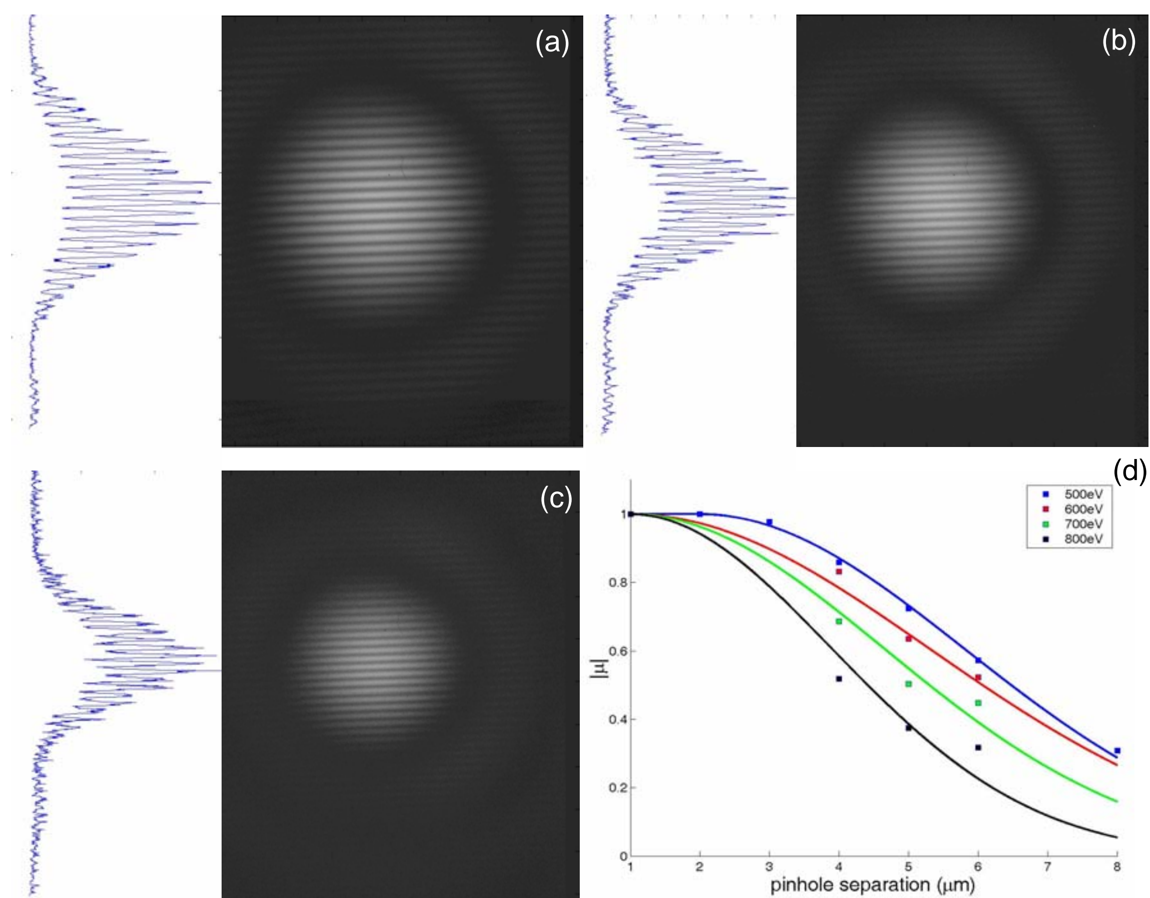

Figure 3-13 Measured two-pinhole interference patterns and their respective lineouts for a 5μm vertical pinhole separation at a photon energy of (a) 600eV (2.07nm), (b) 700eV (1.77nm) and (c) 800eV (1.56nm). The airy envelope decreases for increasing energy, as is implied from equation (3-9). (d) charts the measured magnitude of the complex coherence function versus the pinhole separation for 500eV(blue), 600eV(red), 700eV(green) and 800eV(black). A least square error Gaussian curve is fitted to each energy's set of data points. All of this data was taken on beamline 12.0.2 of the ALS. The coherence lengths as calculated by equation (3-19) are 5.4μm (500eV), 4.9 μm (600eV), 4.2 μm (700eV) and 3.6 μm (800eV).

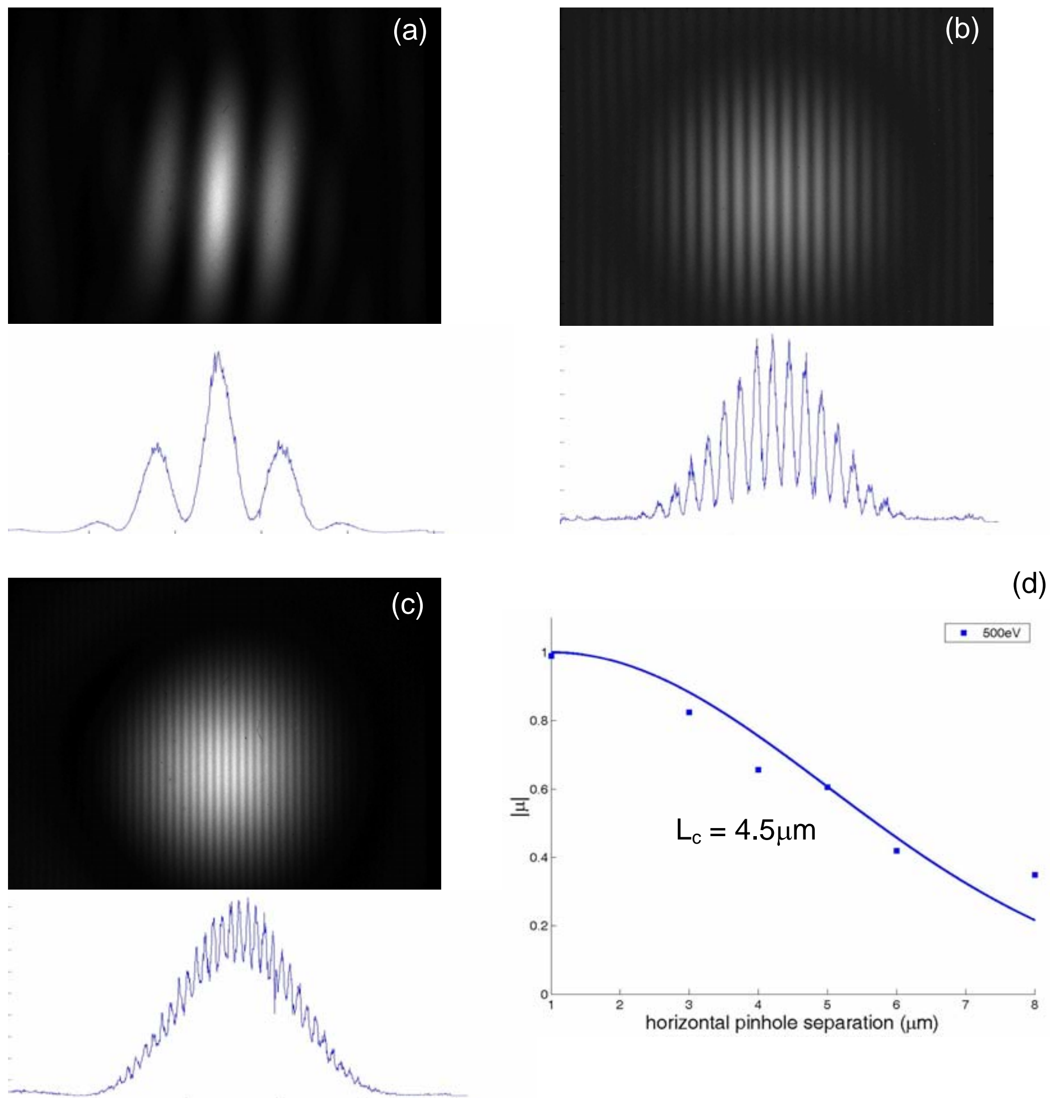

Figure 3-14 Measured two-pinhole interference patterns and their respective lineouts for horizontal pinhole separations of (a) 1μm, (b) 4μm and (c) 8μm. (d) charts the measured magnitude of the complex coherence function versus the pinhole separation. A least square error Gaussian curve is fitted to these data points. All of this data was taken at a photon energy of 500eV (2.48nm) on beamline 12.0.2 of the ALS.

The value of the magnitude of the complex coherence factor is determined from each interferogram in the Fourier domain. Following Goodman, [33], the intensity of the interference pattern on the CCD camera can be expressed as

$$I(x, y) = 2I^{(1)}(x, y)\left[1 + \mu \cos\left(\frac{k}{z} ax + \phi\right)\right] \tag{3-15}$$

where $I^{(1)}$ is the intensity on the CCD due to pinhole diffraction, x is the axis on the CCD that is parallel to the pinhole separation, z is the distance from the pinhole pair to the CCD and ϕ is the fringe shift relative to the geometric center of the interference pattern. Taking a two-dimensional Fourier transform of equation (3-15) yields

$$\begin{aligned} \Im\{I(x, y)\} &= \Im\{2I^{(1)}(x, y)\} * \Im\left\{\left[1 + \mu \cos\left(\frac{k}{z} ax + \phi\right)\right]\right\} \\ &= \Im\{2I^{(1)}(x, y)\} * \left[\delta(f_x, f_y) + \mu \frac{1}{2}\left(\delta\left(f_x - \frac{\lambda}{z} a, f_y\right) + \delta\left(f_x + \frac{\lambda}{z} a, f_y\right)\right)\right] \end{aligned} \tag{3-16}$$

where * denotes convolution. As seen in this equation, in the Fourier domain, the fringe visibility (and thus complex coherence factor) is equal to twice the relative intensity of the first order peak to that of the zeroth order peak [24, 68].

In practice, Matlab is used to two-dimensionally Fourier transform the double pinhole interferogram and then filters are applied to achieve the ratio of the first order peak to the zeroth order peak.

The least squares error fitted Gaussian curves are used to determine the transverse coherence length of the beam with regards to direction and energy.

Following Goodman [33] and Mandel [69] who defined a lateral coherence length defined as

$$L_c = \int_0^{\infty} |\mu(\Delta x)|^2 \, d\Delta x \qquad (3\text{-}17)$$

where the integration variable Δx is the distance between the two pinholes. Defining the complex coherence variable as

$$\mu(\Delta x) = e^{-\frac{(\Delta x - m)^2}{2\sigma^2}} \quad \text{for } \Delta x \geq m$$

$$= 1 \qquad \text{for } 0 < \Delta x < m \qquad (3\text{-}18)$$

where m is the mean and σ is the standard deviation of the fitted Gaussian, the coherence length can then be found to be

$$\begin{aligned} L_c &= \int_0^{\infty} |\mu|^2 \, d\Delta x \\ &= \int_0^{m} |1|^2 \, d\Delta x + \int_m^{\infty} \left| e^{-\frac{(\Delta x - m)^2}{2\sigma^2}} \right|^2 d\Delta x \qquad (3\text{-}19) \\ &= m + \frac{\sigma\sqrt{\pi}}{2} \end{aligned}$$

The lateral coherence lengths determined from the curves given in figure 3-12, 3-13, and 3-14 are summarized in table 3-2. The difference in the coherence length in the vertical versus horizontal direction can be seen as a result of the monochromator. The grating of the monochromator is vertically deflecting element and thus the exit slits of the monochromator are positioned to filter the beam in the vertical direction.

The lateral coherence lengths shown in table 3-2 are greater than what is expected using equation (3-14). The small vertical size and divergence of the electron beam emitted from the undulator results in partially coherent illumination in this vertical direction, however equation (3-14) is for uncorrelated emitters. Also, by using the monochromator to limit the bandwidth of the radiation, the upstream angular aperture is under filled, effectively reducing θ in equation (3-14). Lastly, the model used was for a perfect single optics and neglects the aberrations present in the beamline [70]. Coming out of the undulator, the beam has dimensions of 260μm X 16μm, rms [30] which corresponds with focal spot of 44μm X 2.7μm FWHM. These values are affected by aberrations in the beamline K-B optics, more so in the vertical direction. As shown in figure 3-6, the FWHM of the experimental focal spot is 60μm X 9.4μm FWHM. The ratio of the focal spot size to the coherence length is a constant. As such, as the focal spot size increases due to aberrations, the coherence length also increases.

Energy (eV)	Separation	L_c (μm)
500	Vertical	5.4
600	Vertical	4.9
700	Vertical	4.2
800	Vertical	3.6
500	Horizontal	4.5

Table 3-2 Tabulated values of the experimentally determined lateral coherence length (L_c) versus energy for beamline 12.0.2, consistent with the values determined using van Cittert-Zernike when modified for the complications of beamline optics.

3.7 Beamline Challenges

The beamline characterization results reported above are the final product of many months of beamline optimization. This section presents some of the challenges that were overcome in order to make beamline 12.0.2 operational. Specifically, this section discusses the presence of higher (than 3rd) harmonics, beamline stability and alignment.

When the double pinhole experiment began, the interference patterns presented in section 3-6 appeared with a saturated rectangular area in the center of them as shown in figure 3-15. This image was recorded on the CCD camera 1.44m behind the focal plane, the same as the patterns in section 3-6.

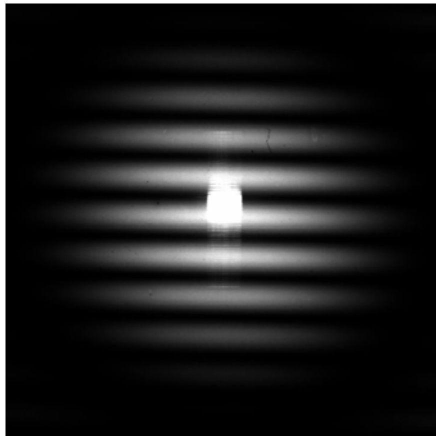

Figure 3-15 Interference fringes with saturated bleed through in a near-axis rectangular region.

The origin of this saturated rectangle was not readily apparent. This rectangle did not appear on the focusing YAG discussed in section 3-4. The pinhole and CCD camera were removed and a YAG was attached ~0.5m behind the focal plane. The rectangle was not displayed at this YAG position, either.

Inspecting figure 3-15 with Matlab, it is seen that the rectangle is approximately 66 pixels (0.164cm) wide in the horizontal direction. To determine if the rectangle was the projection of an artifact in the pinhole plane the 0.164cm width was angularly traced to the pinhole plane using equation (3-4). Doing this, the 0.164cm square on the CCD corresponded to an approximately 1.4μm image at the focal plane. This negligible size at the focal plane, coupled with the discovery that the monochromator exit slit width effected the vertical extent of the rectangle and the "undefined" edges of the vertical side of the rectangle led to the belief that something was being imaged through the beamline (and thus coming to a minimum at the focal plane) and out onto the camera in the projection far field.

This realization was unexpected as anything that was successful at imaging itself through the beamline system was assumed to be absorbed at the pinhole plane. The rectangular artifact showing up at the CCD appeared unaffected by the 0.7μm of gold that was being used as an absorber around the pinholes at the start of the experiment. In order to project through this gold layer, less absorptive, higher energies needed to be involved.

In chapter 2, we discussed the generation of second and third order harmonics. However, the higher order iterative solutions are not limited to the second and third. The critical harmonic describes the harmonic number that for a certain magnet spacing, or K value, will give half of the energy radiated into higher

harmonics and half into lower harmonics. The critical harmonic can be expressed as [30]

$$n_c = \frac{3K}{4}\left(1 + \frac{K^2}{2}\right) \tag{3-20}$$

The 500eV (2.48nm) radiation from the 3rd harmonic at beamline 12.0.2 is maximized for K=1.77. This K value corresponds to a critical harmonic of n_c=3.41. This means that half of the energy being radiated from the U8 of beamline 12 is being radiated into harmonics higher than the n=3 that is utilized by beamline 12.0.2.

For a given energy in the first harmonic, E_o, the electron energy of the higher order harmonics is defined as [37]

$$E = nE_o \tag{3-21}$$

For the 500eV third harmonic radiation that has been of the primary interest, this corresponds to E_5=833.3eV and E_7=1166.7eV. The transmission through the pinhole materials of these higher order harmonics is summarized in table 3-3. As this table shows, the absorption of the seventh harmonic is approximately six orders of magnitude less than that of the third harmonic.

Figure 3-16 plots the power in the central radiation cone versus energy using equation (2-19) of the 3rd, 5th, and 7th harmonics of beamline 12 for $0.5 < K < 4.95$. Although the amount of absorption from the gold is significantly less for these higher orders, the power in the fifth and seventh harmonic is decreased, as

well. This low power still allows for the saturation of the CCD camera for two reasons. First, the number of electrons per photon produced at the CCD camera increases with increasing energy. Second, the higher order radiation is projecting through the gold absorber and thus the entire higher order beam is recorded on the CCD. This is in comparison with the small percentage of the 3rd harmonic beam that is propagating to the CCD camera after being filtered by the pinholes.

		Transmission for:				
n	Energy	0.7μm Gold	12nm Gold	6nm Chrome	0.1 μm Si_3N_4	Total
3	500eV	4.60E-08	0.749	0.984	0.623	2.11E-08
5	833.3eV	5.17E-05	0.844	0.950	0.879	3.65E-05
7	1266.6eV	1.31E-02	0.928	0.982	0.960	1.15E-02

Table 3-3 Transmission of the originally used material thicknesses in the fabrication of the pinholes for the 3rd, 5th, and 7th harmonics associated with K=1.77. K=1.77 maximized the third harmonic power at an electron energy of 500eV. Note the six order of magnitude increase in transmission from the third harmonic to the seventh.

In order for the 5th and 7th harmonics to transmit through the 0.7μm of absorber gold, they must have been able to propagate from the U8 through the beamline to the focal plane. Figure 2-9 plotted the mirror reflectivity with regards to energy of the reflective coatings used in beamline 12.0.2. This plot displays that for these higher energies of the fifth and seventh harmonic, there is not a significant decrease in the reflectivity of the four glancing incidence optics.

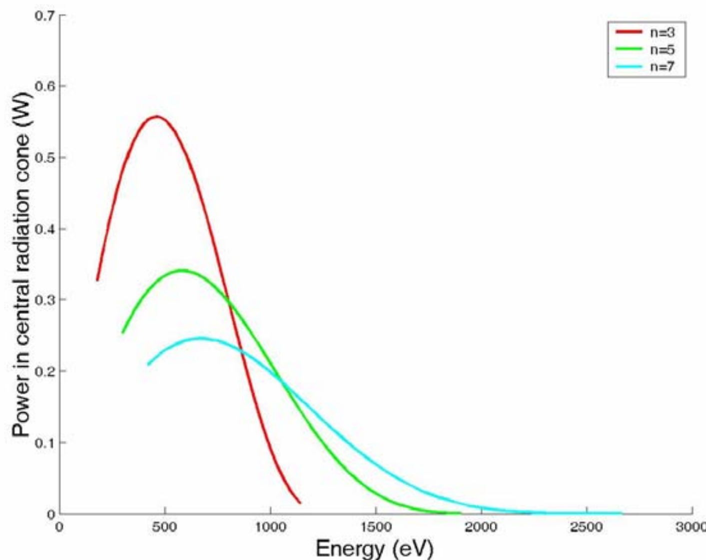

Figure 3-16 Power in the central radiation cone versus energy for the 3rd, 5th and 7th harmonics [37-40] out of the U8 undulator of beamline 12. Values are plotted for 0.5 < K <3.5. Note the decreasing peak power with increased harmonic.

It is less obvious that the higher energies of these higher order harmonics will pass through the beamline monochromator. As previously discussed, the monochromator is made up of a varied line space glancing incidence grating coupled with an exit slit. The grating spreads the radiation for a specific wavelength and then the exit slit selects the specific wavelength. The basic grating equation can be expressed as [71]

$$\theta_q = \theta_i + q\frac{\lambda_o / n}{\Lambda} \tag{3-22}$$

where q is the diffraction order of the grating, θ_i is the incident angle, θ_q is the reflected angle and Λ is the grating period. The wavelength is expressed to include order number, following the convention of equation (3-21). From

equation (3-22), we see that for an increased harmonic, n, there is a matching q such that the reflected angle of the grating remains a constant. This enables the higher orders for a given K to pass through the exit slit of the monochromator.

The element being imaged by the higher order harmonics through the beamline is the angular aperture prior to M2. This angular aperture sets the central radiation cone to that of the 500eV radiation of the third harmonic. It is what limits the beamline to passing central radiation cone radiation at 500eV even when the exit slits of the monochromator are wide open. This aperture was chosen as a square to save in the cost of the beamline. The projection of the aperture appeared as a rectangle rather than a square due to the high levels of spatial coherence in the vertical direction. This coherence is due to the spatial and angular filtering performed in the vertical direction by the exit slit of the monochromator.

To combat the presence of this saturated rectangle, a thicker absorber layer of gold was used with the pinholes. This is the 2.1μm of gold presented in table 3-1. Absorption values for the 5th and 7th harmonic are included in table 3-4.

		Transmission for:				
n	Energy	2.1μm Gold	12nm Gold	6nm Chrome	0.1 μm Si_3N_4	Total
3	500eV	9.71E-23	0.749	0.984	0.623	4.46E-23
5	833.3eV	1.39E-13	0.844	0.950	0.879	9.76E-14
7	1266.6eV	2.27E-06	0.928	0.982	0.960	1.99E-06

Table 3-4 Transmission of the materials used in the fabrication of the pinholes for the 3rd, 5th, and 7th harmonics associated with K=1.77.

Additional challenges of the beamline have been beamline stability and alignment. Heat, vibrations and a "soft spot" in the cement floor of the ALS cause instability of the beam. When someone walks next to the upstream components of the beamline, movement of the beam can be seen on the focusing YAG. In order to maintain a stable beam for experiments, it is beneficial to perform this work late at night when there are fewer disturbances.

Accurate placement of the first mirror, M0, is critical to achieving the high flux found in the beamline characterization. If this mirror is not positioned precisely, the beam will not be deflected into beamline 12.0.2 correctly. M0 is mounted on a strut system to align it. The heat from placing one's hand on one of these struts causes enough movement on M0 to lose beamline alignment. To regain an optimized position for M0, adjust the struts to maximize the current detected on a diode placed behind the focal plane of the 14X sub branch. This adjustment should be performed at 500eV with the exit slits of the monochromator set for the central radiation cone bandwidth.

A final beamline challenge is the wavelength accuracy of the monochromator. Monochromators made up of varied line space gratings coupled with an exit slit have been quite successful in the extreme ultraviolet region. This extension to the to the soft x-ray region demands greater performance out of the monochromator calibration and exit slit position then before.

A calibration of the monochromator is performed each shift by scanning the grating and detecting the fluorescence from a downstream mirror. When the grating is angled such that it is reflecting its zeroth order through the exit slits it acts like a mirror and the whole spectrum of the undulator is passed. The peak of this reflection is measured and set to λ=0. Comparing this method of calibrating the monochromator with calibration performed by using the visibility from a material's absorption edge, it is seen that the monochromator calibration can be "off" by up to a 4eV difference. Although this is a large number in photon energy units, it is a small value in wavelength (0.02nm about 500eV.) For data collection where wavelength accuracy is critical, a scan about a material's absorption edge is required.

3.8 Conclusions

This chapter experimentally characterized the new coherent soft x-ray branchline at the ALS. A central radiation cone flux level was found within a factor of 2 of what was theoretically expected. The spatially coherent flux was lower by a factor of 4. The first high quality soft x-ray airy patterns were presented. The magnitude of the complex coherence function was determined in the vertical and horizontal direction by performing a double-pinhole experiment. Lastly, higher harmonic and alignment challenges in establishing the beamline were discussed.

Chapter 4

Interferometry - Material Testing

4.1 Introduction

Interferometers are instruments designed to take advantage of the fringe patterns resulting from two light beams that interfere after traveling different optical path lengths. These instruments have been in use for almost 200 years. Applications of interferometry are extremely diverse and range from the measuring of small defects in a surface to studying airflow about an airplane wing to creating a 3D map of the earth. The physical setup of interferometers fall into two categories: wavefront division interferometers and amplitude division interferometers. In amplitude division interferometers, a beam splitter is used to divide the initial beam into two parts that are later re-joined to create fringes. In wavefront division interferometers, portions of the initial beam are used as sources to emit secondary waves that later overlay and interfere. At EUV and SXR wavelengths, wavefront division interferometers are employed as effective beam splitters are not available due to the near unity value of the index of refraction. [72-74]

This chapter presents an interferometric experiment designed to measure index of refraction. First, index of refraction is defined and previous methods used to determine index of refraction are reviewed. Next, the experiment itself is discussed in two categories: EUV measurements and SXR measurements. Both sets of measurements were made on beamline 12 at the ALS; the EUV

measurements were made on the older bl12.0.1.2 and the SXR measurements were made on the new bl12.0.2.1, which was characterized in chapter 3. For both sets of measurements, the experimental setup is presented, methods for data analysis are discussed and the results are presented. The experimental results are compared with results from prior measurement methods.

4.2 Index of Refraction – definition and previous work

The interferometer discussed in this chapter is used to measure the index of refraction of several materials in the EUV and SXR region. In the EUV region, ruthenium, tantalum silicon nitride, and silicon, three materials important in EUV lithography, are measured. Ruthenium is used as a capping layer for the multilayer mirrors used in EUV lithography. Tantalum silicon nitride is a highly absorptive material being considered as an absorber for phase shift masks. [75] Lastly, silicon is often utilized for multilayer mirrors.

In the SXR regime, chromium and vanadium are measured. Both of these materials have absorption edges near 500eV, the energy about which beamline 12.0.2.1 is optimized.

As stated in chapter 2, the frequency dependent index of refraction can be defined as

$$n(\omega) = 1 - \delta + i\beta \tag{2-30}$$

Inserting (2-30) into the wave equation yields an equation that can be factored into three distinct parts. [47]

$$E(r,t) = E_o e^{-i(\omega t - k \cdot r)}$$

$$E(r,t) = E_o e^{-i\omega\left(t-\frac{r}{c}\right)} e^{-i\left(\frac{2\pi\delta}{\lambda}\right)r} e^{-\left(\frac{2\pi\beta}{\lambda}\right)r} \qquad (4\text{-}1)$$

The first term of equation (4-1) represents the propagation of the wave in a vacuum. The second term is the amount of phase shift the wave will experience as it travels through a material with a real part of the index of refraction, δ, and a thickness r. The final term describes the attenuation of the wave as it propagates through a material with an imaginary part of the index of refraction, β, a distance, r. With equation (2-30) defined such that the sign on the β term is positive, increasing β in equation (4-1) corresponds with wave decay rather than wave amplification.

This is not the first index of refraction determination on these materials at these wavelengths. Henke, Gullikson and Davis [76] compiled all elements on the periodic chart ranging from hydrogen to uranium (1-92), at energies from 30eV – 30keV(41nm wavelength - 0.041nm). The index of refraction was determined by measuring the absorption of radiation through thin foils (or gases) of the element of interest. This absorption could then used to determine β as seen in equation (4-1). In order to determine δ from this absorption measurement, the Kramer's Kronig relations [77, 78] were used. This measurement technique is extremely successful at making β measurements over a broad spectrum. A detriment of

this measurement technique is the indirect determination of δ. At an absorption edge, the value of β increases as a step function. This is a very difficult measurement to make. Any error in this measurement at the edge is then transcribed to the δ measurement. Also, the data taken to establish β did not include bound-bound electron transitions, Near-Edge X-Ray Absorption Structure (NEXAS) or Extended X-Ray Absorption Fine Structure (EXAFS). In using the Kramers-Kronig relations, this error would appear in the δ values as well.

Index of refraction measurements have also been made by Soufli and Gullikson [79] using reflectance. Here the data is collected in the form of reflectance curves where the index of refraction is extracted by using the least squares fitting of Fresnel coefficients. As this is a reflectance measurement, its accuracy is sensitive to surface roughness, chemistry and contamination. This measurement also works best when $\delta/\beta << 1$.

The interferometric method employed in this chapter is a modified phase shifting point diffraction interferometer (PS/PDI) [80] that was developed by C. Chang at EUV wavelengths [2]. This method offers the ability to determine the real and imaginary part of the index of refraction independently. As this is a transmission interferometer the effect of surface contamination is minimized when the thickness of the contaminants is small with respect to the thickness of the sample.

4.3 EUV Experiment

Experimental Setup and Data Acquisition

The experimental setup conceptually used in the index of refraction measurements is shown in figure 4-1. In this experiment, extreme ultraviolet radiation is diffracted from a pinhole placed at the focal plane of beamline 12.0.1.2. It then illuminates a grating, which spreads the illumination into several orders. The +1 and –1 orders from the grating are focused by the zone plate to the sample mask and propagated to the CCD camera where the interference is recorded.

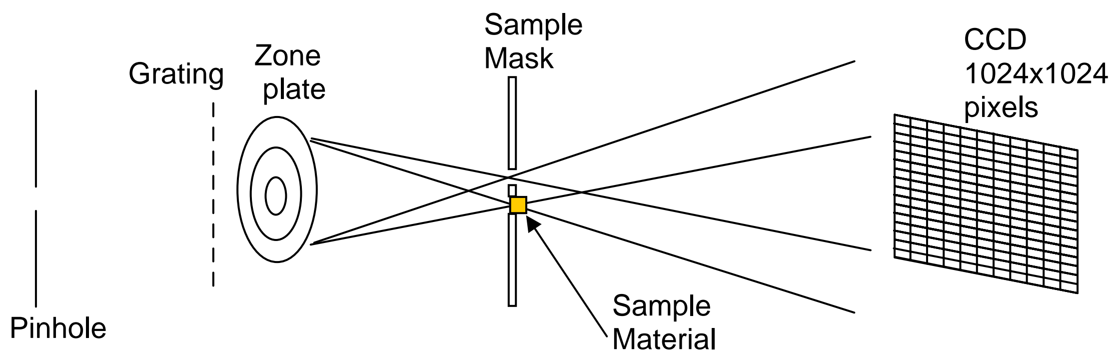

Figure 4-1 Intuitive experiment setup for material measurement.

Figure 4-1 is the experimental setup "conceptually" used in the index of refraction measurements, not the actual setup. Each time an optical element is included in the experimental setup the overall system efficiency decreases. This is due to the efficiency of the element (diffraction into a particular order) as well as to the absorption of the 0.1μm Si_3N_4 film that all of these elements are built upon. Chang [81] designed an element composed of a bit wise exclusive-or of a zone

plate and a grating (XOR). This element creates two off-axis foci, the same as a grating coupled with an zone plate, but with an efficiency approximately 10 times higher. This higher efficiency allows for experimentally tolerable exposure times as well as much easier experimental alignment.

Figure 4-2 displays the experimental setup actually used for the extreme ultraviolet measurements. The pinhole used has a 5μm diameter and is fabricated the same as shown in figure 3-2. The stage upon which the pinhole is mounted has three degrees of freedom. Movement in the z direction is critical to optimize the flux through the pinhole due to the small depth of focus of the beamline at these wavelengths.

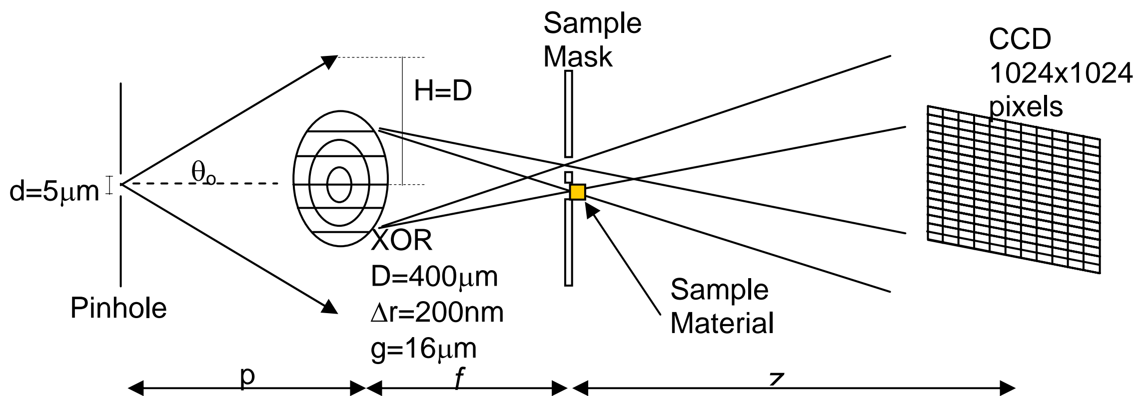

Figure 4-2 Experimental setup for material testing.

The XOR is placed a distance *p* downstream of the focal plane. This distance is chosen such as to overfill the XOR with central Airy lobe radiation diffracted from the pinhole. This distance can be solved for using equation (3-6). As the wavelength range needed in these measurements will only vary by 1.7 nm, the XOR location for twice filling by the beam will only move 17 nm. Because of this

small distance, the XOR was placed at 100mm downstream from the pinhole and not moved throughout the experiment. This made alignment of the system easier, and data collection quicker. The XOR used in the EUV experiments has a diameter, D, of 400μm, an outer zone width, Δr, of 200nm and a grating period, g, of 16μm. Its absorber material is 200nm of nickel. [81]

The sample mask is placed at the focal plane of the XOR, which is the same as the focal length of a zone plate, defined [82]

$$f \approx \frac{D\Delta r}{\lambda} \tag{4-3}$$

For 13.4 nm (92.5eV) this is a focal length of 5.97mm.

Although the focal length of the XOR is a function of energy, the foci separation, Δx, is not. This is experimentally important as the sample mask is made with standard processing techniques and is not mutatable after fabrication. The foci separation can be expressed as

$$\Delta x \approx \frac{2\Delta r D}{g} \tag{4-4}$$

For the XOR described in figure 4-2, this equates to a foci separation of 10μm.

The sample mask is fabricated by the Center for X-ray Optics nanofabrication team, as shown in figure 4-3 [55].

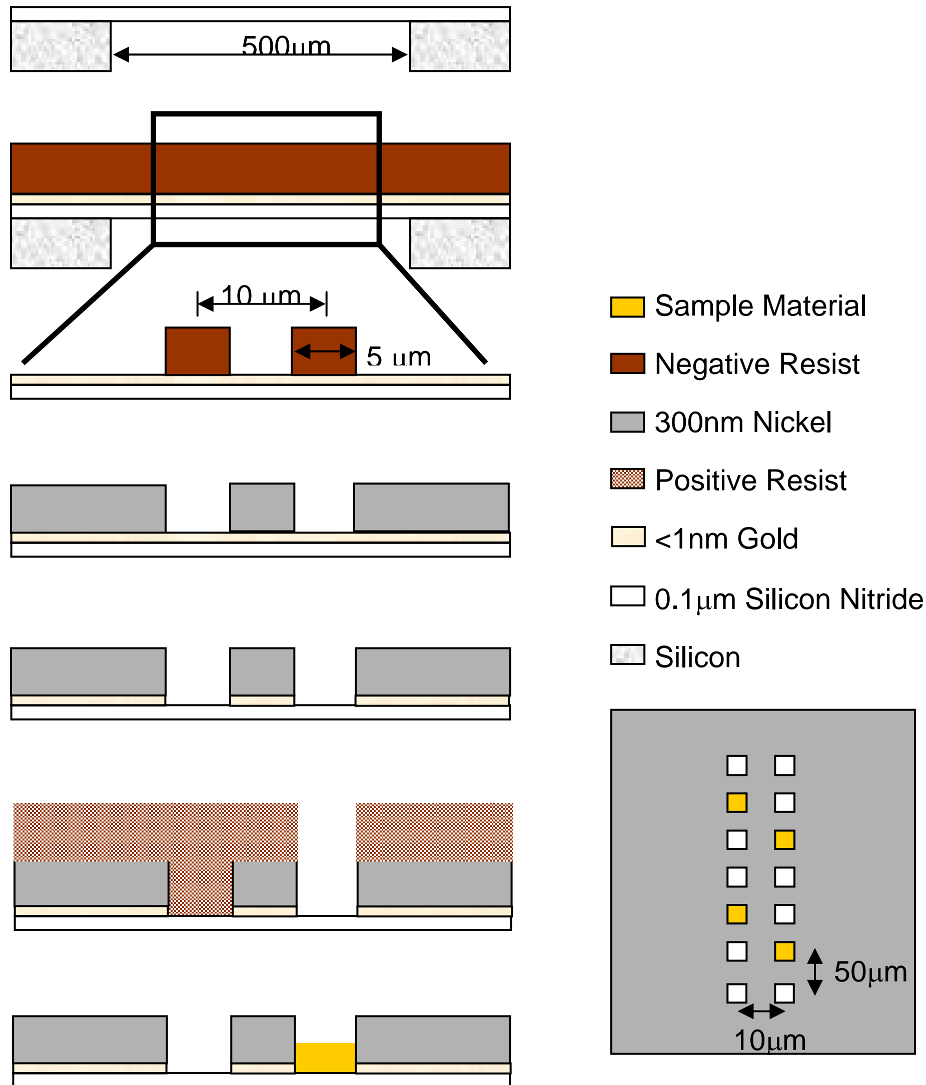

Figure 4-3 Fabrication process for sample mask used to directly measure the index of refraction of the sample material.

The sample mask fabrication process begins with a silicon wafer with a 0.1μm thick silicon nitride window stretched across a 500μm X 500μm square back opening, the same as used in the pinhole fabrication process. Less than 1nm of gold is deposited on the silicon nitride to act as a plating base. Negative resist is

spun on the plating base and then patterned with the e-beam nanowriter so that only the 5μm by 5μm squares where the XOR focused beam will pass are left. Next, 300nm of nickel is electo-plated onto the gold to act as an absorber material for the sample mask. The resist is removed and the plating base is dry etched away. Next, positive resist is spun on and e-beam patterned to reveal the four windows where the sample will be deposited. The pattern of the sample windows is shown in figure 4-3 and will be discussed below. The sample material is sputtered on and the resist is removed with acetone. [55]

After the sample mask, the two wavefronts propagate a distance z to the CCD camera where the interference pattern is recorded. The CCD camera used is the same camera described in section 3-5. The camera is attached to the experimental chamber 405mm downstream of the pinhole plane, thus $z = 405\text{mm} - p - f(\lambda)$.

Correct alignment of the experimental setup shown in figure 4-2 is critical for accurate data acquisition. The alignment is done starting with the pinhole and then adding one element at a time. The diode of section 3-2 is placed behind the 5μm pinhole and the pinhole and diode are iteratively moved until the current on the diode is maximized, centering the pinhole in the beam. When the pinhole has radiation incident on it during alignment, and during data acquisition, low pressures of oxygen are blown onto the pinhole. This oxygen enables the small

pinholes to remain clear of contaminants, such as carbon, which can clog the pinhole.

Next in the alignment process, the diode is moved from blocking the pinhole radiation and the diffraction of the pinhole on the CCD is inspected. Leaving the camera running in <focus> mode so that images are continuously being updated on the screen for feedback, the camera is moved until the Airy pattern is centered horizontally and vertically on the 1”X1” chip. The camera is run in subset mode so that only 1 in 4 pixels is used (254 pixels X 254 pixels) in order for the image to update in a timely manner.

Next the chamber holding the translation stages for the XOR and sample is vented to atmospheric pressure with nitrogen so that the XOR can be inserted. The upstream downstream position of the XOR is located mechanically while the system is at air. The system is pumped back to ~μT pressures for the centering of the XOR in the x/y directions. Using the electric stages, the XOR is moved until the interference pattern is centered on the CCD camera and the illumination appears circularly symmetric.

Lastly, the chamber is vented to atmospheric pressures once again so that the sample can be inserted onto the sample stage. The chamber is pumped and the sample is aligned in all three directions with the electric stages. As seen in figure 4-3, the sample mask is made up of seven window pairs. The first, fourth and

seventh window pairs are clear of sample material and are used to obtain three reference wavefronts. The other four windows pairs have one sample window each, two on one side, two on the other. These four window pairs are used to obtain fringes with the sample material information. Thus for each energy, seven data points are taken.

Alignment of the sample mask is also performed with the CCD camera running in the “focus” mode. Exposure times for the focusing run from 0.02 sec – 1 sec depending on what energy alignment is performed at.

Sample mask alignment is first performed in the vertical, y, direction. The XOR-sample mask combination will create many off axis interferograms. The sample mask is translated in the y direction until the brightest of the interferograms is recorded on the CCD camera. This is the image created from the +1 and –1 orders of the XOR. Next, the sample mask needs to be moved to the correct position in the z direction. The beam diameter is at a minimum at the energy dependent focal plane of the XOR. To see if the sample mask is at this focal plane, the sample mask is slowly moved in the vertical direction until the interferogram disappears. When the interferogram disappears slowly such that part of the interferogram is visible while the rest is not, the sample mask is not centered. The sample mask is then moved in the z direction and the vertical movement is repeated. When the sample mask is moved in the vertical direction and the interferogram disappears all at once, the sample mask is at the

minimized beam diameter and thus the focal plane of the XOR. The depth of focus of the XOR is the same as that for a zone plate. It can be expressed as [82]

$$\Delta Z \approx \pm \frac{2\Delta r^2}{\lambda} \qquad (4\text{-}5)$$

For an energy of 92.5eV and the XOR parameters shown in figure 4-2 the depth of focus is 5.97μm. This relatively small depth of focus allows for an ease of z-positioning of the sample mask as small z-movements offer much feedback.

In the horizontal, x, direction, there are seven different interferograms. This corresponds to the 7 sample mask window pairs. The window pairs are separated by 50μm or 1500 counts of the sample stage. The first or the seventh interferogram of these interferograms is first located and then re-centered in the y-direction. The full-field (1024pixels X 1024 pixels) of the CCD is used to expose an image of the interferogram. The exposure time of this interferogram is chosen such that the median number of counts (electrons recorded, proportional to the number of incident photons) of the interferogram is greater than 10,000. The maximum number of counts of the CCD is approximately 60,000, limited by the dark current on the CCD and pixel overflow near saturation. The noise seen on the CCD has a count level of ~100. Recording greater than 10,000 counts allows for the noise to be <1% of the image. The exposure time for a single interferogram ranges from 0.1sec – 60sec depending on the energy that the sample is being measured at and the sample that is being measured.

It is critical that the seven interferograms are taken within as short a time period as possible. The beam from the undulator is not infinitely stable, it will move slowly with respect to time. This change in upstream illumination needs to be avoided to minimize experimental error. Shorter individual exposure times are important so as to minimize the effects of vibration. After the first interferogram is taken, the pinhole and XOR must not be moved during the seven recordings as this, too, will change the upstream illumination. It takes approximately 30 minutes to acquire all seven interferograms for a specific energy. After the seven are taken, the undulator gap and monochromator are set for the next energy of interest and the sample mask alignment process is repeated. This highlights a detriment of this method of index of refraction measurements: it is quite time-consuming and thus demanding of beamtime.

Data Analysis

The data analysis is approached in two distinct ways. First we will look at cross sectionals lineouts of the interferograms. These cross sections will allow for a rough estimate of the index of refraction. In practice, these lineouts are used during the experiment to determine if the experiment is working properly. Second, we will examine the interferograms in the Fourier domain. Although more time consuming then the lineout method, the Fourier transform method offer much more accurate values for the index of refraction as it takes into account the entire interferogram. The Fourier transform method of data analysis is performed after all data acquisition is completed.

Figure 4-4 (a) shows an interferogram taken in the EUV region. This interferogram is taken of a 287nm thick sample of silicon at 99.6eV(12.4nm wavelength). Note the saturated inner circle of the interferogram. This portion of the interferogram will not be used in data analysis.

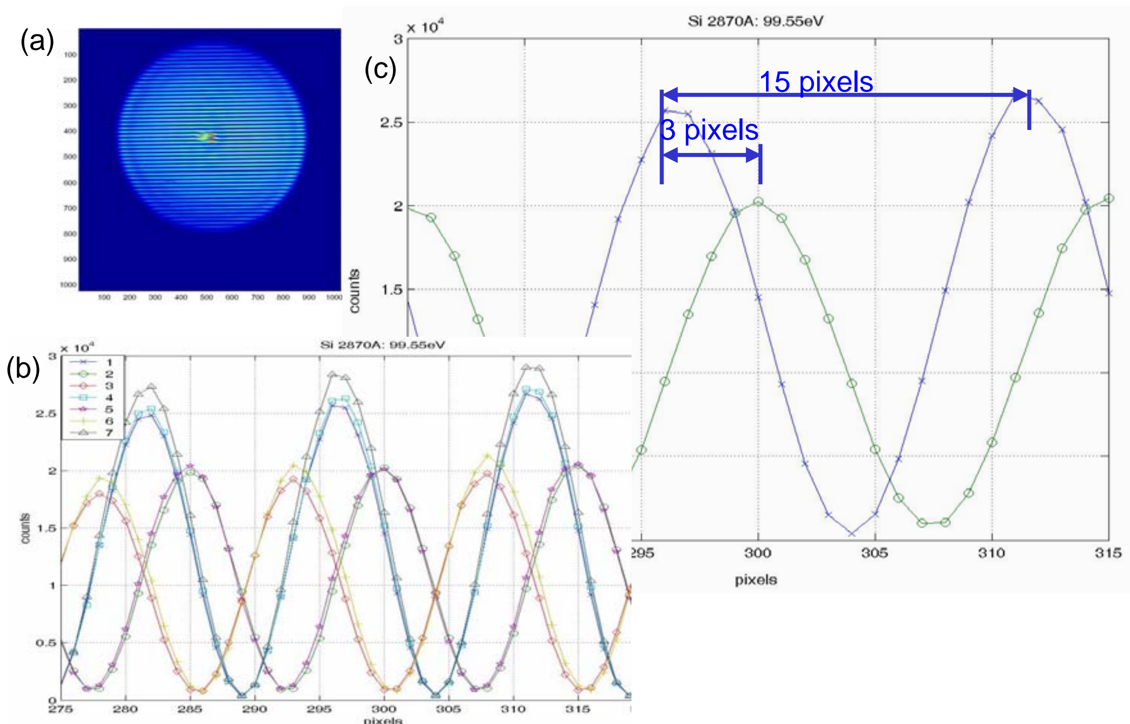

Figure 4-4 Rough data analysis for the 287nm thick silicon sample taken at 99.6eV(12.4nm) (a) sample interferogram (b) cross-sectional lineouts of the seven silicon interferograms taken. These lineouts run from pixel 275 to pixel 320 in the vertical direction at a horizontal pixel location of 375. The fringes are marked at each discreet pixel point. (c) close up of a sample and reference lineout.

The lineouts of figure 4-4 (a) and the six other interferograms associated with this energy point are shown in figure 4-4 (b). The lineout covers approximately 45

pixels (~4% of the length of the interferogram) and avoids the saturated inner region. The three “clear” window pairs produce the high magnitude fringes. The sample window pairs produce the lower magnitude offset fringes. Two sets are shifted in one direction and two are shifted in the other, based on whether the material was on the right or left side of the sample mask of figure 4-3. Figure 4-4(c) offers a close-up of two of the lineouts. Inspecting this close-up reveals that there are approximately 15 pixels in one period of the fringe and that the sample fringe peak is shifted approximately 3 pixels from the reference fringe peak. Extracting the phase shifting part of the wave equation from equation (4-1) gives

$$\phi_{rad} = \left(\frac{2\pi\delta}{\lambda}\right) r \tag{4-6}$$

or

$$\delta = \left(\lambda \phi_{waves}\right) \frac{1}{r} \tag{4-7}$$

where $\phi_{waves} = 2\pi\phi_{rad}$ For the phase shift of $\phi_{waves} = -3/15 = -0.2$ seen in figure 4-4(c), this corresponds to a δ = -0.0087.

Inspecting the magnitude of the two lineouts in figure 4-4 (c) reveals the magnitude of the intensity of the reference fringe is approximately 26000 counts. The magnitude of the intensity of the sample fringe is approximately 20000 counts. Working again from equation (4-1), the intensity of the electric field can be expressed as [47]

$$I = |E|^2 = I_o e^{-\left(\frac{4\pi\beta}{\lambda}\right) r} \tag{4-8}$$

Assuming the thickness of the Si_3N_4 and plating base layers is equivalent in both window pairs, the imaginary part of the index of refraction can be expressed as

$$\beta = -\left(\frac{\lambda}{4\pi r}\right)\ln\left(\frac{I_{sample}}{I_{reference}}\right) \qquad (4\text{-}9)$$

For the interferograms shown in figure 4-4 (c), equation 4-9 gives

$\beta = 9.06 \times 10^{-04}$.

The above data analysis is a valuable tool during data acquisition as it gives a quick rough estimate of what index of refraction values are expected. This method, however, yields large errors as it uses only a small fraction of the interferogram and is pixel limited. The Fourier transform method [2, 83] determines more accurate values for the index of refraction. Figure 4-5 details the method for determining the real part of the index of refraction.

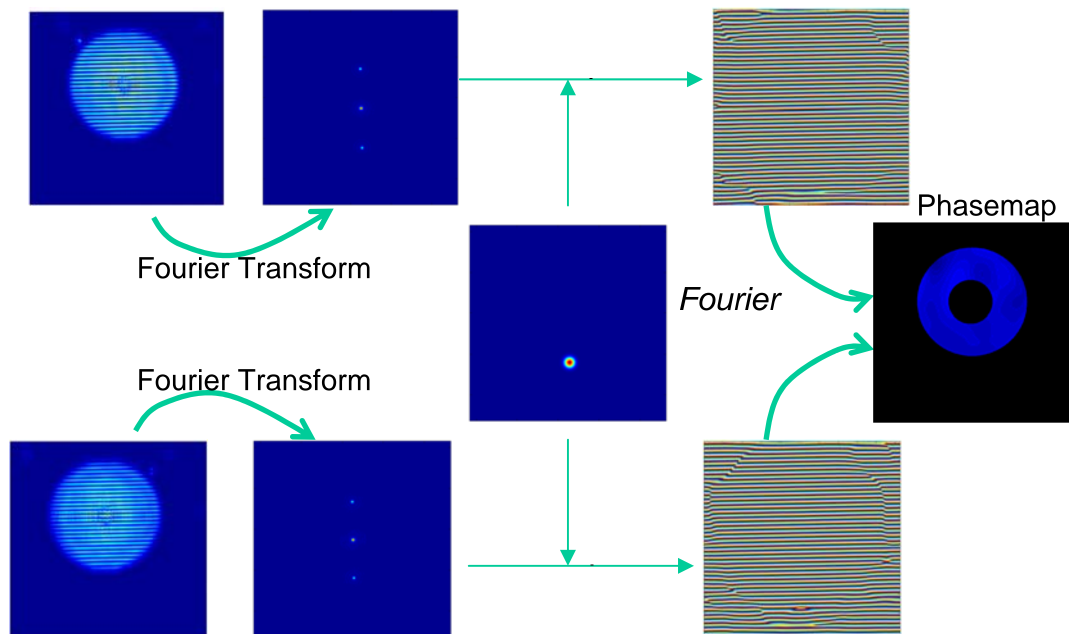

Figure 4-5. Schematic of Fourier approach to data analysis to achieve the real part of the index of refraction [2].

Figure 4-5 begins with two interferograms. One is for a “clear” reference window pair and one is for a sample window pair. Using Matlab, the interferogram is first two-dimensionally Fourier transformed. This Fourier transform reveals three peaks in the Fourier domain. A filter is then applied to this Fourier domain image so that only the +1 peak survives. This rids the image of stray light having different spatial frequencies than the interferograms fringes. These images are then two-dimensionally inverse Fourier transformed back to the image plane. The phases of the two images are compared, leaving the resultant phase map. These phase comparisons are performed between each combination of clear and sample window pairs, yielding 12 phase measurements. The average of these 12 phase values is then applied to equation (4-7) to achieve δ. The variation in these twelve phases is what results in the error bars of this data. Note the donut like appearance of the final phase map. The center region of the initial interferogram is removed as this contains the saturated region.

The imaginary part of the refractive index is determined from the visibility of the interferograms. First, the visibility of each interferogram is determined as was done in section 3-6. Defining $\alpha = I^{P1} / I^{P2} = I_{sample} / I_{reference}$ and inserting this into equation (3-13) the visibility can be defined as

$$V = \frac{2\sqrt{\alpha}}{1+\alpha} \tag{4-10}$$

Solving for α and inserting into equation (4-9) then yields the imaginary part of the index of refraction. This is averaged over the twelve combinations of sample

to reference window pair. The variation in these twelve combinations is what leads to the error bars of this data.

Results

In the EUV region, three sample materials were measured: ruthenium, silicon and tantalum silicon nitride with argon. The index of refraction of ruthenium and $Ta_{57.68}Si_{26.46}N_{14.42}Ar_{1.44}$ are of interest at and close to 13.4nm (92.5eV) for EUV lithography applications. Silicon is also of interest at 13.4nm as well as about its L_2 and L_3 absorption edges (99.8eV and 99.2eV, respectively). The thickness of these samples was chosen as a tradeoff between maximizing the phase shift that the material will display and minimizing the absorption of the sample material. The expected phase shift and absorption were estimated using values found at [84]. In order to measure the index of refraction about silicon's absorption edge, two thicknesses were used. The thicker sample yielded high phase shift with low attenuation below the absorption edge. The thinner sample aided in getting data above the absorption edge where the attenuation is high. The sample thicknesses chosen are shown in table 4-1.

Material	Thickness
Silicon	178nm, 287nm
Ruthenium	56nm
$Ta_{57.68}Si_{26.46}N_{14.42}Ar_{1.44}$	50nm

Table 4-1 Material thicknesses used for EUV index of refraction measurement.

The results for the EUV index of refraction measurements are shown in figures 4-6, 4-7, and 4-8. These figures display the results for ruthenium, $Ta_{57.68}Si_{26.46}N_{14.42}Ar_{1.44}$ and silicon, respectively. For ruthenium and silicon, the experimental data is referenced against tabulated values for the atomic scattering factors, f^o, of these materials (shown in red) found using absorption measurements [85]. From the atomic scattering factors, the real and imaginary parts of the index of refraction were calculated using equations (4-11) and (4-12) [47], respectively, where n_a is the atomic density and r_e is the classical electron radius.

$$\delta = \frac{n_a r_e \lambda^2}{2\pi} f_1^0(\omega) \tag{4-11}$$

$$\beta = \frac{n_a r_e \lambda^2}{2\pi} f_2^0(\omega) \tag{4-12}$$

Reference data for $Ta_{57.68}Si_{26.46}N_{14.42}Ar_{1.44}$ and $Si_{93.96}Ar_{5.98}In_{0.06}$ was determined from the weighted sum of individual index of refraction measurements [84]. This is shown in green in figures (4-7) and (4-8).

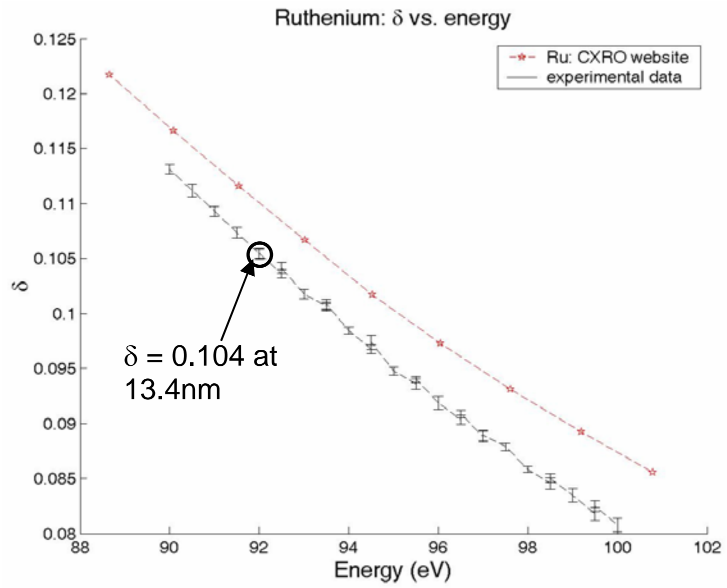

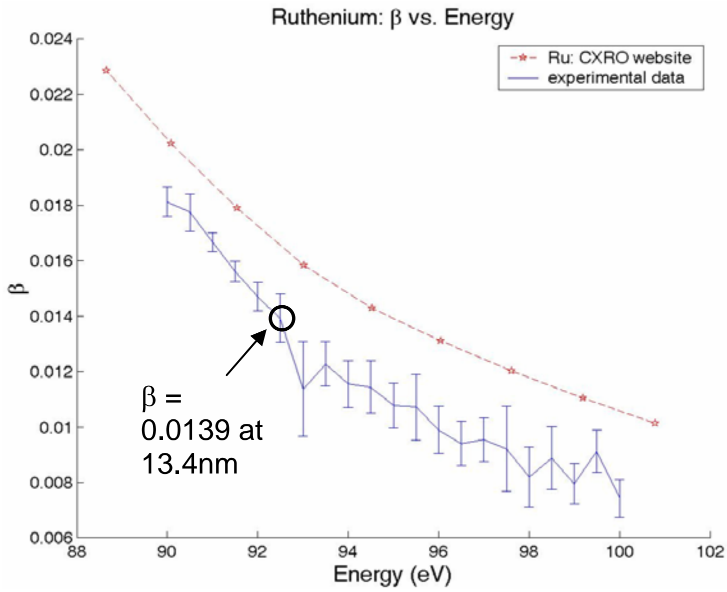

Figure 4-6 (a) δ and (b) β measurements taken about 92.5eV (13.4nm) for ruthenium. The experimental data is shown with error bars and referenced against data taken using absorption measurements [85]. The error bars on the data are a result of changing upstream alignment of the system due to the time of data acquisition.

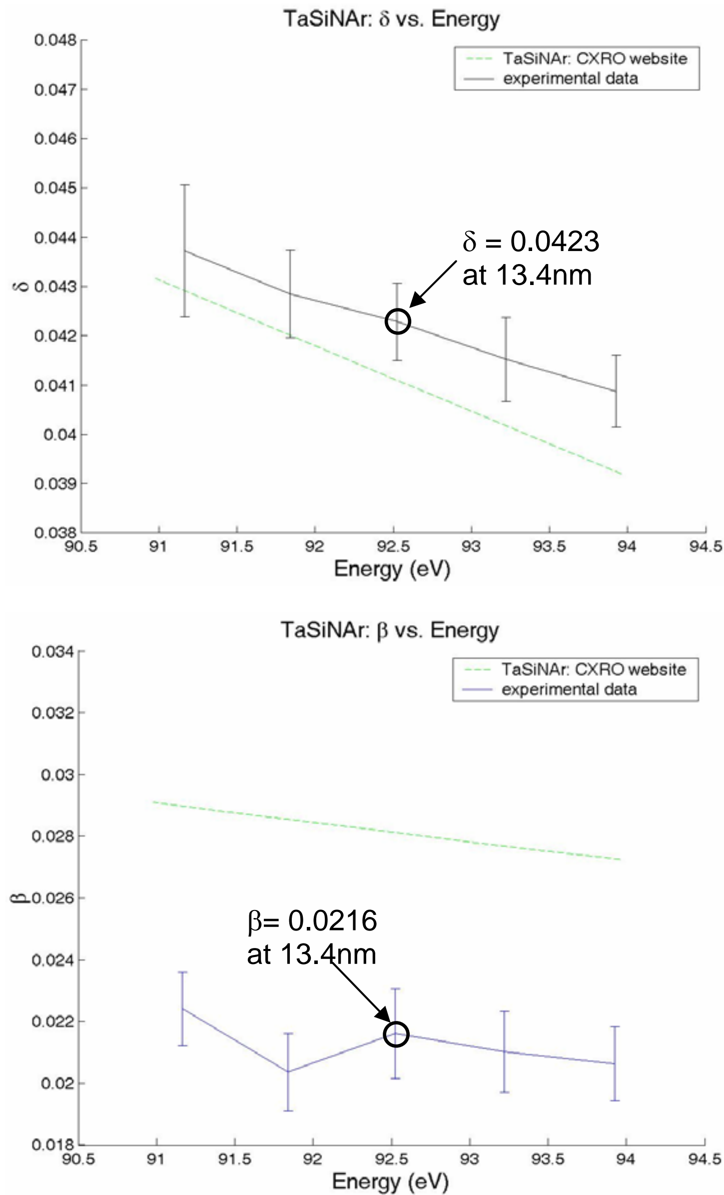

Figure 4-7 (a) δ and (b) β measurements taken about 92.5eV (13.4nm) for $Ta_{57.68}Si_{26.46}N_{14.42}Ar_{1.44}$. This work was performed in conjunction with Motorola, where the sample material was deposited and Rutherford Back-Scattering measurements performed. $Ta_{57.68}Si_{26.46}N_{14.42}Ar_{1.44}$ is a highly absorptive material and as such is being considered as an absorber layer in EUV lithography phase shift masks [75,86,87]. This highly absorptive nature, however, creates great difficulties in taking accurate visibility measurements, and thus β, of this material. A density, ρ, of 11.914 (g/cm^3) and atomic

weight, A, of 114.40 g/mole were used in these calculations. These constants were chosen based on RBS measurements performed by Motorola.

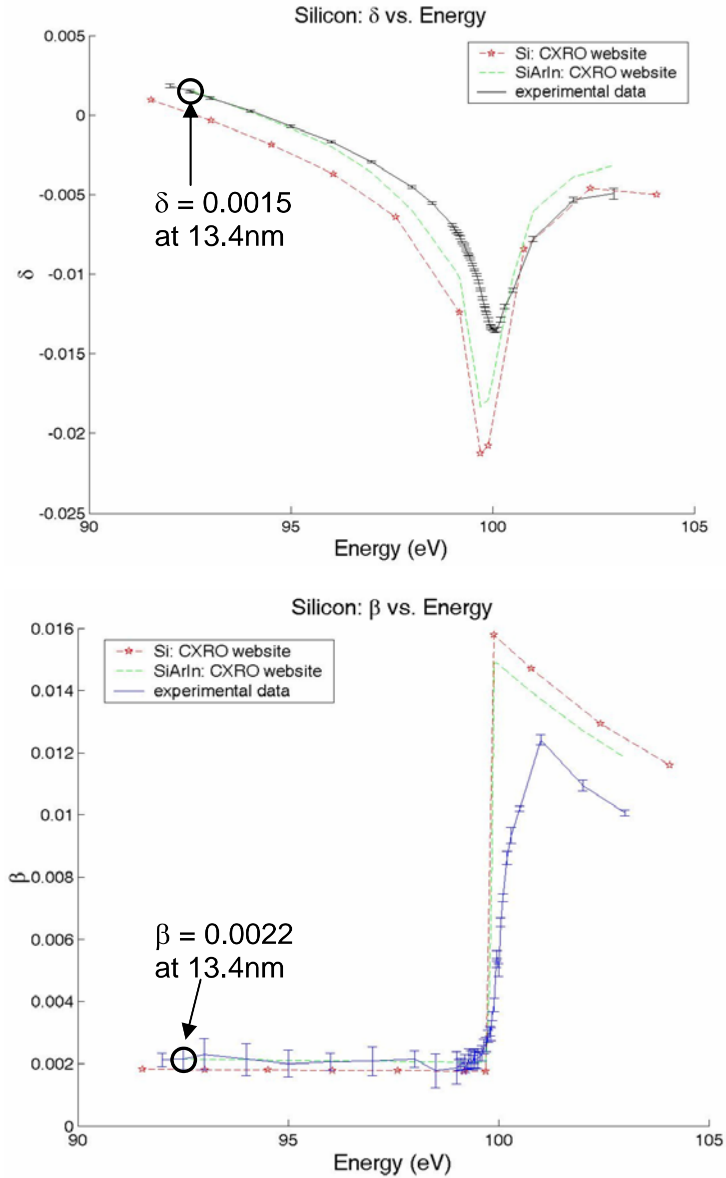

Figure 4-8 (a) δ and (b) β measurements taken about 92.5eV (13.4nm) and silicon's L_2 and L_3 absorption edges (99.8eV and 99.2eV, respectively). Although the sample material was originally thought to be silicon, RBS measurements determined it to be $Si_{93.96}Ar_{5.98}In_{0.06}$. The experimental data is shown with error bars and referenced against data taken using absorption measurements for silicon [85] and $Si_{93.96}Ar_{5.98}In_{0.06}$ [84].

There exists an uncertainty in the index of refraction measurements due to the uncertainty of the thickness, density and composition of the sample material. Rutherford Back-Scattering (RBS) measurements performed by Motorola rectified the density and composition uncertainty. In RBS measurements, high-energy ions incident on the sample are scattered by the atoms of the sample. The energy and number of scattered ions provides information of the composition of the sample, the distribution of those components and the thickness of the sample [88].

In the initial data calculations, the material density was taken from the periodic chart as the sample was assumed to be purely the sputtered sample material. The thickness of the material was taken from alpha step measurements [89] performed on a witness wafer made simultaneously with the sample.

These assumptions were particularly circumspect for the silicon sample. In figure 4-8, the δ and β values calculated from the atomic scattering factors of silicon [85] are shown in red. The significant difference between these red values and the experimental values of the silicon sample led us to have Motorola perform RBS on the sample. The measurements showed that the silicon sample was actually $Si_{93.96}Ar_{5.98}In_{0.06}$ resulting in an overall sample density of 2.313g/cm^3. The argon present in the sample is a result of the argon rich environment of the sputtering chamber. The presence of argon is an important revelation as the

sputtering chamber used to make our sample is that same as that used to make the Mo-Si multi-layer mirrors critical for EUV lithography. The RBS results of the silicon sample are shown in figure 4-9.

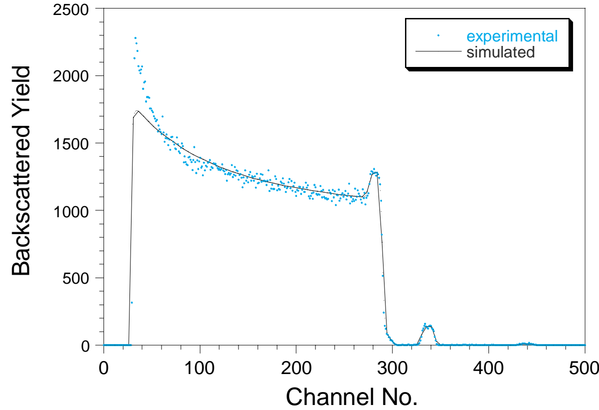

Figure 4-9 RBS results of silicon sample. From the areal density it was found that

$$(Nt)_{\alpha\text{-Si}} = 6.3484 \pm 0.1962 \times 10^{17} \text{atoms / cm}^2\text{, 93.96 atom \%}$$

$$(Nt)_{Ar} = 4.037 \pm 0.1520 \times 10^{16} \text{atoms / cm}^2\text{, 5.98 atom \%}$$

$$(Nt)_{In} = 4.4 \pm 0.4 \times 10^{14} \text{atoms / cm}^2\text{, 0.06 atom \%}$$

resulting in an overall density of 2.313 g /cm^3. RBS measurement courtesy of Motorola.

The strength of this transmission interferometric technique is in the direct measurement of δ. Accurate β measurements are limited to moderately absorbing samples.

4.4 SXR Experiment

Experiment Setup and Data Acquisition

The schematic for the experimental setup for SXR index of refraction measurements is the same as that for EUV measurements shown in figure 4-2.

However, the parameters for the individual elements as well as the distance between these elements have changed for this new energy region.

The pinhole used has a diameter of 2.5μm and is fabricated as shown in figure 3-2. The 2.5μm diameter pinhole generates a high level of spatial coherence at 500eV in both the horizontal and vertical directions, as shown in figures 3-12 and 3-14.

The XOR used for the SXR measurements has a diameter of 280μm, outer zone width of 140nm, and a grating period of 7.84μm. With this diameter, the XOR is placed 248mm downstream of the pinhole in order for it be twice filled by the diffracted soft x-rays near a photon energy of 500eV. The SXR XOR fabrication differs from that used by Chang [70] in that an absorber of 200nm Au is used to create an efficiency of 0.116 at 500eV. [55]

Following equation (4-3), the focal length of the SXR XOR is 16mm at 500eV so the sample mask was placed this distance downstream of the XOR. The XOR parameters were chosen such that the created foci separation would remain at 10μm. The sample mask is fabricated as shown in figure 4-3. The absorber layer used is 1μm of gold. At 500eV, 1μm of gold transmits 3.3E-11 [90].

The CCD camera is attached to the chamber 1.44m downstream of the pinhole. This corresponds to the CCD being a distance downstream from the XOR of $z = 1.44 - p - f(\lambda)$.

The data acquisition in the SXR region is similar to that of the EUV region. The depth of focus of the SXR XOR at 500eV is +/- 15.8μm. This significantly greater depth of focus makes it more difficult to focus the sample mask as less feedback is given for a movement. However, this relatively large depth of focus allows for more forgiveness in the placement of the sample mask.

Results

In the SXR region, two materials were examined: chromium and vanadium. Chromium and vanadium were inspected about their L_3 absorption edges at 574.1eV (2.16nm) and 512.1eV (2.42nm), respectively. The results of these measurements are shown in figures 4-10 and 4-11. The density and composition of the samples was verified using RBS. These results are once again compared to absorption measurements [85].

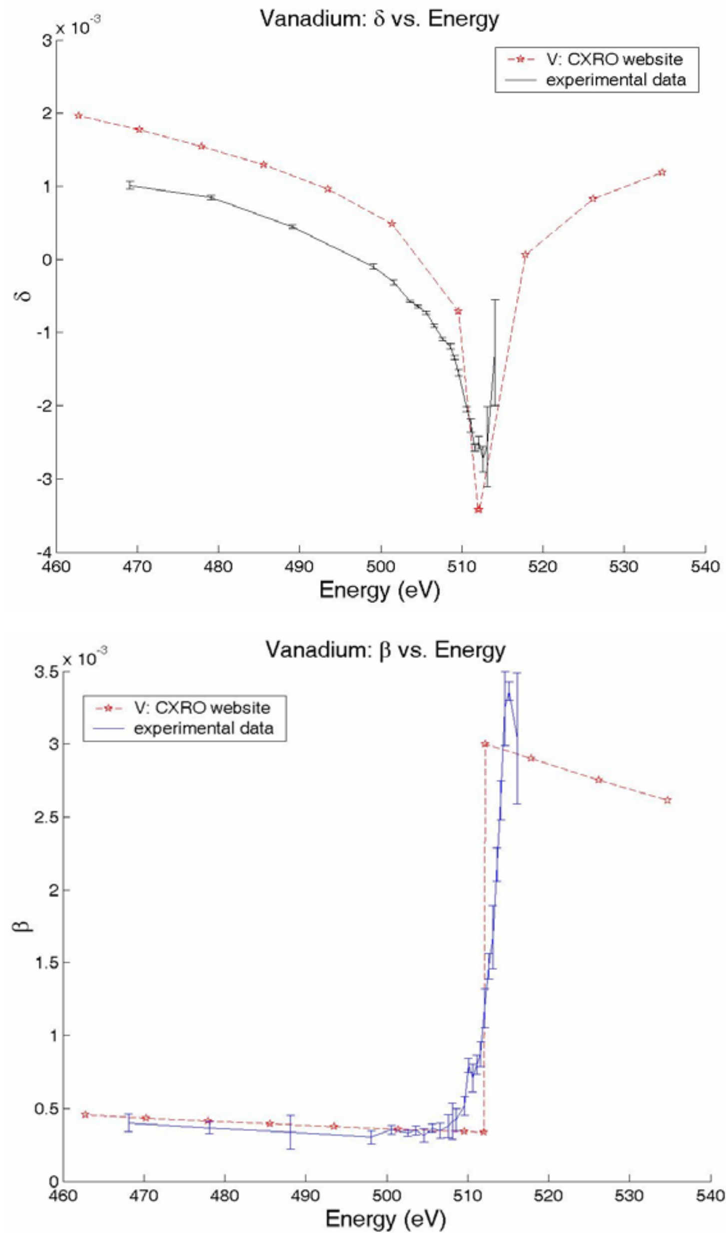

Figure 4-10 (a) δ and (b) β measurements taken about 574.1eV (2.16nm) for vanadium. The experimental data is shown with error bars and referenced against data taken using absorption measurements [85]. The sample used had a thickness of 350nm and a RBS determined density of 5.891g/cm^3. Note the increase in the magnitude of the error bars at energies higher than the absorption edge.

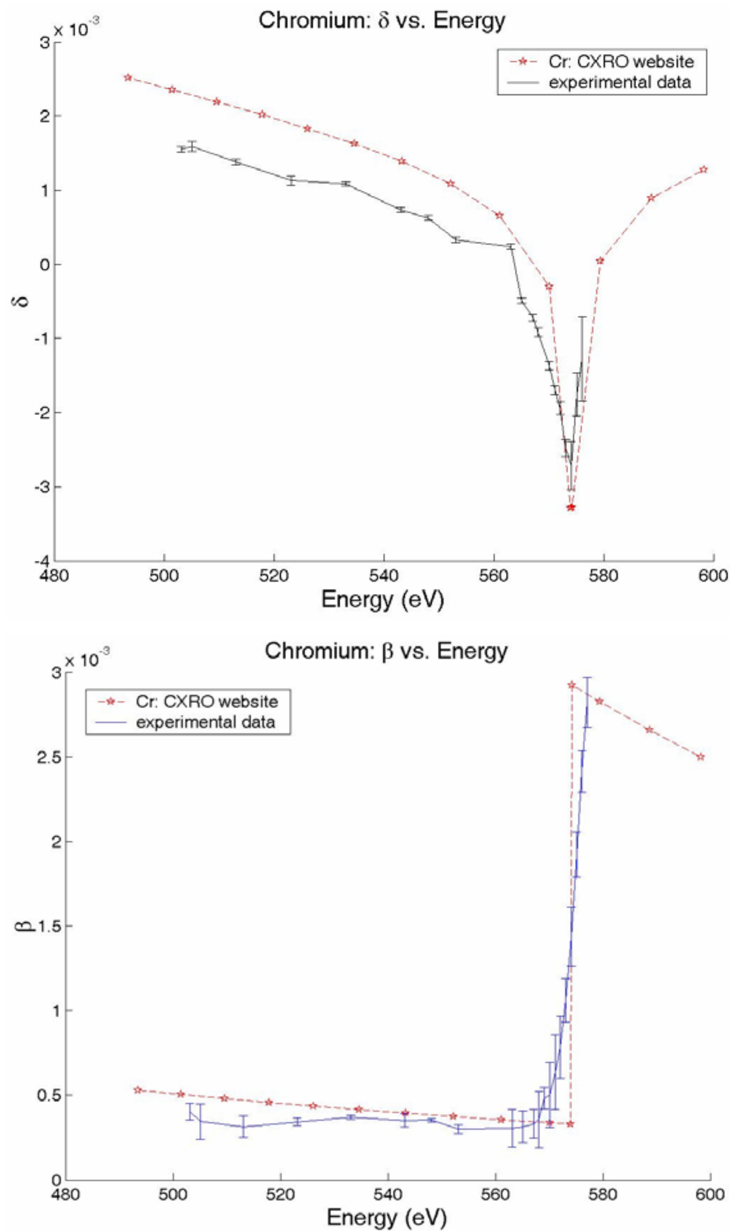

Figure 4-11 (a) δ and (b) β measurements taken about 512.1eV (2.42nm) for chromium. The experimental data is shown with error bars and referenced against data taken using absorption measurements [85]. The sample used had a thickness of 310nm and a RBS determined density of 7.115g/cm^3. Note the increase in the magnitude of the error bars at energies higher than the absorption edge.

4.5 Conclusions

This chapter used coherent EUV and SXR radiation to determine the index of refraction of ruthenium, tantalum silicon nitride, silicon, vanadium and chromium. The method used allowed for direct measurement of both the phase shifting and absorptive part of the index of refraction.

Chapter 5

Conclusions

This thesis presents the design, characterization and first interferometric use of a new tunable, spatially and spectrally coherent soft x-ray branchline at the Advanced Light Source. Specifically, this thesis described the development of third harmonic radiation of an 8cm undulator at the ALS, including photon flux and power available at the focal plane of a new branchline. The value of photon flux in the central radiation cone was measured at the focal plane and found to be within a factor of 2 less than theoretically predicted. Pinhole filtering was used to achieve spatially coherent radiation. The photon flux measured behind a pinhole, chosen to create a resultant angle twice that of the incoming radiation, was measured and determined to be a factor of 4 less than theoretically predicted. A Thompson-Wolf [25] two-pinhole measurement was made to determine the magnitude of the complex coherence factor with respect to transverse distance. The branchline was determined to have a coherence length of 5.4μm and 4.5μm in the horizontal and vertical directions, respectively, at 500eV. The world's first high quality soft x-ray Airy patterns were generated using this new branchline.

With the characterization of the beamline completed, an interferometric experiment designed to directly measure the real and imaginary parts of the index of refraction of several materials was implemented. Measurements were made on an established beamline in the EUV region for samples of silicon,

ruthenium, and tantalum silicon nitride. These are materials important for EUV lithographic applications. The index of refraction measurements were extended to shorter wavelengths with the new coherent soft x-ray branchline. In the soft x-ray region, chromium and vanadium were measured, with results similar to previous reports, but with modest quantitative differences to be analyzed in future studies.

References

[1] P. P. Naulleau, K. A. Goldberg, S. H. Lee, C. Chang, D. Attwood, J. Bokor, “Extreme-ultraviolet phase-shifting point-diffraction interferometer: a wave-front metrology tool with subangstrom reference-wave accuracy,” *Applied Optics*, Vol. 38, Issue 35, pp. 7252-7263, (Dec. 1999).

[2] C. Chang, E. Anderson, P. Naulleau, E. Gullikson, K. Goldberg, D. Attwood, “Direct measurement of index of refraction in the extreme-ultraviolet wavelength region with a novel interferometer,” *Optics Letters*, Vol. 27, Issue 12, pp. 1028-1030, (June 2002).

[3] P. Mercre, P. Zeitoun, M. Idir, S. L. Pape, D. Douillet, X. Levecq, G. Dovillaire, S. Bucourt, K. A. Goldberg, P. P. Naulleau, S. Rekawa, “Hartmann wave-front measurement at 13.4 nm with λ_{EUV}/120 accuracy,” *Optics Letters*, Vol. 28, Issue 17, pp. 1534-1536, (Sept. 2003).

[4] Y. D. Chuang, A. D. Gromko, A. Fedorov, Y. Aiura, K. Oka, Y. Ando, H. Eisaki, S. I. Uchida, D. S. Dessau, “Doubling of the Bands in Overdoped $Bi_2Sr_2CaCu_2O_{8+\delta}$: Evidence for c-Axis Bilayer Coupling,” *Physical Review Letters*, Vol. 87, no.11, pp.117002/1-4, (Sept. 2001).

[5] P. P. Naulleau, K. A. Goldberg, E. H. Anderson, J. Bokor, B. D. Harteneck, K. H. Jackson, D. L. Olynick, F. Salmassi, S. L. Baker, P. B. Mirkarimi, E. A. Spiller, C. C. Walton, D. J. O'Connell, P. Yan, G. Zhang, "Static EUV microexposures using the ETS set-2 optics," *Proc. SPIE*, Vol. 5037, pp. 36-46 (2003).

[6] M.D. Shumway, P. Naulleau, K.A. Goldberg, E.L. Snow, J. Bokor "Resist evaluation at 50 nm in the EUV using interferometric spatial-frequency-doubled imaging," *Proc. SPIE*, Vol. 5037, pp. 910-16, (2003).

[7] M.E. Malinowski, C. Steinhaus, M. Clift, L.E. Klebanoff, S. Mrowka, R. Soufli, "Controlling contamination in Mo/Si multilayer mirrors by Si surface-capping modifications," *Proc. SPIE*, Vol. 4688, pp.442-53, (2002).

[8] Proposed coherent SXR radiation applications include index of refraction determination, lensless magnetic imaging, optics measurement and magnetic scattering.

[9] D.T. Attwood, *Soft X-Rays and Extreme Ultraviolet Radiation: Principles and Applications,* Cambridge, UK: Cambridge University Press, 1999, Chapter 1

[10] T. Warwick, H. Ade, A. P. Hitchcock, H. Padmore, E. G. Rightor and B. P. Tonner, "Soft X-ray spectromicroscopy development for materials science at the Advanced Light Source," *Journal of Electron Spectroscopy and Related Phenomena*, Volume 84, Issues 1-3, pp. 85-98, (March 1997).

[11] "International Technology Roadmap for Semiconductors," 2002 update. See http://public.itrs.net/.

[12] Ref. [9], Chapter 10

[13] P. Naulleau, K.A. Goldberg, E.H. Anderson, D. Attwood, P. Batson, J. Bokor, P. Denham, E. Gullikson, B. Harteneck, B. Hoef, K. Jackson, D. Olynick, S. Rekawa, F. Salmassi, K. Blaedel, H. Chapman, L. Hale, P. Mirkarimi, R. Soufli, E. Spiller, D. Sweeney, J. Taylor, C. Walton, D. O'Connell, D. Tichenor, C.W. Gwyn, P.-Y. Yan, G. Zhang, "Sub-70 nm

extreme ultraviolet lithography at the advanced light source static microfield exposure station using the engineering test stand set-2 optic," *Journal of Vacuum Science & Technology B,* Vol. 20, no. 6, pp. 2829-33. (Nov. 2002).

[14] B. Niemann, D. Rudolph, G. Schmahl, "X-ray microscopy with synchrotron radiation," *Applied Optics*, Vol.15, no.8, pp.1883-4, (Aug. 1976).

[15] D. Sayre, R. Feder, E. Spiller, J. Kirz, D.M. Kim, "Potential operating region for ultrasoft X-ray microscopy of biological materials," *Science*, Vol.196, no.4296, pp.1339-40, (June 1977).

[16] W. Meyer-Ilse, G. Denbeaux, L.E. Johnson, W. Bates, A. Lucero, and E.H. Anderson, "The high resolution x-ray microscope, XM-1," in "Sixth International Conference on X-Ray Microscopy, Berkeley, CA, USA 1999," (*AIP Conf. Proc.*, 507), pp. 129-34.

[17] W. Chao, E. H. Anderson, G. P. Denbeaux, B. Harteneck, J. A. Liddle, D. L. Olynick, A. L. Pearson, F. Salmassi, C. Y. Song, D. T. Attwood, "20-nm-resolution soft x-ray microscopy demonstrated by use of multilayer test structures," *Optics Letters*, Vol. 28, Issue 21, pp. 2019-2021, (Nov. 2003).

[18] W. Meyer-Ilse, D. Hamamoto, A. Nair, S.A. Lelievre, G. Denbeaux, L. Johnson A.L. Pearson, D. Yager, M.A. Legros, C.A. Larabell, "High resolution protein localization using soft X-ray microscopy," *Journal of Microscopy,* Vol.201, pt.3, pp. 395-403, (March 2001).

[19] J.J. Rocca, "Table-top soft X-ray lasers" *Review of Scientific Instruments*, Vol.70, no.10, pp.3799-827, (Oct. 1999).

[20] E. A. Gibson, A. Paul, N. Wagner, R. Tobey, D. Gaudiosi, S. Backus, I. P. Christov, A. Aquila, E. M. Gullikson, D. T. Attwood, M. M. Murnane, and H. C. Kapteyn, "Coherent soft x-ray generation in the water window with quasi-phase matching," *Science,* Vol.302, no.5642, pp.95-8, (Oct. 2003).

[21] E. Seres, J. Seres, F. Krausz, and C. Spielmann "Generation of coherent soft-x-ray radiation extending far beyond the titanium L edge," *Physical Review Letters*, Vol.92, no.16, pp.163002/1-3, (April 2004).

[22] Y. Liu, *Coherence Properties of Extreme Ultraviolet/Soft X-Ray Sources*, Ph.D. dissertation, University of California, Berkeley (2003).

[23] D.T. Attwood, P. Naulleau, K.A. Goldberg, E. Tejnil, C. Chang, R. Beguiristain, P. Batson, J. Bokor, E.M. Gullikson, M. Koike, H. Medecki, J.H. Underwood, "Tunable Coherent Radiation in the Soft X-ray and Extreme Ultraviolet Spectral Regions," *IEEE Journal of Quantum Electronics*, Vol. 35, no. 5, pp. 709-720, (May 1999).

[24] C. Chang, P. Naulleau, E. Anderson, D. Attwood, "Spatial coherence characterization of undulator radiation," *Optics Communications*, Vol.182, no.1-3, pp.25-34, (Aug. 2000).

[25] B.J. Thompson, E. Wolf, "Two-Beam Interference with Partially Coherent Light," *Journal of the Optical Society of America*, Vol. 47, no. 10, pp.895-902, (Oct. 1957).

[26] K. Rosfjord, C. Chang, D. Attwood, "Direct index of refraction measurement of silicon and ruthenium at EUV wavelengths," Accepted at *SPIE's Optical*

Constants of Materials for UV to X-Ray Wavelengths, Denver, CO, (Aug. 2004).

[27] Ref. [9], Chapter 7.

[28] D. Attwood, K. Halbach, K. Kim, "Tunable Coherent X-rays," *Science*, Vol. 228, no. 4705, pp.1265-72, (June 1985).

[29] http://www-als.lbl.gov/als/als_users_bl/bl_layout.html

[30] Ref. [9], Chapter 5.

[31] T. Harada, S. Moriyama, T. Kita, "Mechanically ruled stigmatic concave gratings," *Japanese Journal of Applied Physics*, Vol.14, suppl.14-1, pp.175-9. (1975).

[32] T. Harada, T. Kita, "Mechanically ruled aberration-corrected concave gratings," *Applied Optics*, Vol.19, no.23, pp.3987-93, (Dec. 1980).

[33] J.W. Goodman, *Statistical Optics,* New York, NY: Wiley and Sons Inc, 2000, Chapter 5.

[34] M. Born and E. Wolf, *Principles of Optics 7th Edition,* Cambridge, UK: Cambridge University Press, 2002, Chapter 10.

[35] P.H. van Cittert, "The Probable Distribution of Vibrations in a Plane Illumniated by a Light Source Either Directly or Through a Lens," *Physica 1* pp. 201-210, (1934).

[36] F. Zernike, "The concept of degree of coherence and its application to optical problems," *Physica V*, Vol. 8, pp. 785-795 (1938).

[37] K.-J. Kim, “Characteristics of Synchrotron Radiation,” pp 565 –632 in *Physics of Particale Accelerators*, AIP Conference Proceedings 184 (Amer. Inst. Of Physics, New York, 1989), M. Month and M. Dienes, Editors.

[38] K.-J. Kim, “Optical and power characteristics of synchrotron radiation sources,” *Optical Engineering*, Vol.34, no.2, pp.342-52. (Feb. 1995).

[39] Kwang-Je Kim, “Brightness, Coherence and Propagation Characteristics of Synchrotron Radiation,” *Nuclear Instruments and Methods in Physics Research* A246, pp. 71-76, (1986).

[40] K.-J. Kim, “Characteristics of Synchrotron Radiation,” X-ray Data Booklet, (Center for X-ray Optics, Lawrence Berkeley National Laboratory, 1999) Second Edition.

[41] A. Hofmann, “Quasi-monochromatic synchrotron radiation from undulators,” *Nuclear Instruments & Methods*, Vol.152, no.1, pp.17-21, (June 1978).

[42] A. Hofmann, “Theory of Synchrotron Radiation” Stanford Synchrotron Radiation Laboratory report ACD-Note 38 (unpublished).

[43] J.D. Jackson, *Classical Electrodynamics, 3rd Edition*, John Wiley and Sons, Inc., NY, NY, 1999, Chapter 14.

[44] S. Ramo, J. Whinnery, T. Van Duzer, *Fields and Waves in Communication Electronics, 3rd Edition*, John Wiley and Sons, Inc., NY, NY 1994, Chapter 12.

[45] Y. Liu (CXRO/LBNL), private communication.

[46] Ref. [9], Chapter 8.

[47] Ref. [9], Chapter 3.

[48] K. Rosfjord, C. Kemp, P. Denham, E. Gullikson, P. Batson, S. Rekawa, D. Attwood, "Coherent Soft X-ray Branchline at the Advanced Light Source," *Proc. Of* Synchrotron *Radiation Instrumentation*, pp.448-449, (August 2003).

[49] E. Gullikson, "Hitachi Ruled Gratings for the Coherent Optics Beamline ALS 12.0.2", CXRO/LBNL, Memo sent January 13, 2003, (unpublished).

[50] P. Kirkpatrick and A. V. Baez, "Formation of Optical Images by X-rays," *Journal of the Optical Society of America*, Vol. 38, Issue 9, pp. 766 - 774 (September 1948).

[51] http://www.hpk.co.jp/Eng/products/ssd/pdf/g1126-02_etc_kgpd1005e01.pdf

[52] F. Scholze, H. Henneken, P. Kuschnerus, H. Rabus, M. Richter, G. Ulm, "Determination of the electron-hole pair creation energy for semiconductors from the spectral responsivity of photodiodes," *Nuclear Instruments & Methods in Physics Research Section A-Accelerators Spectrometers Detectors & Associated Equipment*, Vol.439, no.2-3, pp.208-15, (Jan. 2000).

[53] Eric Gullikson (CXRO/LBNL), private communication.

[54] Paul A. Ziarnowski (National Aperture), private communication.

[55] Bruce Harteneck (CXRO/LBNL), private communication.

[56] J.W. Goodman, *Introduction to Fourier Optics 2nd Edition,* New York, NY: McGraw Hill, 1996, Chapter 3.

[57] Measurement made by Eric Gullikson (CXRO/LBNL) at beamline 6.3.2 of the ALS.

[58] J. Janesick, *Scientific Charge-Coupled Devices*, Bellingham, WA, SPIE Press, 2001, Chapter 1.

[59] K. Rosfjord, P. Denham, D. Attwood, "First high-quality airy patterns at soft x-ray wavelengths," OSA's Frontier's in Optics post deadline technical digest, Tucson, AZ, (Oct. 2003).

[60] Matlab™, Copyright 1984-2001, The MathWorks, Inc.

[61] Ref. [34], Chapter 8.

[62] T. Young, *A Course of Lectures on Natural Philosophy and The Mechanical Arts I* (Printed for J. Johnson, London, 1807).

[63] B.J. Thompson and E. Wolf, "Two-Beam Interfernce with Partially Coherent Light," *Journal of the Optical Society of America*, Vol. 47, no 10, pp. 895-902, (Oct. 1957).

[64] Y. Liu, M. Seminario, F.G. Tomasel, C. Chang, J.J. Rocca, D.T. Attwood, "Achievement of Essentially Full Spatial Coherence in a High Average Power Soft X-Ray Laser," *Physical Review A*, Vol.63, no.3, pp.033802/1-5, (March 2001).

[65] T. Ditmire, J. Tisch, E.T. Gumbrell, R.A. Smith, D.D. Meyerhofer, M.H.R. Hutchinson, "Spatial coherence of short wavelength high-order harmonics," *Applied Physics B-Lasers & Optics*, Vol. B65, no.3, pp.313-28, (Sept.1997).

[66] Y. Takayama, T. Hatano, T. Miyahara, W. Okamoto, "Relationship between spatial coherence of synchrotron radiation and emittance," *Journal of Synchrotron Radiation,* Vol. 5, pt. 4, pp. 1187-94, (July 1998).

[67] R. Coisson, "Spatial coherence of synchrotron radiation," *Applied Optics*, Vol. 34, Issue 5, pp. 904-908, (February 1995).

[68] R.A. Bartels, A. Paul, M.M. Murnane, H.C. Kapteyn, S. Backus, Y. Liu, D.T. Attwood, “Absolute determination of the wavelength and spectrum of an extreme-ultraviolet beam by a Young's double-slit measurement,” *Optics Letters*, Vol. 27, Issue 9, pp. 707-709, (May 2002).

[69] L. Mandel, “Fluctuations of Photon Beam: The Distribution of the Photo-Electrons,” *Proc. Phys. Soc.* (London), Vol. 74, pp. 233-243 (1959).

[70] C. Chang, P. Naulleau, D. Attwood “Analysis of illumination coherence properties in small-source systems such as synchrotrons,” *Applied Optic*s, vol. 42, issue 14, pp. 2506-12, (May 2003).

[71] B. Saleh, M. Teich, *Fundamentals of Photonics,* John Wiley & Sons, Inc., NY, NY, 1991, Chapter 2.

[72] M. Francon, *Optical Interferometry*, Academic Press, NY, NY 1966, Chapters 2 and 3.

[73] S. Tolanksy, *An Introduction to Interferometry*, Longmans, Green and Co, NY, NY, 1955, Chapters 4-6.

[74] E. Hecht, *Optics 4th Edition*, Addison Wesley, San Francisco, CA 2002, Chapter 9.

[75] S. Han, E. Weisbrod, J. Wasson, B. Lu, R. Gregory, Q. Xie, P. Mangat, S. Hector, W. Dauksher, K. Rosfjord, “Development of Phase Shift Masks for Extreme Ultra Violet Lithography and Optical Evaluation of Phase Shift Material,” to appear in *SPIE’s Microlithography*, Santa Clara, CA (Feb. 2004).

[76] B.L. Henke, E.M. Gullikson, and J.C. Davis. "X-ray interactions: photoabsorption, scattering, transmission, and reflection at E=50-30000 eV, Z=1-92," *Atomic Data and Nuclear Data Tables* Vol. 54, no. 2, pp.181-342, (July 1993).

[77] R. de L. Kronig, H.A. Kramers, *Atti Congr. Intern. Fisici*, Como 2, 545 (1927).

[78] L.D. Landau, E.M. Lifschitz, *Electrodynamics of Continuous Media, 2nd Edition*, Pergamon Press, Oxford, England, Chapter 9, (1984).

[79] R. Soufli, E. Gullikson, "Reflectance measurements on clean surface for the determination of optical constants of silicon in the extreme ultraviolet-soft-x-ray region," *Applied Optics*, Vol. 36, Issue 22, pp. 5499-5507, (Aug. 1997).

[80] H. Medecki, E. Tejnil, K. A. Goldberg, J. Bokor, "Phase-shifting point diffraction interferometer," *Optics Letters*, Vol. 21, Issue 19, pp. 1526-1528, (Oct 1996).

[81] Chang, C. Naulleau, P., Anderson, E., Rosfjord, K., Attwood, D., "Diffractive Optical Elements Based on Fourier Optical Techniques: A New Class of Optics for Extreme Ultraviolet and Soft X-ray Wavelengths." *Applied Optics-IP*, Volume 41, Issue 35, pp. 7384-7389, (Dec 2002).

[82] Ref. [9], Chapter 9.

[83] M. Takeda, H. Ina, S. Kobayashi, "Fourier-transform method of fringe-pattern analysis for computer-based topography and interferometry," *Journal of the Optical Society of America*, Vol. 72, Issue 1, pp. 156-160 (Jan. 1982).

[84] http://www-cxro.lbl.gov/optical_constants/getdb2.html

[85] http://www-cxro.lbl.gov/optical_constants/asf.html

[86] S-I. Han, J.R. Wasson, P.J.S. Mangat, J.L. Cobb, K. Lucas and S.D. Hector, "Novel Design of Att-PSM Structure for Extreme Ultra Violet Lithography and Enhancement of Image Contrast during Inspection," *Proc. SPIE*, Vol. 4688, pp. 481-494, (2002).

[87] S.-I. Han, E. Weisbrod, Q. Xie, and P.J.S. Mangat, S. D. Hector, W. J. Dauksher, "Design and Method of Fabricating Phase Shift Masks for Extreme Ultra Violet Lithography by Partial Etching into the EUV Multilayer Mirror," *Proc. SPIE*, Vol. 5037, pp. 314, (2003).

[88] http://www.cea.com/cai/rbstheo/intro.htm

[89] Alpha-Step® 500 Surface Profiler, Copyright 1994, Tencor Instruments.

[90] http://www-cxro.lbl.gov/optical_constants/filter2.html

Appendix A

Grating parameters

This appendix contains the parameters for the 600 lines/mm and 1200 lines/mm gratings for the monochromator of beamline 12.0.2. These parameters include the radiation incoming angle,ϕ, the photon energy, the wavelength and the corresponding linear wavelength dispersion.

600 lines/mm

ϕ (degrees)	Energy (eV)	Wavelength (nm)	Dispersion (nm/μm)
0.1	3060	0.410	5.70E-04
0.2	1530	0.810	5.50E-04
0.3	1020	1.22	5.40E-04
0.4	764	1.62	5.20E-04
0.5	611	2.03	5.10E-04
0.6	509	2.43	4.90E-04
0.7	436	2.84	4.80E-04
0.8	382	3.25	4.70E-04
0.9	340	3.65	4.50E-04
1.0	306	4.06	4.40E-04
1.1	277	4.46	4.20E-04
1.2	255	4.87	4.10E-04
1.3	235	5.28	3.90E-04
1.4	218	5.68	3.80E-04
1.5	204	6.09	3.60E-04
1.6	171	7.25	3.50E-04
1.7	180	6.90	3.30E-04
1.8	170	7.30	3.20E-04
1.9	161	7.71	3.10E-04
2.0	153	8.11	2.90E-04
2.1	146	8.52	2.80E-04
2.2	139	8.93	2.60E-04
2.3	133	9.33	2.50E-04
2.4	127	9.74	2.30E-04

2.5	122	10.2	2.20E-04
2.6	118	10.6	2.00E-04
2.7	113	11.0	1.90E-04
2.8	109	11.4	1.70E-04
2.9	105	11.8	1.60E-04
3.0	102	12.2	1.50E-04
3.1	98.6	12.6	1.30E-04
3.2	95.5	13.0	1.20E-04
3.3	92.6	13.4	1.00E-04
3.4	89.9	13.8	8.70E-04
3.5	87.3	14.2	7.30E-04
3.6	84.9	14.6	5.80E-04
3.7	82.6	15.0	4.40E-04
3.8	80.5	15.4	2.90E-04
3.9	78.4	15.8	1.50E-04

1200 lines/mm

ϕ (degrees)	**Energy (eV)**	**Wavelength (nm)**	**Dispersion (nm/μm)**
0.1	6110	0.200	2.80E-04
0.2	3060	0.410	2.80E-04
0.3	2040	0.610	2.70E-04
0.4	1530	0.810	2.60E-04
0.5	1220	1.01	2.50E-04
0.6	1020	1.22	2.50E-04
0.7	873	1.42	2.40E-04
0.8	764	1.62	2.30E-04
0.9	679	1.83	2.30E-04
1.0	611	2.03	2.20E-04
1.1	556	2.23	2.10E-04
1.2	509	2.43	2.00E-04
1.3	470	2.64	2.00E-04
1.4	436	2.84	1.90E-04
1.5	407	3.04	1.80E-04
1.6	382	3.25	1.70E-04
1.7	360	3.45	1.70E-04
1.8	340	3.65	1.60E-04
1.9	322	3.86	1.50E-04
2.0	306	4.06	1.50E-04
2.1	291	4.26	1.40E-04

2.2	278	4.46	1.30E-04
2.3	266	4.67	1.20E-04
2.4	255	4.87	1.20E-04
2.5	245	5.07	1.10E-04
2.6	235	5.27	1.00E-04
2.7	226	5.48	9.50E-05
2.8	218	5.68	8.70E-05
2.9	211	5.88	8.00E-05
3.0	204	6.08	7.30E-05
3.1	197	6.29	6.50E-05
3.2	191	6.49	5.80E-05
3.3	185	6.69	5.10E-05
3.4	180	6.90	4.40E-05
3.5	175	7.10	3.60E-05
3.6	170	7.30	2.90E-05
3.7	165	7.51	2.20E-05
3.8	161	7.71	1.50E-05
3.9	157	7.91	7.30E-06